Three-Dimensional Linear Stability Analysis of Flat-Plate Boundary Layers with Supercritical Fluids

Francisco Ramalho Matias

Delft University of Technology

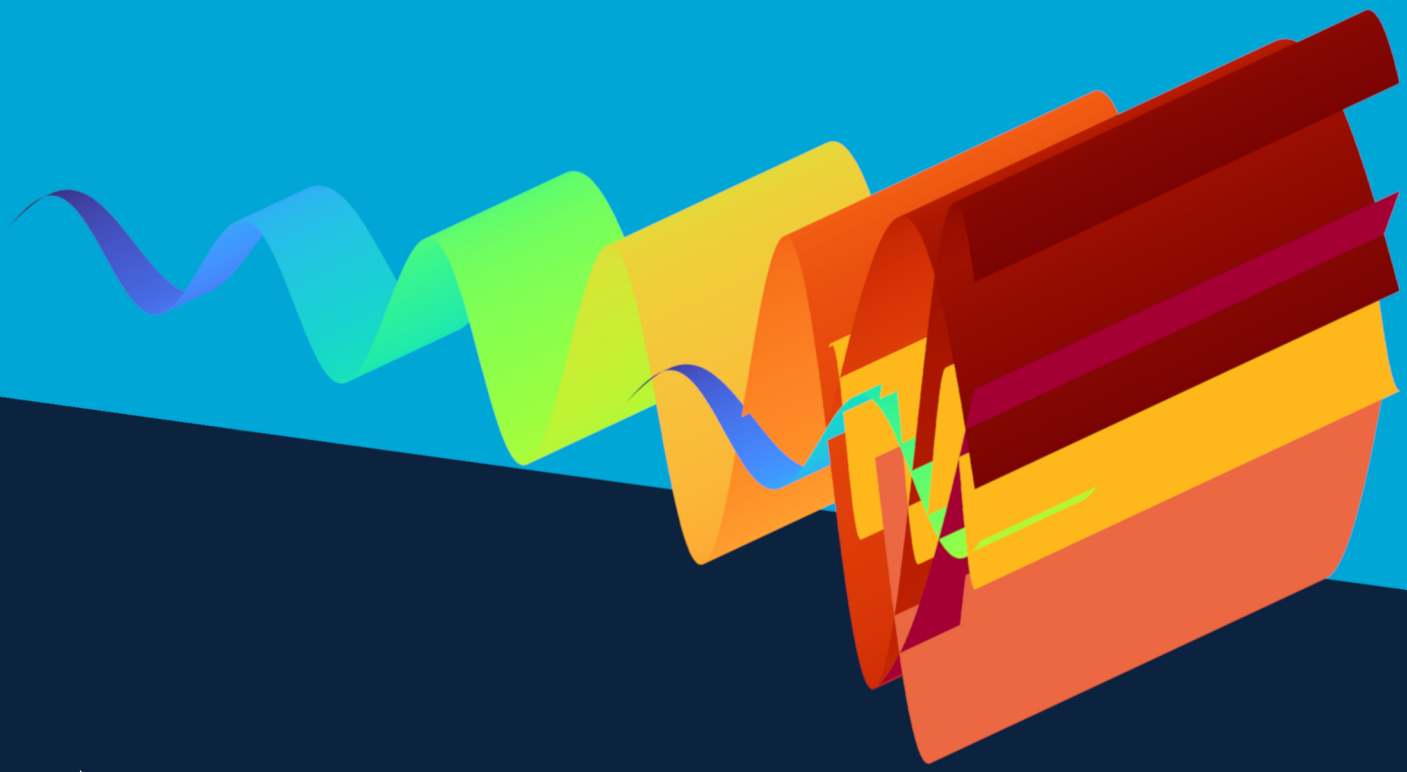

TU Delft

Three-Dimensional Linear Stability Analysis of Flat-Plate Boundary Layers with Supercritical Fluids

by

Francisco Ramalho Matias

in partial fulfillment of the requirements for the degree of
Master of Science in Mechanical Engineering
at the Delft University of Technology

Student number:	5387523
Thesis committee:	Prof. Dr. ir. R. Pecnik, TU Delft, Supervisor and Chairman
	M.Sc. P.C. Boldini, TU Delft, Daily Supervisor
	Dr. ir. P. Costa, TU Delft
Supervisors:	M.Sc. P.C. Boldini
	Dr. ir. B. Bugeat
	Prof. Dr. ir. R. Pecnik

Acknowledgements

Hello, dear reader. I read on the acknowledgements of a PhD thesis that the acknowledgements are in fact the most read part of a thesis. And so, I find myself starting this letter in the very same manner as that PhD student. I thank you, the reader, for taking interest in this thesis, and also in me. I'll start by introducing myself. My name is Francisco Matias, I was born in 1999 in Portugal, having completed my undergraduate studies there. I came to the Netherlands in 2020 with the motivating goal to complete a Masters degree at TU Delft.

I have now been living in the Netherlands for four years, and these have not been without challenge. Perhaps the most common among international students comes from being away from home, from my family and friends. The need to build strong relations, with people you can confide and trust in is difficult, especially in a previously unknown culture. Surely, my early twenties were a time of great personal growth. I was met with many moments of joy, but also great personal hardships. I thank all of those who have accompanied me in this journey. It is now, in September of 2024, that I will finally put behind the goal which originally brought me to the Netherlands. I'm sure that, in time, as I look back at the final stages of this Masters degree, I will find a pivotal moment in the completion of this thesis, after which I can face new, and hopefully exciting challenges. I will face them with fortitude and care.

For the last years, I have many to thank. First of all, I'd like to express my sincere gratitude to my supervisor and daily supervisors, Professor Rene Pecnik, and Pietro Boldini and Benjamin Bugeat respectively. I thank them for their patience and guidance throughout this project. Their passion for the research topic was evident and inspiring, bringing clarity but also challenge during our discussions.

To my friends in the Netherlands – Pranav Molahalli, Siddharth Bokil, Ugne Bunikyte, Yehor Furtsev, Fedir Furtsev – they have provided the necessary bedrock upon which I can find emotional support and stability away from home. To my friends in Portugal – António Pato, Miguel Figueira, Henrique Reis, Cristina Rogeiro, and António Moraes – their companionship and care were most needed during these past years, and for that I thank you.

And finally, to my family, to my dad Jorge and my sister Ana. For their support and encouragement which helped me stay motivated. And to my mom, Isabel,

obrigado.

Francisco Matias

September, 2024

Abstract

Laminar to turbulent transition is the process in which a smooth orderly laminar flow becomes turbulent, chaotic and unpredictable. A laminar boundary layer (BL) may become turbulent due to growing disturbances in the flow. If a disturbance is small its behavior is governed by linear stability theory (LST). Early works on LST were focussed on the growth of normal modes in incompressible or ideal gas compressible boundary layers, with the more recent inclusion of high-temperature and/or dense gas effects. Consideration for growth of perturbations other than modal started in 1970s, and while it has received considerable attention in ideal gas boundary layers, the study of non-modal growth in heavily stratified boundary layers remains limited.

In recent years, research in supercritical fluids and their applications has risen substantially, where supercritical CO2 (SCO2) stands out. It has been proposed as a working fluid for power generation turbines, a heat carrier fluid in geothermal, etc. A supercritical fluid near its pseudo-boiling temperature exhibits extremely large variations of physicochemical properties, leading to strongly stratified transcritical boundary layer flows, which may heavily influence its stability. Recently, transcritical boundary layers have been shown to be unstable to a novel mode, not found in ideal gas boundary layers, further motivating the study of the hydrodynamic behaviour of supercritical fluids.

This study investigates the linear stability of SCO2 boundary layers in the region of the Widom line in the phase diagram. Both heating and cooling are considered, in the sub-, super- and transcritical regimes. Regarding the amplification of normal modes, a special focus is given to 3D perturbations and the conditions for which a 3D perturbation is more amplified than a 2D perturbation. A moderate Mach number is found to be necessary in the further destabilization of 3D waves when compared to 2D waves. As indicated by previous works, the Tollmien-Schlichting (TS) mode is found to be preferentially 3D for moderate Mach number in the sub- and supercritical regimes. However, in the transcritical regime, the TS mode is found to be most amplified for stream-wise propagating waves. The novel mode II, found solely in transcritical flows, is preferentially 3D at sufficiently high Mach number, both in the viscous and inviscid regimes. Regarding non-modal stability, the energy growth of sub- and supercritical boundary layers is comparable to that of an ideal gas compressible boundary layer, with optimal energy growth driven by the lift-up mechanism. In the transcritical regimes, the lift-up mechanism also dominates, but energy growth is considerably larger due to the presence of strong thermodynamic gradients within the flow. This results in substantial energy growth associated with density and temperature streaks in the perturbations. When considering purely kinetic effects, the cooled wall case shows higher growth when compared to an ideal gas boundary layer, whereas the heated wall case shows a reduction of the kinetic energy growth. The cooled wall condition results in high mean vorticity far from the wall, leading to high energy growth, while the heated wall condition results in low mean vorticity far from the wall, leading to a reduced energy growth.

List of Figures

List of Tables

Contents

Nomenclature

Abbreviations

NS	Navier-Stokes
TS	Tollmien-Schlichting
BL	Boundary layer
CO2	Carbon dioxide
SCO2	Supercritical carbon dioxide
GIP	Generalized inflection point
1D	One-dimensional
2D	Two-dimensional
3D	Three-dimensional
c.c.	Complex conjugate

Latin Symbols

x	Streamwise coordinate
y	Wall-normal coordinate
z	Spanwise coordinate
t	Time
T	Temperature
p	Pressure
L	Length
C_p	Specific heat capacity at constant pressure
i	Complex identity
e	Euler's constant
$\underline{\mathrm{u}}$	Velocity field
u	Velocity in the streamwise direction
U	Base flow velocity in the streamwise direction
q	State vector
a	Speed of sound
c	Phase speed
F	Dimensionless frequency
B	Dimensionless span-wise wave number
Re	Reynolds number
Pr	Prandtl number
M	Mach number
Ec	Eckert number
D	Partial derivative with respect to the wall-normal direction

Greek Symbols

α	Streamwise wavenumber
β	Spanwise wavenumber
ω	Frequency
δ	Reference length in the wall normal direction
μ	Dynamic viscosity
ρ	Density
ν	Kinematic viscosity
κ	Thermal conductivity

Superscripts

H	Hermitian transpose
$'$	Perturbation quantity
–	Mean flow quantity
$*$	complex conjugate of perturbation quantity

Subscripts

∞	Free-stream quantity
r	Real part
i	Imaginary part
ref	Reference
rel	Relative
c	Critical
pc	Pseudo-critical
max	Maximum
opt	Optimum
in	Inlet quantity
out	Outlet quantity
s	At the location of the GIP

1

Introduction

When considering the flow of a low viscosity fluid over a body, the boundary layer is understood as the very thin layer close to the body where viscosity is important. In the remaining region outside this layer viscosity is assumed to be negligible. It was Prandtl (1905) who first introduced this treatment. Since, many complex engineering problems have been clarified using this simplifying approach. Most notably, boundary-layer theory is used to predicted aerodynamic loads and heat transfer rates on a body placed in a fluid stream. Consider for instance the drag force experience by a ship in the sea, or by the wings of a plane. Further, consider the flow of fluids through the blades of turbomachinery in refrigeration or power cycles. It is boundary-layer theory that supplies an answer as to the form that it is necessary to give the blades in order attain better efficiencies.

In many applications, the flow of a fluid over a body is characterized by an unorderly and chaotic behaviour. In this state, a flow is called turbulent. Conversely, an orderly flow is called laminar. The transition from a laminar to a turbulent flow is of great importance in engineering. Indeed, the heat transfer rate and the loads experienced by a body in a fluid stream greatly depend on weather the flow in the boundary-layer is laminar or turbulent. It is within this context of laminar-to-turbulent transition that the stability of boundary layers is studied.

Hydrodynamic stability is concerned with the response of a laminar flow to a disturbance. Consider that a small perturbation is applied to a laminar flow initially in equilibrium. If the perturbation decays with time and the flow effectively returns to its initial state, the flow is considered stable. Conversely, if the perturbation grows with time, the flow is considered unstable. Such an instability may cause the flow to become turbulent.

Boundary layer stability was first considered by Prandtl (1921). Through a simplified approach, Prandtl discovered an otherwise inviscidly stable boundary layer flow to be unstable in the presence of viscous forces. It is relevant to stress the importance of this result, it uncovered the important role of viscosity, traditionally viewed as a purely stabilizing force, in the destabilization of viscous flows. Since 1921, the stability of incompressible and ideal-gas compressible boundary layers has seen extensive research.

During the 1990s, driven by the development of hypersonic vehicles, the interest in non-ideal boundary layer stability increased. Studies feature various non-ideal behaviour, namely high-temperature and dense gas effects. More recently, the work of Ren et al. (2019b) considers the stability of a supercritical boundary layer. In some engineering applications, the use of supercritical fluids is advantageous due to the ease of manipulation of their thermodynamic and transport properties by simply varying pressure and temperature. For instance, in integrated circuit manufacturing, King and Williams (2003) reviewed the use of supercritical carbon dioxide (SCO2) on wafer cleaning, film deposition, photoresist stripping,

etc. A particularly exciting application of supercritical fluids is in power-cycles where SCO2 is often proposed as the working fluid. These power-cycles have been extensively analyzed in recent literature and have been shown to be theoretically competitive. SCO2 power-cycles find variety of applications, including concentrated solar power, geothermal power, waste heat recovery, and nuclear reactors (White et al., 2021). Motivated not only by the growing interest in supercritical fluids, but also by the result of Ren et al. (2019b) which uncovered a previously unknown unstable mode in supercritical boundary-layer, the present thesis aims to extend to research of boundary-layer stability with supercritical fluids.

In this introductory chapter, Section 1.1 offers an introduction to supercritical fluids. Section 1.2 presents important results regarding the modal and non-modal stability of boundary layers. Section 1.3 outlines the research objectives of the current work, and lastly, Section 1.4 provides the lay-out of the present thesis.

1.1. Supercritical Fluids

A supercritical state of matter occurs at temperatures and pressures exceeding its critical point. At subcritical conditions, below the critical temperature and pressure, a coexistence region exists where both gas and liquid coexist in equilibrium. Additional heat added to the system results in the vaporization of the liquid, with a sudden change in thermodynamic and transport properties. At supercritical conditions, only a single phase exists. Therefore, at subcritical conditions there is a discontinuous phase change from liquid to gas, while at supercritical pressures, the phase change is continuous and occurs over a narrow range of temperatures around the pseudo-critical temperature. The pseudo-critical temperature is defined as the temperature at which the specific heat at constant pressure (C_p) reaches its maximum. Figure 1.1 shows the phase diagram for CO2, with critical conditions $T_c = 304.1\,\text{K}$ and $p_c = 73.8\,\text{bar}$. The supercritical region, shown in red, exists at pressures and temperatures above the critical point. The gas-liquid coexistence region is represented by the black line in the $p - T$ space. The Widom line, or pseudo-critical line, is represented by the dotted line.

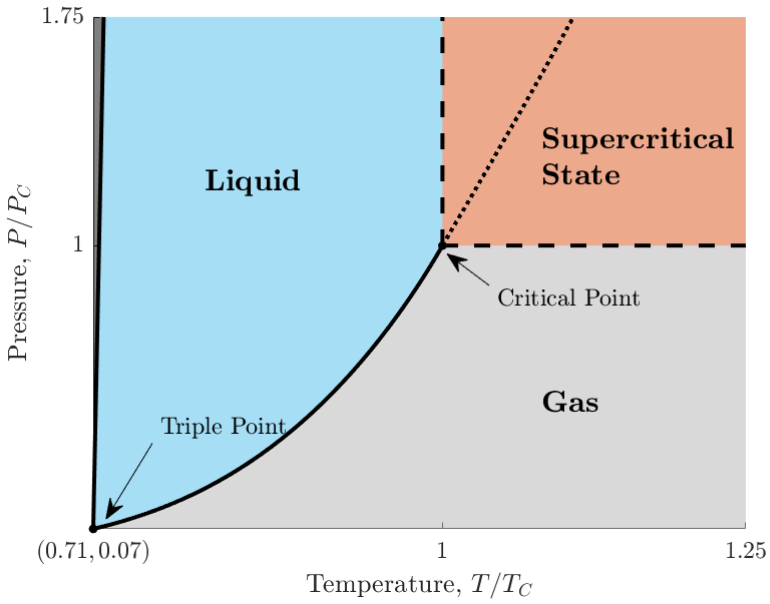

Figure 1.1: Pressure - Temperature phase diagram of CO2

At supercritical conditions, below the pseudo-critical temperature, a fluid exhibits properties

typical of a liquid: high density, high viscosity, etc. Conversely, above pseudo-critical temperatures, a supercritical fluid behaves in a gas-like manner. In the present work, a flow in which the temperature crosses the Widom point is defined as a transcritical flow. A subcritical flow is a flow in which the temperature is below pseudo-critical, and in a supercritical flow the temperatures are above pseudo-critical.

1.2. Boundary Layer Transition

In practice, laminar-to-turbulent transition in boundary layers occurs due to the instability of the base flow. Disturbances, such as sound or vorticity, enter the boundary layer and may subsequently get amplified and ultimately lead to turbulence. The conversion from external disturbances into internal modes is called receptivity (Morkovin, 1969). The different routes to turbulence (Morkovin, 1994) are shown in Figure 1.2. Processes 1 and 2 entail the previously mentioned external disturbances forcing and receptivity, respectively. In the case that the amplitude of the entrained disturbance is "small", its growth is described by linear theory. The mechanisms for which linear theory is applicable are highlighted in salmon.

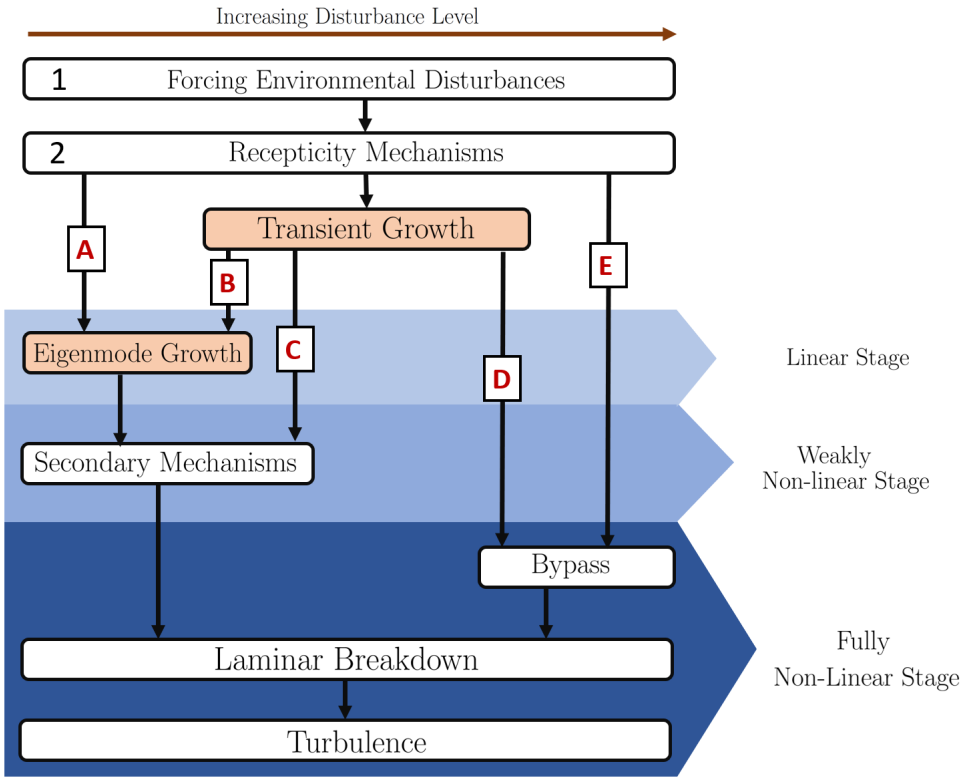

Figure 1.2: Routes to turbulence in shear flows. Morkovin, 1994

The present study focuses on the linear stability of boundary layers with supercritical fluid. Both of the highlighted processes in Figure 1.2 are considered: eigenmode growth and transient growth. Eigenmode growth refers to exponentially growing eigenfunctions and may also be referred to as modal growth or natural transition. If modal growth is dominant then transition occurs through path A in Figure 1.2. This is conventional in low-disturbance environments, and the transition process is associated with mode instabilities (TS wave, Mack modes, mode II), crossflow instability, and Görtler vortices. On this route to turbulence, eigenmode growth is followed by secondary mechanisms, and transition occurs

due to a cascade of successive instabilities: a growing primary instability leads to a modified base flow and the excitation of further instabilities. Regarding transient growth, it considers how perturbations may grow other than exponentially for a finite time. This phenomenon may lead to transition by the excitation of secondary mechanisms (path C) or by triggering non-linear effects and effectively by-passing the (weakly) linear stages (path D). Flows can also experience a competition between modal and non-modal growth. It may be that a boundary layer experiences large non-modal energy growth, but the dynamics of the transient growth mechanism are then surpassed by the exponential growth of modal instabilities - this scenario corresponds to path B. Finally, path E corresponds to a situation where the initial forcing is such that non-linearities are directly excited.

1.2.1. Modal Stability

Early works on the stability of shear flows consider solely the growth of normal modes. Rayleigh's inflection point criterion (Rayleigh, 1880) states a necessary condition for a modal instability in an incompressible, inviscid parallel flow. It was shown that the velocity profile must be inflectional for the existence of an inviscid instability. This result contradicted the prevailing thought that an inviscid flow would always be unstable, and that viscosity acted purely as a stabilizing force. Prandtl (1921) first discovered an otherwise inviscidly stable boundary layer flow to be unstable in the presence of viscous forces. His work was continued by his former students, Walter Tollmien and Hermann Schlichting, who showed the existence of an instability in the Orr-Sommerfeld equation, which describes the modal growth in a parallel viscous flow. When considering an incompressible flat plate boundary layer flow, in the absence of a pressure gradient, and thus of a velocity inflection point, by Rayleigh's criterion viscosity is indispensable in the destabilization of the base flow. A Tollmien-Schlichting (TS) wave takes the form of a wave traveling in the streamwise direction. Schubauer and Skramstad (1947) first observed these waves and demonstrated their connection to transition.

The investigation of compressible boundary layer modal stability started with the work of Lees and Lin (1946). The authors considered a perfect gas. It was proved that, similar to Rayleigh's criterion for incompressible flows, a necessary condition for the existence of an invicidly unstable mode is the presence of a generalized inflection point (GIP), that is, a point within the flow where $D(\rho DU) = 0$, with D representing the wall-normal derivative, ρ the base flow density, and U the base flow velocity. Numerical work by L. Mack (1963, 1964, 1965, 1984) extended compressible theory to the supersonic case. The author revealed the existence of additional unstable modes, referred to as higher modes. These belong to the family of trapped acoustic waves, travelling between the wall and the point at which the wave travels sonically with relation to the base flow. Following Fedorov and Tumin (2011), Mack's higher modes result from the synchronization between fast modes from the continuous spectrum of the fast acoustic branch and the slow mode, such that only one unstable mode (TS, or Mack's higher mode) is present at any given perturbation parameters. Mack's second mode, the first higher mode, is of particular importance as it shows a growth rate higher than the TS mode.

The wall temperature and Mach number are of great importance to the amplification of both the TS mode and Mach's second mode. Wall cooling was found to stabilize the TS mode, as predicted by Lees and Lin, but destabilize the second mode (Mack, 1984, and experimental work by Lysenko and Maslov, 1984). The TS mode is stabilized for high Mach number, with maximum amplification for Mach number lower than unity. The second mode is only present for supersonic flows with Mach number higher than around 2.2, and it is most destabilized for Mach number around 5, (Bitter & Shepherd, 2014). Mack's second mode is preferentially non-skewed, that is, its highest growth rate is observed for 2D waves traveling in the stream-wise direction. Conversely, at high Mach number, sweked waves are the most amplified for the TS mode.

The stabilization/destabilization of the first (TS wave) and second Mack modes have been extensively

studied considering several high temperature effects. M. Malik and Anderson (1991) studied chemical non-equilibrium effects for Mach 10 and 15 boundary layers, that stabilizes the first mode and destabilizes the second mode. Hudson et al. (1997) also considered the hypersonic case and further includes thermal non-equilibrium effects through a vibrational temperature model. Thermal non-equilibrium effects contributed to the further destabilization of the second mode, and to the stabilization of the first.

The effects of viscosity stratification on fluid stability was covered recently in a review paper by Govindarajan and Sahu (2014). Viscosity stratification may be studied by considering two-layer flows. Many studies focus on the interfacial instability, first discovered by Yih (1967) when considering two immiscible layers for a Couette and Poiseuille flow. Given their importance in many engineering applications, for instance in the transportation of crude oil (Joseph et al., 1997), two-layer closed flows have seen the most consideration (Sahu et al., 2009, Joseph et al., 1984). Regarding two-fluid boundary layers, Timoshin and Hooper (2000) and Özgen et al. (1998) studied the effect of parameters such as gravity and surface tension, on the stabilization / destabilization of the TS and interfacial modes.

Studies on dense gas effects are also of particular interest. Gloerfelt et al. (2020) performed linear stability analysis on a boundary layer flow with dense gases. The viscosity is observed to increase from the wall, where the temperature is highest, to the center line (much like a liquid). Moreover, due to high heat capacity, and consequently low value for the average Eckert number, friction heating effects are nearly negligible. At low Mach number the boundary layer is unstable to a single viscous mode (TS wave), preferentially two-dimensional. With an increase of the Mach number the most amplified 2D mode is stabilized, and, for Mach number close to unity, the TS mode becomes most unstable to oblique (3D) waves.

Within the field of supercritical fluid stability, Ren et al. (2019b) studied the linear stability of a CO2 boundary layer near the pseudo-critical line at supercritical pressure of 80 bar. An adiabatic wall boundary condition was prescribed, and viscous heating is controlled by varying the Eckert number. It was shown that, if the temperature profile does not cross the pseudo-critical line, non-ideal effects contribute to the stabilization of the boundary layer. Furthermore, an increase in Eckert number and a proximity of the temperature profile to the pseudo-critical temperature also stabilizes the boundary layer. In the subcriticial regime, for which $T(y) < T_{pc}$, the Mach number was varied between 0.15 and 0.57, and the most unstable TS mode is 2D. Conversely, in the supercritical regime $\left(T(y) > T_{pc}\right)$, the Mach number was varied between 051 and 1.95, and the TS mode was found to be preferentially 3D for the $M_\infty > 0.7$ cases.

Ren et al. (2019b) most striking result occurs in the transcritical regime where the temperature profile crosses the Widom line. In the transcritical case a new mode arises (mode II) in addition to mode I (TS mode). These two unstable modes may coexist, unlike the TS and Mack's higher modes. Within the trancritical regime, an increase in Eckert leads to the increase of the height of the Widom line and greater temperature stratification, which result in the further destabilization of the flow, particularly mode II. The growth rate of mode II is much greater than mode I - one order of magnitude higher. Mode II is associated with a GIP and thus inviscidly unstable. However, mode II is not acoustic, and hence not connected to Mack's second mode. Also, unlike mode 2, dispite being inviscidly unstable, mode II is most amplified for finite Reynolds number, such that viscosity contributes towards its amplification.For a transcritical case with moderate Mach number of 0.66, mode II was observed to be preferentially two-dimensional, and mode I is three-dimensional.

Recently, Bugeat et al. (2022) considered the transcritical regime for a boundary layer flow. The Van der Waals equation of state is employed, the wall is heated (isothermal), and the limiting case of Eckert/Mach number zero ($M_\infty = Ec_\infty = 0$) is considered. Mode II is recovered in this approach, bringing to light its significance to a more general class of fluids. Furthermore, mode II is directly linked to the crossing of the Widom line. Under the assumption that viscosity effects dominate the balance

of streamwise momentum of the base flow, the authors link the presence of a GIP to the strong local gradients of dynamic viscosity, and a minimum of kinematic viscosity. Additionally, the authors suggest that mode II could be recovered for a Couette flow, which could provide a more canonical framework for its study.

1.2.2. Non-Modal Stability

Despite the success of eigenmode analysis, in many cases it fails to capture experimentally observed phenomena. For instance, modal stability predicts that incompressible Couette flow is stable for all Reynolds numbers. Moreover, many flows are observed to be unstable well below the computed critical Reynolds number from modal theory, including boundary layer flows (Schmid, 2007). In comparison to modal analysis, the non-modal framework is quite novel, and the body of literature significantly shorter. Until very recently (1990s) transition phenomena which could not be explained by eigenmode analysis was often labeled as bypass transition. Non-modal linear stability gives a plausible explanation to the observed transition of flows that are modally stable. Consider that a perturbation imposed on the base flow grows algebraically for a finite time, and by triggering non-linear effects leads to turbulence. In such a case, modal analysis, and in particular the most unstable mode, do not provide any insight into the dynamics of transition.

Non-modal instabilities begun to be uncovered through the work of Ellingsen and Palm (1975). The authors considered a bounded parallel flow, assumed inviscid, incompressible and non-stratified. It was shown that three-dimensional disturbances, independent of the x-direction, may grow linearly in time. Landahl (1980) considered the temporal framework for an inviscid shear flow. It was shown that the stream-wise extension of a 3D disturbance grows linearly with time, and, asymptotically, the stream-wise velocity perturbation remains bounded. Therefore, elongated streaks evolve in a shear layer. The physical mechanism behind the formation of these elongated streaks is called the lift-up effect. This mechanism is most commonly explained by the redistribution of stream-wise momentum in the wall-normal direction. An initial disturbance consisting of stream-wise vortex streaks transport high velocity fluid, far from the wall, towards a region of low velocity fluid near the wall. Vice-versa, slow moving fluid close to the wall is push towards a region of higher fluid velocity. Fluid particles initially retain their stream wise momentum, hence this interaction results in stream wise velocity fluctuations along the span-wise direction.

The early work that follow focused on the non-modal growth of incompressible shear flows as this mechanism for transient growth provides an explanation for the experimentally observed transition of flows that are modally stable (Gustavsson, 1991, Henningson et al., 1993, Schmid and Henningson, 1994, etc.). Hanifi et al. (1996) first employed the transient growth setting to a perfect gas compressible boundary layer. The optimal initial perturbations, similarly to the incompressible case, are stream-wise vortices. These evolve into elongated streaks (lift-up mechanism). The authors also conclude that, just as observed in closed Couette and Poiseuille flows (Gustavsson, 1991, and Reddy and Henningson, 1993), the non-modal energy growth scales with the square of the Reynolds number Re_δ^2 and the time of maximum amplification with Re_δ. The works of Tumin and Reshotko (2001) and Bitter and Shepherd (2014) consider the parallel flow approximation and the spatial setting. In both cases the lift-up effect is responsible for large energy growth. For an adiabatic wall, an increase in Mach number leads to an increase of the maximum energy growth. While at zero Mach number only kinetic effects are responsible for energy growth, with increasing Mach the flow becomes progressively more temperature and density stratified, and non-kinetic effects contribute more towards the transient growth. However, under a norm which keeps pressure work conservative (Mack's energy norm), it is observed that for an ideal gas cases, even for a hypersonic flow with $\mathrm{M}_\infty = 5$, the temperature/density perturbations have a minimal contribution towards the optimal energy growth for stationary waves. Indeed, for adiabatic conditions,

an increase in the Mach number results in a slight increase of the maximum energy growth. The energy growth is higher when the wall and free-stream temperatures differ, such that generally, for a given Mach number, the energy growth is minimum for an isothermal wall at the same temperature as the free-stream. When considering an isothermal wall, an increase of the Mach number generally leads to a decrease of the maximum energy growth.

In regard to strongly stratified flows, Parente et al. (2020) conducted modal and non-modal stability analysis on a stably stratified Blasius boundary layer. The temporal framework is employed. The authors investigated the effect of varying Prandtl, Reynolds and Richardson number. The latter representing the ratio of the buoyancy effect and flow shear effects. An increase in the Richardson lead to a decrease of the optimal energy growth. Notably, for the finite Richardson number cases, the optimal stream-wise wave number is considerably different from zero, that is, the optimal condition is a stream-wise varying perturbation. Additionally, the optimum growth scales linearly with the Reynolds number. These finding suggest that both the Orr mechanism and the lift-up effect are at play.

The number of studies regarding the transient growth of mixing layer or two-fluid boundary layers is limited. The work of Yecko and Zaleski (2005) explores the non-modal stability of a two-phase mixing layer of immiscible fluids. The evolutions of the energy growth with time may feature oscillations due to interfacial modes, these may be of comparable magnitude. The optimal initial perturbation consists of two vertically aligned counter-rotating stream-wise vortices. At the interface the initial perturbation consists of a span-wise velocity (with zero wall normal component), and the two vortexes have their centre above and below the liquid-gas interface. The resulting perturbation consists of stream-wise velocity streaks local with maximums vertically aligned with the centres of the vortexes.

A study on algebraic growth for a supercritical CO2 Poiseuille flow was recently carried out by Ren et al. (2019a). In the limit of zero Eckert number the flow becomes isothermal, and transient growth analysis yields the usual streamwise vortices and streaks, much like for the ideal gas case. Furthermore, the authors compared non-modal growth for varying wall temperatures and numbers of (Pr Ec). Independently of these parameters, the largest energy amplification is obtained for oblique stream-wise independent perturbations, just as in the ideal gas case. While in the subcritical regime, an increase in (Pr Ec) contributes to the destabilization of the non-ideal flow, in the supercritical regime it contributes to its stabilization. Optimal initial and resulting disturbances remain generally unchanged between ideal and non-ideal cases. These correspond, once again, to vortices and velocity streaks aligned in the streamwise direction. A notable difference in the transcritical regime is the amplitude of the thermal streak, which is much larger close to the wall.

1.3. Research Objective

In the present work, the modal and non-modal stability of SCO2 boundary layers near its Widom point is analysed. The research objectives are summarized bellow:

1. To investigate the effect of Mach number on the amplification of oblique waves.

2. To investigate the transient growth of zero Mach number boundary layers near the fluid's pseudo-boiling point.

Regarding objective *1.*, while previous works on the modal stability of mode I show that for low

Mach number mode I is preferentially 2D, at Mach number higher than around 0.7 mode I becomes most amplified for oblique waves (Gloerfelt et al., 2020, Mack, 1984, Ren et al., 2019b). Despite the apparent link between Mach number and the three-dimensional character of mode I, this is often not made explicit. In the case of mode II, its three-dimensionality has yet to be studied. The present work investigates the three-dimensionality of mode I and mode II. In the case of mode II, given its inviscid nature, the analysis is extended to the inviscid regime, leading to the simplification of the governing equations. Within this framework, the three-dimensionality of mode II is linked explicitly to the base flow's Mach number.

Regarding the non-modal energy growth of boundary layers. In the sub- and supercritical regimes the boundary layers are close to ideal, as such their non-modal behaviour is expected to be similar to what is observed for an ideal gas. Conversely, in the transcritical regime, the base flow profiles are far from ideal. The velocity profiles are highly modulated when compared to an ideal gas case, and, due to the modified velocity profile, the growth of kinetic energy may feature different structures. This is observed in a mixing layer, see Yecko and Zaleski (2005). Moreover, due to the strong density stratification, especially at the Widom point, the non-kinetic terms may contribute significantly to the perturbation energy composition. As a final point of interest, in an ideal gas boundary layer, the interaction between continuous modes and the TS mode can lead to significant transient growth. In the transcritical scenario, where both the TS mode (mode I) and mode II are simultaneously present, interactions between these two modes, along with the potential involvement of additional modes from the continuous eigenspectrum, may result in substantial transient growth.

1.4. Thesis Lay-out

Chapter 2 – Theoretical Framework, introduces the governing equation for a fluid flow, and specifically the equations which govern a self-similar zero-pressure gradient flat-plate boundary layer flow. Further, the linear operator governing the dynamics of a growing perturbation is presented.

Chapter 3 – Numerical Methods and Validation, presents the numerical methods used to solve for the boundary layer flows under investigation, and the perturbations. In addition, the code employed in the present work is validated.

Chapter 4 – Results: Modal Stability Analysis, presents and analyses the stability results under normal-mode stability, i.e., asymptotic stability.

Chapter 5 – Results: Non-Modal Stability Analysis, presents and analyses the stability results under the non-modal approach, i.e. the presence of transient energy growth.

Chapter 6 – Conclusion, summarizes the main outcomes of the research. Provides recommendations for future work.

2

Theoretical Framework

2.1. Governing Equations

The dynamics of a compressible viscous single-phase fluid are described by the Navier-Stokes equations. These are expressed, in differential and dimensionless form, as

$$\begin{cases} \dfrac{\partial \rho}{\partial t} + \dfrac{\partial \rho u_i}{\partial x_i} = 0, \\ \rho \left(\dfrac{\partial u_i}{\partial t} + u_j \dfrac{\partial u_i}{\partial x_j} \right) + \dfrac{1}{\mathrm{M}_\infty^2} \dfrac{\partial p}{\partial x_i} - \dfrac{1}{\mathrm{Re}_\delta} \dfrac{\partial \tau_{ij}}{\partial x_j} = 0, \\ \rho \left(\dfrac{\partial e}{\partial t} + u_j \dfrac{\partial e}{\partial x_j} \right) + \dfrac{\mathrm{Ec}_\infty}{\mathrm{M}_\infty^2} p \dfrac{\partial u_j}{\partial x_j} - \dfrac{\mathrm{Ec}_\infty}{\mathrm{Re}_\delta} \dfrac{\partial u_i \tau_{ij}}{\partial x_j} + \dfrac{1}{\mathrm{Re}_\delta \mathrm{Pr}_\infty} \dfrac{\partial q_j}{\partial x_j} = 0, \end{cases} \tag{2.1}$$

where t is time, $x_i = (x, y, z)$ are the Cartesian coordinates in the streamwise, wall-normal and span-wise directions, respectively, and $u_i = (u, v, w)$ are the velocity components in the corresponding directions. The fluid's density, pressure, and internal energy are indicated by ρ, p and e, respectively. The viscous stress tensor (τ) is

$$\tau_{ij} = \mu \left(\frac{\partial u_i}{\partial x_j} + \frac{\partial u_j}{\partial x_i} \right) + \lambda \delta_{ij} \frac{\partial u_k}{\partial x_k}, \tag{2.2}$$

where δ_{ij} is the Kronecker delta, μ stands for the dynamic viscosity and $\lambda = \mu_b - 2/3\mu$ is the second viscosity, with μ_b being the bulk viscosity. As shown by Ren et al. (2019a), the effect of the bulk viscosity μ_b on the linear stability of a SCO2 channel flow is negligible, and thus it is set to zero for the present analysis.

The heat flux vector (q) is

$$q_i = -\kappa \frac{\partial T}{\partial x_i}, \tag{2.3}$$

where κ is the thermal conductivity and T the fluid's temperature.

The governing equations are shown in dimensionless form. They are made dimensionless using the definitions

$$(u,\, v,\, w) = \frac{(u^*,\, v^*,\, w^*)}{u_\infty^*}\,, \quad (x,\, y,\, z) = \frac{(x^*,\, y^*,\, z^*)}{\delta^*}\,, \quad t = \frac{t^* u_\infty^*}{\delta^*}\,, \quad p = \frac{p^*}{\rho_\infty^* a_\infty^{*2}}\,, \quad e = \frac{e^*}{C_{p_\infty}^* T_\infty^*}\,, \tag{2.4}$$

where the asterisk $(\cdot)^*$ represents a dimensional quantity, a is the speed of sound, and C_p the specific

heat capacity at constant pressure. The length scale δ^* is the local Blasius length scale:

$$\delta^* = \sqrt{\frac{\mu^*_\infty x^*}{\rho^*_\infty u^*_\infty}}. \tag{2.5}$$

The remaining thermodynamic and transport properties are non-dimensionalized using their value at the free stream, for example, the non-dimensional density is $\rho = \rho^*/\rho^*_\infty$. The non-dimensional numbers are

$$\mathrm{Re}_\delta = \frac{\rho^*_\infty u^*_\infty \delta^*}{\mu^*_\infty}, \quad \mathrm{M}_\infty = \frac{u^*_\infty}{a^*_\infty} \quad \mathrm{Ec}_\infty = \frac{u^{*2}_\infty}{C^*_{p_\infty} T^*_\infty}, \quad \mathrm{Pr}_\infty = \frac{C^*_{p_\infty}\mu^*_\infty}{\kappa^*_\infty}. \tag{2.6}$$

Finally, unless stated otherwise, fluid properties are calculated based on the NIST REFPROP library (Lemmon et al., 2018). These are required in order to solve the base boundary-layer flow and the stability analysis, which will be discussed in sections 2.2 and .2.3.

2.2. Steady-State Boundary Layer Flow

The base flow under consideration is a self-similar 2D zero-pressure gradient flat-plate boundary-layer flow, under no gravitational forces, necessarily stationary. The governing equations are

$$\begin{cases} \dfrac{\partial \rho u}{\partial x} + \dfrac{\partial \rho v}{\partial y} = 0, \\ \rho\left(u\dfrac{\partial u}{\partial x} + v\dfrac{\partial u}{\partial y}\right) - \dfrac{\partial}{\partial y}\left[\dfrac{\mu}{\mathrm{Re}_\delta}\dfrac{\partial u}{\partial y}\right] = 0, \\ \dfrac{\partial p}{\partial y} = 0, \\ \rho\left(u\dfrac{\partial h}{\partial x} + v\dfrac{\partial h}{\partial y}\right) - \dfrac{\mu}{\mathrm{Re}_\delta}\left(\dfrac{\partial u}{\partial y}\right)^2 - \dfrac{1}{\mathrm{Pr}_\infty \mathrm{Re}_\delta}\dfrac{\partial}{\partial y}\left(\kappa\dfrac{\partial T}{\partial y}\right) = 0, \end{cases} \tag{2.7}$$

where h is the static enthalpy, which equals $h = e + \left(\mathrm{Ec}_\infty/\mathrm{M}^2_\infty\right)(p/\rho)$, and is non-dimensionalized with $C^*_{p_\infty} T^*_\infty$. The derivation of the system 2.7 can be found in M. Malik and Anderson (1991).

A self-similar boundary layer is considered. The Lees-Dorodnitsyn transformation is employed

$$\xi = \int_0^x \rho^*_\infty \mu^*_\infty u^*_\infty dx^*, \qquad \eta = \frac{u^*_\infty}{\sqrt{2\xi}} \int \frac{\rho^*}{\rho^*_\infty} dy^*, \tag{2.8}$$

resulting in the set of ordinary differential equations (ODE)

$$\begin{cases} \dfrac{\partial}{\partial \eta}\left(C\dfrac{\partial^2 f}{\partial \eta^2}\right) + f\dfrac{\partial^2 f}{\partial \eta^2} = 0 \\ f\dfrac{\partial g}{\partial \eta} + \dfrac{\partial}{\partial \eta}\left(\dfrac{C}{\mathrm{Pr}}\dfrac{\partial g}{\partial \eta}\right) + C\dfrac{u^{*2}_\infty}{h^*_\infty}\left(\dfrac{\partial^2 f}{\partial \eta^2}\right)^2 = 0 \end{cases} \tag{2.9}$$

with

$$\frac{\partial f}{\partial \eta} = \frac{u^*}{u^*_\infty}, \quad g = \frac{h^*}{h^*_\infty}, \quad C = \frac{\rho^*\mu^*}{\rho^*_\infty \mu^*_\infty} \quad \mathrm{Pr} = \frac{C^*_p \mu^*}{\kappa^*} \tag{2.10}$$

and boundary conditions

$$f(0) = 0, \quad \frac{\partial f(0)}{\partial \eta} = 0, \quad \frac{\partial f(\eta \to \infty)}{\partial \eta} = 1, \quad \frac{\partial g(\eta \to \infty)}{\partial \eta} = 1. \tag{2.11}$$

Regarding the wall boundary condition for the dimensionless enthalpy g, two cases may be considered, an adiabatic wall for which

$$\frac{\partial g(0)}{\partial \eta} = 0 \tag{2.12}$$

or an isothermal wall with

$$g(0) = g_w \tag{2.13}$$

where g_w is the dimensionless enthalpy at the wall. The derivation of the preceding equations 2.7 and 2.9 can be found in the standard text books such as Anderson (1989).

2.3. Linear Stability Analysis

Stability theory is concerned with the response of a dynamical system to a small perturbation around a stationary solution. Consider that the state vector q is decomposed into a steady-state solution $\bar{q}$ and a perturbation q': $q = \bar{q} + q'$. The dynamical system under consideration is non-linear, as governed by the Navier-Stokes equations (Equation 2.1). Expressed in dynamical system form:

$$\frac{\partial q}{\partial t} = \mathcal{N}(q) \tag{2.14}$$

where $\mathcal{N}$ is the Navier-Stokes operator. The stationary solution $\bar{q}$ is the laminar boundary-layer flow, which satisfies Equation 2.7. Note that, as a steady-state solution, $\frac{\partial \bar{q}}{\partial t} = \mathcal{N}(\bar{q}) = 0$. The evolution of the perturbation q' is governed by

$$\frac{\partial q'}{\partial t} = \mathcal{N}(\bar{q} + q'). \tag{2.15}$$

In linear stability analysis, the assumption is made that the perturbation q' is small: $q' \sim O(\varepsilon)$, $\varepsilon \ll 1$. Neglecting the terms of order $O(\varepsilon^2)$ in Equation 2.15 yields a linear system in q', and can be expressed as

$$\frac{\partial q'}{\partial t} = \mathcal{L}(\bar{q})q' \tag{2.16}$$

where $\mathcal{L} = \left(\frac{\partial \mathcal{N}}{\partial q}\right)_{\bar{q}}$ is the linearized Navier-Stokes operator. For the sake of completeness, the linear stability equations are written in their full form as:

- Conservation of mass:

$$\frac{\partial \rho'}{\partial t} + \bar{\rho}(\nabla \cdot \underline{u}') + U\frac{\partial \rho'}{\partial x} + v'\frac{\partial \bar{\rho}}{\partial y} = 0 \tag{2.17a}$$

• Conservation of momentum

$$\begin{aligned}\bar{\rho}\left(\frac{\partial \underline{u}'}{\partial t}+U\frac{\partial \underline{u}'}{\partial x}+v'\frac{\partial \bar{\underline{u}}}{\partial y}\right)+\frac{1}{\mathrm{M}_\infty^2}\nabla p' = \\ =\frac{1}{\mathrm{Re}_\delta}\Big[\bar{\mu}\nabla^2\underline{u}'+\mu'\frac{\partial^2 U}{\partial y^2}\vec{e}_x+ \\ +\bar{\mu}\nabla(\boldsymbol{\nabla}\cdot\underline{u}')+ \\ +\frac{\partial\mu}{\partial y}\left(\frac{\partial \underline{u}'}{\partial y}+\nabla v'\right)+\frac{\partial U}{\partial y}\left(\frac{\partial\mu'}{\partial y}\vec{e}_x+\frac{\partial\mu'}{\partial x}\vec{e}_y\right)+ \\ +\bar{\lambda}\nabla\left(\boldsymbol{\nabla}\cdot\underline{u}'\right)+\left(\boldsymbol{\nabla}\cdot\underline{u}'\right)\nabla\bar{\lambda}\Big]\end{aligned} \tag{2.17b}$$

• Conservation of energy

$$\begin{aligned}\bar{\rho}\left(\frac{\partial e'}{\partial t}+U\frac{\partial e'}{\partial x}+v'\frac{\partial \bar{e}}{\partial y}\right)= \\ -\frac{\mathrm{Ec}_\infty}{\mathrm{M}_\infty^2}\bar{p}\left(\nabla\cdot\underline{u}'\right) \\ +\frac{\mathrm{Ec}_\infty}{\mathrm{Re}_\delta}\left[\left(\frac{\partial U}{\partial y}\right)^2\mu'+2\bar{\mu}\frac{\partial U}{\partial y}\left(\frac{\partial v'}{\partial x}+\frac{\partial u'}{\partial y}\right)\right] \\ +\frac{1}{\mathrm{Re}_\delta\mathrm{Pr}_\infty}\left[\bar{k}\nabla^2T'+\frac{\partial\bar{k}}{\partial y}\frac{\partial T'}{\partial y}+k'\frac{\partial^2\bar{T}}{\partial y^2}+\frac{\partial k'}{\partial y}\frac{\partial\bar{T}}{\partial y}\right]\end{aligned} \tag{2.17c}$$

where $\bar{(\cdot)}$ pertains to base flow quantities and $(\cdot)'$ to perturbation quantities. Additionally, the base flow is assumed parallel with $\bar{\underline{u}} = U\vec{e}_x$, and $\underline{u}'$ is the perturbation velocity field $\underline{u}' = (u', v', w')$.

As thermodynamic and transport properties are inter-dependent, the state vector is reduced to $q = [p, u, v, w, T]^T$. Perturbation quantities for other thermodynamic and transport properties can be obtained from p' and T'. The remaining thermodynamic and transport properties of interest, a first order Taylor series expansion is used. For example, the density perturbation is calculated by

$$\rho' = \left(\frac{\partial\rho}{\partial p}\right)_T\Big|_{\bar{q}}p'+\left(\frac{\partial\rho}{\partial T}\right)_p\Big|_{\bar{q}}T' \tag{2.18}$$

For convenience, Equation 2.16 is written in the matrix form as

$$\begin{aligned}\mathcal{L}_t\frac{\partial q'}{\partial t}+\mathcal{L}_x\frac{\partial q'}{\partial x}+\mathcal{L}_y\frac{\partial q'}{\partial y}+\mathcal{L}_z\frac{\partial q'}{\partial z}+\mathcal{L}_{q'}q'+ \\ +\mathcal{L}_{xx}\frac{\partial^2 q'}{\partial x^2}+\mathcal{L}_{yy}\frac{\partial^2 q'}{\partial y^2}+\mathcal{L}_{zz}\frac{\partial^2 q'}{\partial z^2}+\mathcal{L}_{xy}\frac{\partial^2 q'}{\partial x\partial y}+\mathcal{L}_{xz}\frac{\partial^2 q'}{\partial x\partial z}+\mathcal{L}_{yz}\frac{\partial^2 q'}{\partial y\partial z}=0,\end{aligned} \tag{2.19}$$

and the non-zero terms of the above 5×5 base-flow matrices are given in appendix A.

In the context of 1D linear stability theory, the perturbation q' is decomposed in Fourier modes in time, with frequency ω, and in the $x-$, and $z-$ directions, with wave numbers α and β, respectively:

$$q' = \tilde{q}(y)e^{i(\alpha x+\beta z-\omega t)}+\text{c.c.}, \tag{2.20}$$

and the perturbation is inhomogeneous in the y-direction.

The wave numbers α and β and the frequency ω are dimensionless, with reference values δ^* for the wave numbers and δ^*/u_∞^* for the frequency. Note that the Blasius length scale (δ^*) increases with the

streamwise coordinate x. Therefore, for a given physical perturbation, the dimensionless frequency ω changes as the perturbation travels downstream. The dimensionless parameter F, which is constant for a perturbation with frequency f^* in Hz, is introduced:

$$F = \frac{2\pi f^* \mu_\infty^*}{\rho_\infty^* u_\infty^{*2}} = \frac{\omega}{\mathrm{Re}_\delta} \tag{2.21}$$

A similar rationale is applied to the wave number β and a dimensionless parameter B is considered:

$$B = \frac{\beta^* \mu_\infty^*}{\delta^* \rho_\infty^* u_\infty^*} = \frac{\beta}{\mathrm{Re}_\delta} \tag{2.22}$$

Regarding Equation 2.19, and making use of Equation 2.20 yields

$$\left(\alpha^2 \mathcal{A}_{\alpha^2} + \alpha \mathcal{A}_\alpha + \omega \mathcal{A}_\omega + \mathcal{A}_0\right) \tilde{q} = 0 \tag{2.23}$$

where

$$\begin{aligned} \mathcal{A}_0 &= i\beta \mathcal{L}_z + \mathcal{L}_{q'} - \beta^2 \mathcal{L}_{zz} + (\mathcal{L}_y + i\beta \mathcal{L}_{yz}) \frac{\partial}{\partial y} + \mathcal{L}_{yy} \frac{\partial^2}{\partial y^2} \\ \mathcal{A}_\omega &= -i\mathcal{L}_t \\ \mathcal{A}_\alpha &= i\mathcal{L}_x - \beta \mathcal{L}_{xz} + i\mathcal{L}_{xy} \frac{\partial}{\partial y} \\ \mathcal{A}_{\alpha^2} &= -\mathcal{L}_{xx} \end{aligned} \tag{2.24}$$

For a locally convectively unstable flow, such as a flat-plate boundary layer, spatial theory is commonly applied, where the frequency ω and the spanwise wave number β are real and the streamwise number α is complex, such that the perturbation can be considred to grow in x-direction. Then, Equation 2.23 forms a second order eigenvalue problem for the complex eigenpair α and $\tilde{q}$.

The boundary conditions of the eigenvalue problem resulting from Equation 2.23 are

$$\begin{aligned} \tilde{u} = \tilde{v} = \tilde{w} = 0, \quad y = 0 \\ \tilde{u} = \tilde{v} = \tilde{w} = \tilde{T} = 0, \quad y \to \infty \end{aligned} \tag{2.25}$$

Additionally, the temperature perturbation boundary condition at the wall follows the boundary condition employed for the base flow (Equation 2.12 or 2.13):

$$\begin{aligned} \text{if} \quad g(0) = g_w, \quad \tilde{T} = 0, \quad y = 0 \\ \text{if} \quad \frac{\partial g(0)}{\partial \eta} = 0, \quad \frac{\partial \tilde{T}}{\partial y} = 0, \quad y = 0 \end{aligned} \tag{2.26}$$

2.3.1. Inviscid Analysis

In the limit of infinitely large Reynolds number ($\mathrm{Re}_\delta \to \infty$), Equation 2.19 can be simplified to

$$\bar{\rho} i \left(\alpha U - \omega\right) \tilde{v} = -\frac{1}{\mathrm{M}_\infty^2} \frac{\partial \tilde{p}}{\partial y} \tag{2.27a}$$

$$\bar{\rho} i \left(\alpha U - \omega\right) \frac{\partial \tilde{v}}{\partial y} = i\alpha \bar{\rho} \frac{\partial U}{\partial y} \tilde{v} + \left(\alpha^2 + \beta^2\right) \left[\mathrm{M}_\mathrm{r}^2 - 1\right] \frac{1}{\mathrm{M}_\infty^2} \tilde{p} \tag{2.27b}$$

where $\mathrm{M_r}$ is the relative Mach number defined as

$$\mathrm{M_r} = \frac{\mathrm{M}_\infty\,(\alpha U - \omega)}{\bar{a}\sqrt{(\alpha^2+\beta^2)}} = \frac{\mathrm{M}_\infty}{\bar{a}}\,(U\cos(\theta') - c)\,, \tag{2.28}$$

where $\bar{a}$ is speed of sound of the mean flow, which is non-dimensionalized with the speed of sound in the free-steam, c is the wave's phase speed $c = \omega/\sqrt{\alpha^2+\beta^2}$, and θ' represents the perturbation's propagation angle $\theta' = \arctan(\beta/\alpha)$. Consider briefly a 2D flow, the relative Mach number is

$$\mathrm{M_r} = \frac{\mathrm{M}_\infty\,(\alpha U + \beta W - \omega)}{\bar{a}\sqrt{(\alpha^2+\beta^2)}}, \tag{2.29}$$

where W is the base flow velocity in the y-direction. The relative Mach number may also be expressed as

$$\mathrm{M_r} = \frac{\mathrm{M}_\infty}{\bar{a}}\cos(\theta)\left(\sqrt{U^2+W^2} - c_{\bar{u}}\right), \tag{2.30}$$

where the angle θ represents the deviation between the base flow's propagation direction and the phase speed of the wave perturbation, and $c_{\bar{u}}$ denotes the speed at which the wavefront travels in the axis oriented along the base flow velocity, given by

$$c_{\bar{u}} = \frac{w}{\sqrt{\alpha^2+\beta^2}}\frac{1}{\cos(\theta)} = \frac{w}{\alpha\cos\bar{\theta} + \beta\sin\bar{\theta}}, \quad \text{where} \quad \bar{\theta} = \arctan\left(\frac{W}{U}\right). \tag{2.31}$$

This is illustrated in Figure 2.1. The intersection between the wavefront, with phase speed $c = \omega/\sqrt{\alpha^2+\beta^2}$ and shown in orange, with the axis oriented along the mean flow direction ($\bar{u}$), travels at speed $c_{\bar{u}}$.

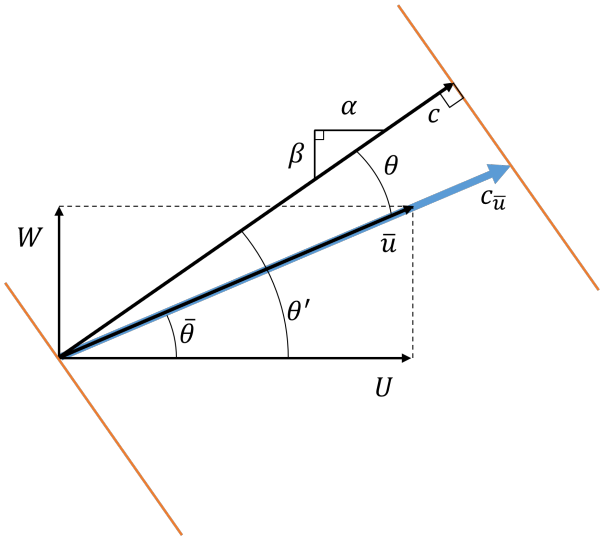

Figure 2.1: Illustration of relevant quantities for the relative Mach number. The angle $\theta = \pm(\theta' - \bar{\theta})$, represents the deviation between the base flow's propagation angle ($\bar{\theta}$) and the phase speed angle θ'. The orange lines represent a wave front, traveling with phase speed c.

In the case of a 1D base flow, Equation 2.30 reduces to

$$\mathrm{M_r} = \frac{\mathrm{M}_\infty}{\bar{a}}\cos(\theta')\,(U - c_x)\,, \quad \text{where} \quad c_x = \omega/\alpha. \tag{2.32}$$

The quantity c_x will prove be useful in the upcoming analysis.

For the inviscid system in Equations 2.27a and 2.27b, the state vector is reduces to $\tilde{q}^{\mathrm{INV}} = [\tilde{p}, \tilde{v}]$. In

matrix form the system 2.23 reads

$$\left(\alpha^2 \mathcal{A}^{\mathrm{INV}}_{\alpha^2} + \omega^2 \mathcal{A}^{\mathrm{INV}}_{\omega^2} + \alpha\omega \mathcal{A}^{\mathrm{INV}}_{(\alpha\omega)} + \alpha \mathcal{A}^{\mathrm{INV}}_{\alpha} + \omega \mathcal{A}^{\mathrm{INV}}_{\omega} + \mathcal{A}_0\right) \tilde{q}^{\mathrm{INV}} = 0 \tag{2.33}$$

The non-zero terms of the above 2×2 base-flow matrices are given in appendix A. Since at the wall, the wall-normal perturbation velocity $\tilde{v}$ is zero, given Equation 2.27a, $D\tilde{p} = 0$. Thus, in the inviscid case, the boundary conditions are

$$\begin{aligned} \tilde{v} = \frac{\partial \tilde{p}}{\partial y} = 0, \quad y = 0 \\ \tilde{v} = \tilde{p} = 0, \quad y \to \infty \end{aligned} \tag{2.34}$$

In the context of inviscid stability, an important property of the base flow is the presence of a generalized inflection point, that is, a point within the boundary layer where

$$\frac{\partial}{\partial y}\left(\bar{\rho}\frac{\partial U}{\partial y}\right) = 0 \tag{2.35}$$

Denote by y_s the height of the GIP, that is, the point at which Equation 2.35 is satisfied. For a subsonic perturbation, that is $M_r^2 < 1$, Lees and Lin (1946) show that the existence of a GIP is a sufficient and necessary condition for the presence of an inviscid neutral instability, if $y_s > y_0$, where y_0 is the point at which $U = 1 - 1/\mathrm{M}_\infty$. Also, the phase velocity $c_x = \omega/\alpha$ of this neutral wave is $(c_x)_s = U_s = U(y_s)$.

2.3.2. Non-Modal Stability

Classically, linear stability theory is concerned with the asymptotic fate of a perturbation. This framework is referred to by modal stability. Since asymptotic behaviour is governed by the eigenvalues of Equation 2.23, the modal problem reduces to finding unstable solutions to the eigenvalue problem 2.23. Within the spatial framework, unstable satisfy $\alpha_i < 0$, such that the perturbation grows exponentially in the x-direction. Conversely, non-modal stability is concerned with the transient behaviour of a perturbation. Due to the non-normality of the linearized NS operator, a significant growth may occur before the subsequent exponential behaviour.

While modal stability is realized by finding the solutions to the eigenvalue problem in Equation 2.23, the non-modal analysis is mathematically more complex. The approach in Tumin and Reshotko (2001) is closely followed. A perturbation solution to Equation 2.16 is expressed by an eigenvector expansion

$$q' = \sum_{k=1}^{n} \kappa_k \, \tilde{q}_k(y) \, e^{i(\alpha_k x + \beta z - \omega t)} \tag{2.36}$$

where κ_k are the expansion coefficients, and $(\tilde{q}_k, \alpha_k)$ the k-th eigenpair. Only the first n eigenvectors are considered, meaning that the state vector space is restricted to the space spanned by the first n eigenvectors. The choice of eigenvectors considered in Equation 2.36, and hence the parameter n, is explored in Chapter 3. In matrix form, Equation 2.36 reads

$$q' = \mathbf{Q}\,\mathbf{\Lambda}\,\kappa\, e^{i(\beta z - \omega t)} \tag{2.37}$$

where, the matrix $\mathbf{Q}$ contains the first n eigenvectors, $\mathbf{\Lambda}$ is a diagonal matrix with $\mathbf{\Lambda}_{j,j} = \exp\left(i\,\alpha_j\,x\right)$, and the vector κ contains the expansion coefficients.

The growth of the perturbation q' is given by

$$g(x) = \frac{\|q'(x)\|_E^2}{\|q_0'\|_E^2} \tag{2.38}$$

where $\|\cdot\|_E$ stands for the energy norm. The conversion to an Euclidian norm ($\|\cdot\|_2$) is obtained by considering a matrix $\mathbf{W}$, which can be arbitrarily chosen, containing the necessary weights such that

$$\|q'\|_E = \int_0^\infty q'^H \mathbf{W} q' \partial y = \|\mathbf{M} q'\|_2 \tag{2.39}$$

with $\mathbf{M}$ resulting from a Cholesky decomposition of $\mathbf{W} = \mathbf{M}^H\mathbf{M}$. The choice of the weights $\mathbf{W}$ is left to Section 2.3.2.

Interest lies in the maximum obtainable amplification, and its corresponding initial perturbation. The maximum energy amplification G at position x is given by

$$G(x) = \max_{q_0'} g(x) = \max_{\kappa} \frac{\|\mathbf{M}\mathbf{Q}\mathbf{\Lambda}\kappa\|_2^2}{\|\mathbf{M}\mathbf{Q}\kappa\|_2^2} = \max_{\mathbf{F}\kappa} \frac{\left\|\mathbf{F}\mathbf{\Lambda}\mathbf{F}^{-1}\mathbf{F}\kappa\right\|_2^2}{\|\mathbf{F}\kappa\|_2^2} = \left\|\mathbf{F}\mathbf{\Lambda}\mathbf{F}^{-1}\right\|_2^2 \tag{2.40}$$

where the matrix $\mathbf{F}$ results from the Cholesky decomposition $\mathbf{F}^H\mathbf{F} = (\mathbf{M}\mathbf{Q})^H\,\mathbf{M}\mathbf{Q}$.

Consider the singular value decomposition of the matrix $\mathbf{F}\mathbf{\Lambda}\mathbf{F}^{-1}$

$$\mathbf{F}\mathbf{\Lambda}\mathbf{F}^{-1} = \mathbf{U}\mathbf{\Sigma}\mathbf{V}^{-1} \tag{2.41}$$

where $\mathbf{V}$ and $\mathbf{U}$ are unitary matrices and $\mathbf{\Sigma}$ is diagonal, containing the singular values. The Euclidian norm of $\mathbf{F}\mathbf{\Lambda}\mathbf{F}^{-1}$ is equal to its largest singular value, denoted σ_1 $\left(\left\|\mathbf{F}\mathbf{\Lambda}\mathbf{F}^{-1}\right\|_2^2 = \sigma_1\right)$. Furthermore, the right and left singular vectors associated with σ_1 satisfy

$$\mathbf{F}\mathbf{\Lambda}\mathbf{F}^{-1}\, v_1 = \sigma_1 u_1 \tag{2.42}$$

The operator $\mathbf{F}\mathbf{\Lambda}\mathbf{F}^{-1}$ maps the right singular vector v_1 onto u_1, while increasing its amplitude by σ_1. Therefore, considering equations 2.37 and 2.40, the maximum amplified perturbation at position x, denoted by q'_{out}, is

$$q'_{\text{out}} = \mathbf{Q}\mathbf{F}^{-1}u_1 \tag{2.43}$$

and the associated initial perturbation, denoted by q'_{in} is

$$q'_{\text{in}} = \mathbf{Q}\mathbf{F}^{-1}v_1 \tag{2.44}$$

For any considered frequency ω and wave number β, the energy amplification $G(x)$ is maximized over all x and denoted by $G_{\max}$:

$$G_{\max}(\beta, \omega) = \max_x G(x) \tag{2.45}$$

The optimal energy amplification G_{opt} and optimal perturbation q'_{opt} are, the maximum obtainable amplification of $G_{\max}$ and the corresponding initial perturbation, respectively.

$$G_{\text{opt}} = \max_{(\beta,\omega)} G_{\max} \tag{2.46}$$

Choice of energy norm

The non-modal analysis requires an energy norm to be defined. Written in the general form

$$E = \int_V \left(m_u \left(u^* u' + v^* v' + w^* w' \right) + m_\rho \rho^* \rho' + m_e e^* e' \right) dV \tag{2.47}$$

While in incompressible boundary layers the kinetic energy of a perturbation is a logical and physically meaningful choice for an energy norm, in compressible flows there is no such natural choice. Commonly Chu's energy norm (or Mack's in the ideal gas case), which eliminates compression work is chosen. Looking only at the pressure related terms of E:

$$\int_V \left(m_\rho \bar{\rho} \rho' \left(\nabla \cdot u' \right) + m_u \frac{1}{\mathrm{M}_\infty^2} \frac{1}{\bar{\rho}} u' \cdot \nabla p' + m_e \frac{\mathrm{Ec}_\infty}{\mathrm{M}_\infty^2} \frac{\bar{p}}{\bar{\rho}} e' \left(\nabla \cdot u' \right) \right) dV = 0 \tag{2.48}$$

from which

$$m_\rho = -\frac{1}{\mathrm{M}_\infty^2} \frac{1}{\bar{\rho}} \left(\frac{\partial e}{\partial \rho} \right)_{\bar{p}} \left(\frac{\partial e}{\partial p} \right)_{\bar{\rho}}^{-1} \qquad m_u = \bar{\rho} \qquad m_e = \frac{1}{\mathrm{Ec}_\infty} \frac{\bar{\rho}}{\bar{p}} \left(\frac{\partial e}{\partial p} \right)_{\bar{\rho}}^{-1} \tag{2.49}$$

However, at zero Mach number this norm is not physical. The weights m_ρ, m_e scale with M_∞^{-1}, such that in the limit $\mathrm{M}_\infty^2 \to 0$, m_ρ, $m_e \to \infty$, and the energy growth of a perturbation is not finite. For this reason two energy norms are adopted. Firstly the kinetic energy growth of a perturbation is considered:

$$KE = \int_V \rho \left(u^* u' + v^* v' + w^* w' \right) dV \tag{2.50}$$

which will be referred to as KE norm. Secondly, as to include all the terms of the perturbation vector q', the GE norm

$$GE = \int_V \rho \left(u^* u' + v^* v' + w^* w' + \rho^* \rho' + e^* e' \right) dV \tag{2.51}$$

is also considered.

3

Numerical Methods and Validation

3.1. Numerical methods

The present section addresses the numerical methods employed to solve the base flow in Section 2.2, and the viscous and inviscid eigenvalue problems in Section 2.3. A computational grid is constructed with N Gauss-Lobatto points

$$\hat{y}_j = \cos\left\{\frac{j\pi}{N}\right\}, \quad j = 1, 2 \ldots, N \tag{3.1}$$

The mapping between the physical domain, given by y, and the Gauss-Lobatto points $\hat{y}$ is

$$y_j = a\frac{1+\hat{y}}{b-\hat{y}}, \quad a = \frac{y_i y_{\max}}{y_{\max} - 2y_i}, \quad b = 1 + \frac{2a}{y_{\max}}, \tag{3.2}$$

where $y_{\max}$ is the height of the domain. The grid clustering parameter y_i causes the grid points to cluster near the wall, ensuring a more accurate resolution of the boundary-layer. The grid points y are mapped into the interval $[0, y_{\max}]$, with half being mapped onto $[0, y_i]$.

Numerical derivatives are calculated using Chebyshev polynomials. The derivative with respect to $\hat{y}$ is calculated as

$$\frac{\partial}{\partial \hat{y}} = \mathbf{D}_C \tag{3.3}$$

where $\mathbf{D}_C$ is an $N \times N$ Chebyshev differentiation matrix, and can be found in Trefethen (2000). In the physical domain, the first order derivative is

$$\frac{\partial}{\partial y} = \frac{\partial \hat{y}}{\partial y}\frac{\partial}{\partial \hat{y}} = \mathbf{D}_M \mathbf{D}_C \tag{3.4}$$

and for the second order derivative is

$$\frac{\partial^2}{\partial y^2} = \frac{\partial^2 \hat{y}}{\partial y^2}\frac{\partial}{\partial \hat{y}} + \left(\frac{\partial \hat{y}}{\partial y}\right)^2 \frac{\partial^2}{\partial \hat{y}^2} = \mathbf{D}_{M2}\mathbf{D}_C + \mathbf{D}_M^2 \mathbf{D}_C^2 \tag{3.5}$$

where $\mathbf{D}_M$ and $\mathbf{D}_{M2}$ are diagonal matrices, given by

$$\mathbf{D}_{M_{jj}} = \frac{\partial \hat{y}_j}{\partial y} = \frac{a(1+b)}{(a+y_j)^2} \tag{3.6a}$$

$$\mathbf{D}_{M2_{jj}} = \frac{\partial^2 \hat{y}_j}{\partial y^2} = \frac{-2a(1+b)}{(a+y_j)^3} \tag{3.6b}$$

3.1.1. Self-similar base-flow solution

Regarding base flow, Equation 2.9 is first decomposed into a set of first order ODEs of the form

$$\frac{\partial Y}{\partial \eta} = \mathcal{F}(\eta, Y) \tag{3.7}$$

With

$$Y = \begin{pmatrix} f \\ f' \\ f'' \\ g \\ g' \end{pmatrix} \qquad F(\eta, Y) = \begin{pmatrix} Y_2 \\ \frac{1}{C} Y_3 \\ -\frac{1}{C} Y_1 Y_3 \\ \frac{\mathrm{Pr}}{C} Y_5 \\ -\frac{\mathrm{Pr}}{C} Y_1 Y_5 - \frac{h^*_\infty}{C u^2_\infty} Y_3^2 \end{pmatrix} \tag{3.8}$$

The integration of Equation 3.7 is carried out using a fourth-order Runge-Kutta (RK4) method

$$Y^{j+1} = Y^j + \frac{\Delta\eta}{6}\left(k_1 + 2k_2 + 2k_3 + k_4\right), \; j = 1, \ldots, N-1 \tag{3.9}$$

where the superscript 'j' indicates the grid point, and where

$$\begin{aligned} k_1 &= \mathcal{F}(\eta^n, Y^n) \\ k_2 &= \mathcal{F}\left(\eta^n + \frac{\Delta\eta}{2}, Y^n + \frac{\Delta\eta}{2} k_1\right) \\ k_3 &= \mathcal{F}\left(\eta^n + \frac{\Delta\eta}{2}, Y^n + \frac{\Delta\eta}{2} k_2\right) \\ k_4 &= \mathcal{F}\left(\eta^n + \Delta\eta, Y^n + \Delta\eta k_3\right) \end{aligned} \tag{3.10}$$

At the wall, given the boundary conditions in equations 2.11 and 2.12 or 2.13

$$\begin{aligned} Y^{n=1} &= \left[0, \;\; 0, \;\; Y_3^{n=1}, \;\; Y_4^{n=1}, \;\; 0\right]^T \;\; \text{if} \;\; \frac{\partial g(0)}{\partial \eta} = 0 \\ Y^{n=1} &= \left[0, \;\; 0, \;\; Y_3^{n=1}, \;\; g_w, \;\; Y_5^{n=1}\right]^T \;\; \text{if} \;\; g(0) = g_w \end{aligned} \tag{3.11}$$

The Newton-Raphson's method is used to iteratively solve for the missing boundary conditions.

Convergence is achieved when the residual error ($0.5 \cdot ||r_i||_2$) is less than 1e−14. Regarding the computational mesh, convergence is found at $N = 10000$, $y_i = 10$, and $y_{\max} = 60$.

3.1.2. Eigenvalue problem solver

Discretization of equations 2.23 or 2.33, considering equations 3.4 and 3.5, result in the eigenvalue problem

$$\left(\alpha^2 \mathbf{A}_{\alpha^2} + \omega^2 \mathbf{A}_{\omega^2} + \alpha\omega \mathbf{A}_{(\alpha\omega)} + \alpha \mathbf{A}_\alpha + \omega \mathbf{A}_\omega + \mathbf{A}_0\right) \tilde{\mathbf{q}} = 0 \tag{3.12}$$

where the $\mathbf{A}$ matrices are $5N \times 5N$ in the viscous problem and $2N \times 2N$ in the inviscid problem.

Depending on the considered regime (viscous or inviscid), and on the considered framework

(temporal or spatial) the resulting eigenvalue problem may be quadratic:

$$\left(\sigma^2 \mathbf{A}_{\sigma^2} + \sigma \mathbf{A}_{\sigma} + \mathbf{A}_0\right) \tilde{\mathbf{q}} = 0 \tag{3.13}$$

where σ represents the eigenvalue α in the spatial framework and ω in the temporal. In order to solve the full quadratic EVP, the transformation

$$\begin{bmatrix} \mathbf{A}_0 & 0 \\ 0 & I \end{bmatrix} \begin{bmatrix} \tilde{\mathbf{q}} \\ \sigma\tilde{\mathbf{q}} \end{bmatrix} = \sigma \begin{bmatrix} -\mathbf{A}_{\sigma} & -\mathbf{A}_{\sigma^2} \\ I & 0 \end{bmatrix} \begin{bmatrix} \tilde{\mathbf{q}} \\ \sigma\tilde{\mathbf{q}} \end{bmatrix} \tag{3.14}$$

is applied, where I is the identity matrix. The problem in Equation 3.14 is linear in σ. The eigenvalue problem is solved using the QZ algorithm.

3.2. Validation and Convergence studies

In regard to the self-similar boundary layer solver described in Section 3.1.1, obtained results are compared to those of Ren et al. (2019b) in Figure 3.1. The obtained results are in agreement to those of Ren et al. (2019b).

Regarding the eigenvalue solver described in Section 3.1.2, Figure 3.2 shows contour levels of 2D instabilities ($\beta = 0$), in the $\mathrm{Re}_\delta - \mathrm{F}$ space for mode I and mode II. An Eckert number of 0.2 is considered. For comparison, the neutral curve from Ren et al. (2019b) is shown with markers, and a good agreement is found with the present results. The eigenfunctions for both modes are shown in Figure 3.3, where $F = 75\dot{1}0^{-6}$ is considered, where again the obtained results are in close agreement to those of Ren et al.

To validate the non-modal approach in Section 2.3.2, the results of Tumin and Reshotko (2001) are reproduced. An ideal-gas boundary layer is considered over a range of Mach numbers. Note that, since the fluid is considered calorically perfect, the boundary layer solver used in this case is slightly different, since the fluid thermodynamic properties are obtained from the ideal gas equation of state. However, the code employed to solve the EVP and obtain the non-modal results is identical, regardless of the considered equation of state. Figure 3.4 shows the comparison with the work of Tumin and Reshotko (2001). The results obtained with the present approach are in good agreement with those of Tumin and Reshotko.

As a second validation case for the non-modal analysis, the results of Bitter and Shepherd (2014) are replicated. In this case, air is considered as a thermally perfect gas. Therefore, neither the Prandtl number nor the specific heat is assumed constant. The specific heats vary with temperature only. The dynamic viscosity follows Sutherland's formula and the thermal conductivity is modelled with Euken's method. A supersonic boundary layer at $\mathrm{M}_\infty = 5$ is considered, the wall is adiabatic and the free-stream temperature is $T^*_\infty = 70\mathrm{K}$. In this case the temporal framework is considered, meaning ω is complex, and the perturbation grows with time. Figure 3.5 shows the global eigenvalue spectrum. The 10 modes that contribute most significantly to the optimal disturbance are marked. The blue crosses represent the results obtained with the present code, and in red circles the results of Bitter and Shepherd (2014). Regarding the discrete modes, the obtained eigenvalues are nearly identical, whilst for the continuous spectra, the marked eigenvalues are located in close proximity along the same continuous branch.

The calculation of the eigenvalue problem is performed with $N = 301$ grid points, a domain height of $y_{\max} = 200$, considering $y_i = 5$ (see Equation 3.2). To verify that results for the EVP have converged, point wise checks were performed with varying number of grid points and domain heights. An example is show in Table 3.1, where the dependency of the complex wave number α for mode I and mode II is shown with respect to the number of grid points. Additionally, in Table 3.2, the dependency of

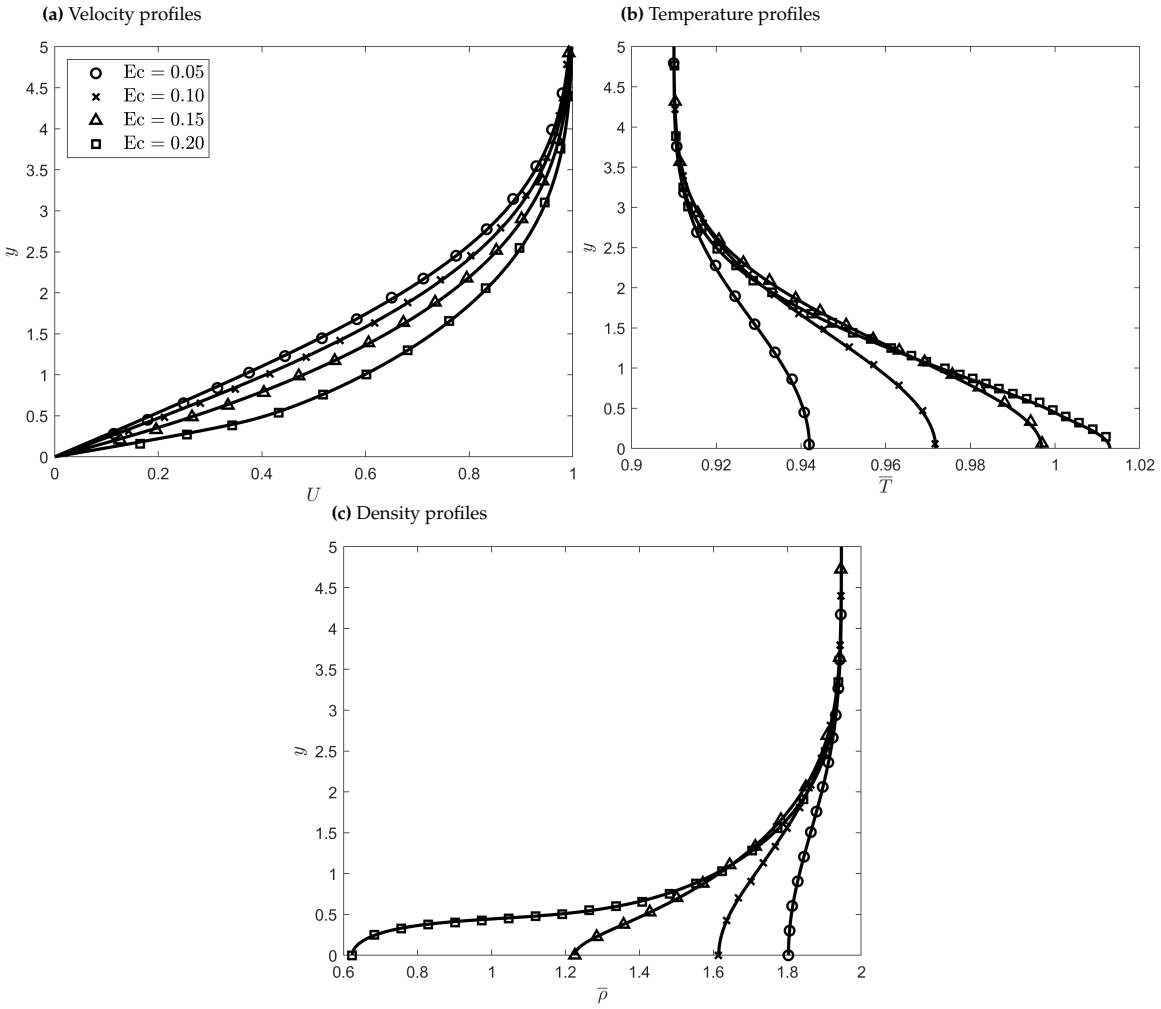

Figure 3.1: Base-flow profiles for SCO2 boundary layers with varying Eckert number, P^*_∞ = 80bar, T^*_∞ = 280K, and adiabatic wall. Temperature (panel 3.1b) and density (panel 3.1c) are non-dimensionalized by the pseudo-critical values: $\overline{T} = \overline{T}^*/T^*_{pc}$, and $\overline{\rho} = \overline{\rho}^*/\rho^*_{pc}$. The velocity (panel 3.1a) is non-dimensionalized by the free-stream velocity: $U = U^*/U^*_\infty$. The lines correspond to the results obtained with the present methodology, and the markers show the results from Ren et al. (2019b)

G_{max} is shown with regard to the number of grid points. When considering $y_i = 5$, for a number of grid points higher than 301 ($N > 301$) both the calculated modal amplification ($-\alpha_i$) and real wave number (α_r) vary less than 1%, confirming that convergence is achieved. As for the non-modal results, results are also shown to be converged for $N = 301$, with a maximum error of less than 0.5%. The grid clustering parameter y_i used in the present study is half of that suggested by M. R. Malik (1990) for hypersonic boundary layers. While for hypersonic boundary layers the boundary layer thickness is large, the considered SCO2 boundary layers are more confined, and a lower value for y_i result in the proper resolution of the boundary layer for smaller N. Indeed, a faster convergence is obtained with $y_i = 5$ when compared to $y_i = 10$, as is shown Table 3.1.

The full spatial formulation is used for the modal results, that is the term $\alpha^2\mathbf{A}_{\alpha^2}$ in Equation 3.12 is not neglected, and the eigenvalue problem is solved via the transformation in Equation 3.14. The full spatial formulation results in a minor time penalty, since only the eigenvalue pertaining to mode I or mode II needs to be calculated, as opposed to calculating the global eigenvalue spectrum. However, in the case of the non-modal analysis, Equation 3.12 is linearized and the term $\alpha^2\mathbf{A}_{\alpha^2}$ is neglected. As the non-modal calculation requires the calculation of the global eigenvalue spectrum (that is, a

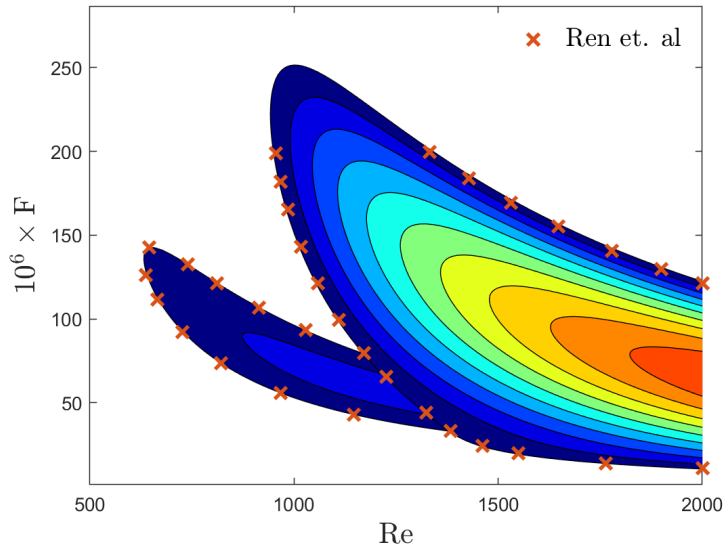

Figure 3.2: Growth rates ($-\alpha_i$) of mode I and mode II in the $\mathrm{Re}_\delta - \mathrm{F}$ space, when considering $\beta = 0$. SCO2 real gas boundary layers with $\mathrm{Ec}_\infty = 0.2$, $P^*_\infty = 80$bar, $T^*_\infty = 280$K, and adiabatic wall. The colored contours represent the growth rate of mode I and mode II. The red crosses represent the neutral curve as obtained by Ren et al. (2019b).

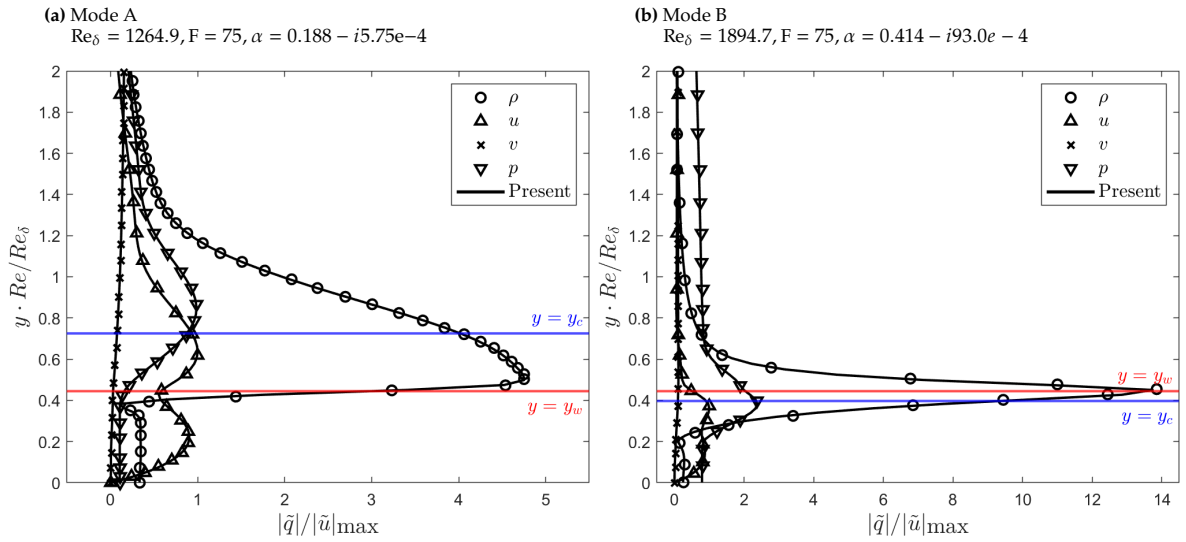

Figure 3.3: Profiles of mode I (3.3a) and mode II (3.3b) perturbations. CO2 boundary layer with $T^*_\infty = 280$K, $P^*_\infty = 80$bar, and adiabatic wall. The Eckert number is 0.2, the wave number in the z-direction is $\beta = 0$, and the global frequency is $\mathrm{F} = 75 \times 10^{-6}$. For mode A (3.3a) $\mathrm{Re}_\delta = 1264.9$, and for mode B (3.3b) $\mathrm{Re}_\delta = 1894.7$.

Convergence of mode I and mode II for varying number of grid points (N) with $y_i = 10$, and $y_i = 5$				
	Mode I		Mode II	
N	$y_i = 5$	$y_i = 10$	$y_i = 5$	$y_i = 10$
101	85.679 - 2.388i	81.719 + 0.408i	125.16 - 9.86i	121.65 - 13.32i
201	85.891 - 2.042i	86.108 - 2.455i	129.07 - 5.90i	128.17 - 6.74i
301	85.888 - 2.056i	85.908 - 2.075i	128.85 - 6.02i	128.17 - 6.74i
401	85.888 - 2.056i	85.885 - 2.053i	128.86 - 6.02i	128.86 - 6.01i
501	85.888 - 2.056i	85.888 - 2.056i	128.86 - 6.02i	128.86 - 6.02i

Table 3.1: Convergence obtained for increasing number of grid points (N) for mode A and mode B, considering $y_i = 10$ and $y_i = 5$. CO2 boundary layer at $\mathrm{M}_\infty = 0.3$, $T_\infty = 0.95 T_{pc}$, $T_{wall} = 1.05 T_{pc}$, $P^*_\infty = 80$bar, when considering $\mathrm{Re}_\delta = 1000$, $\beta = 0.2$, $\omega = 0.05$.

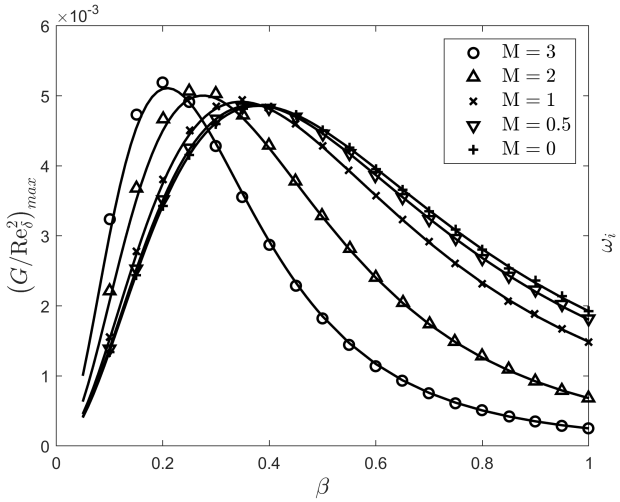

Figure 3.4: Maximum spatial energy amplification of stationary waves ($\omega = 0$) with varying span-wise wave number (β). Ideal gas boundary layer with stagnation a temperature of 333K and adiabatic wall. The specific heat ratio is 1.4, the dynamic viscosity follows Sutherland's formula, and the Prandtl number is assumed constant $\mathrm{Pr}_\infty = 0.7$. The markers represent the results obtained by Tumin and Reshotko (2001), and the line the results obtained with the present approach.

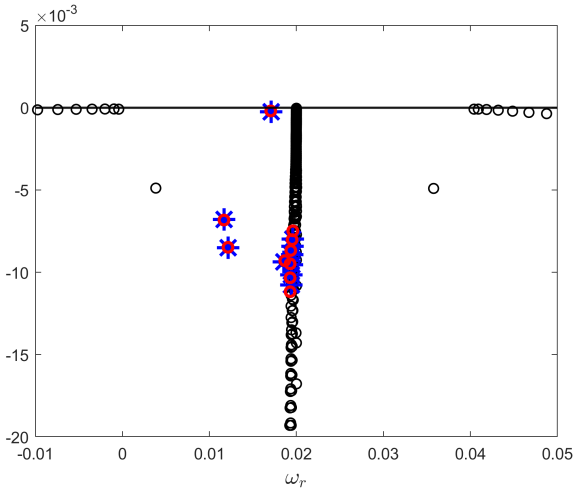

Figure 3.5: Global eigen spectrum. Air boundary layer, modelled as a thermally perfect gas. M = 5, $T_\infty = 70$K, $T_{wall} = T_{\mathrm{adiabatic}}$. $\alpha = 0.02$, $\beta = 0.1$, and $\mathrm{Re}_\delta = 300$. The markers show the 10 most relevant modes for the optimal disturbance. The blue crosses the results obtained with the present methodology, and the red circles are the results of Bitter and Shepherd (2014).

Convergence of $G_{\max}$ for increasing number of grid points (N) $\mathrm{Re}_\delta = 1000$, $\beta = 1$					
N		201	301	401	501
$G_{\max}$	$\omega = 0$	6534	6773	6768	6752
	$\omega = 0.1$	4888	5002	4998	4990

Table 3.2: Convergence obtained for $G_{\max}$ with increasing number of grid points (N), considering $y_i = 5$ and $y_{\max} = 200$. CO2 boundary layer with M = 0.3, $T_\infty = 0.95T_{pc}$, $T_{\mathrm{wall}} = 1.05T_{pc}$, $P_\infty = 80$bar, $\mathrm{Re}_\delta = 1000$, $\beta = 1$

discrete approximation to the entire eigenvalue spectrum), a sizeable time efficiency is gained with this approach. To verify that the linearization is appropriate, at times, the quadratic problem is resolved, following the method in Equation 3.14. Figure 3.6 compares the maximum energy growth obtained when solving the full quadratic EVP to those obtained through linearization. The GE energy norm is considered (Equation 2.51). The considered boundary layer is a heated wall transcritical flow with $T_{\mathrm{wall}} = 0.95T_{pc}$, $T_\infty = 1.05T_{pc}$, and $\mathrm{M}_\infty = 0.3$. The Reynolds number is $\mathrm{Re}_\delta = 1000$, the span-wise wave number is $\beta = 1$, with varying frequency ω. For this particular scenario a difference of less than 0.1% is observed, confirming the validity of the results obtained through linearization of Equation 3.13.

The limiting case of $\mathrm{M}_\infty \to 0$ is studied, for which a "very small" Mach is considered. To test the validity of this approach, the modal stability of a heated wall transcritical flow with increasingly smaller Mach number is investigated. Figure 3.7 shows the convergence obtained for the eigenvalues for mode I and II, and Figure 3.8 shows the convergence obtained for the maximum energy growth $G_{\max}$ For a Mach number of order 10^{-3} results are found to be converged. A Mach 10^{-3} boundary layer is considered for the zero Mach boundary layer results.

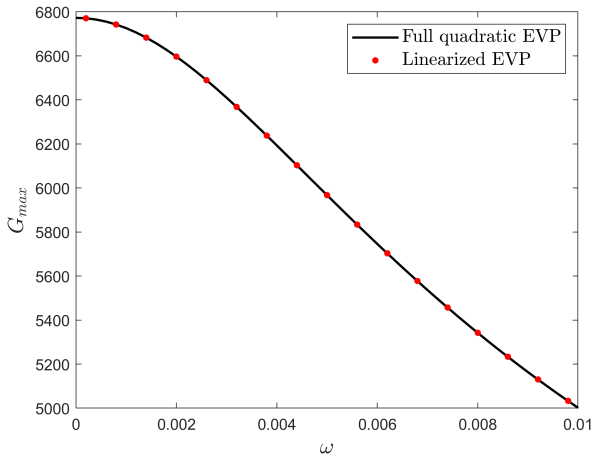

Figure 3.6: Comparison between non-modal results obtained by solving the full quadratic EVP in Equation 3.12 and by linearizing the EVP. The Reynolds number is $\mathrm{Re}_\delta = 1000$, the span-wise wave number is $\beta = 1$. CO2 boundary layer with $T_\infty = 0.95T_{pc}$, $T_{\mathrm{wall}} = 1.05T_{pc}$, $P_\infty = 80$bar and $\mathrm{M}_\infty = 0.3$

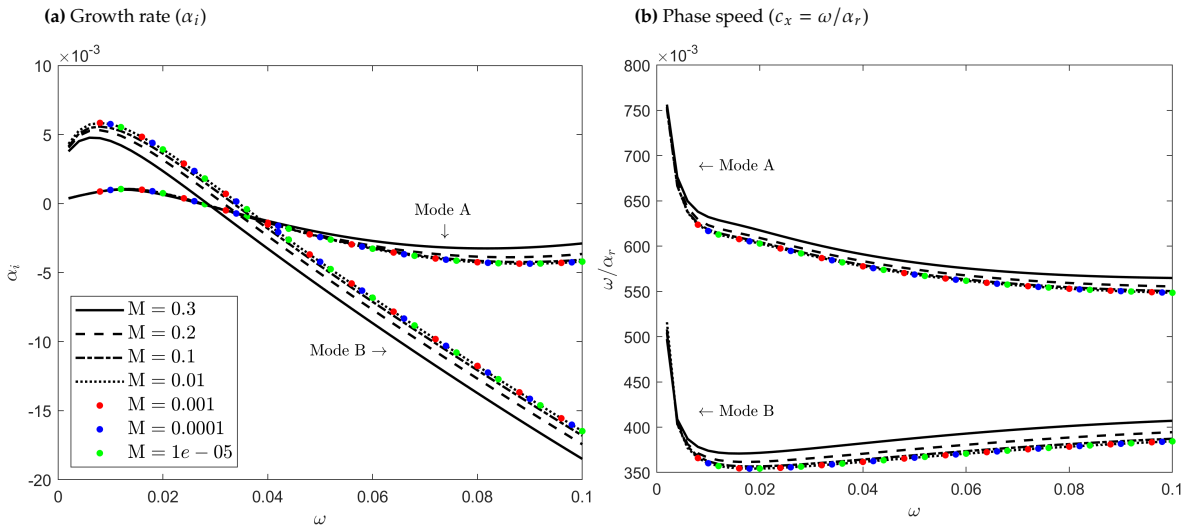

Figure 3.7: Influence of increasingly smaller Mach number on modal stability. The growth rate in 3.7a and the phase speed $c_x = \omega/\alpha_r$ in 3.7b for both mode I and mode II. Various Mach numbers for a CO2 boundary layer with $T_\infty = 0.95T_{pc}$, $T_{wall} = 1.05T_{pc}$, $P_\infty = 80$bar, $\mathrm{Re}_\delta = 1000$, $\beta = 0.2$, and varying ω

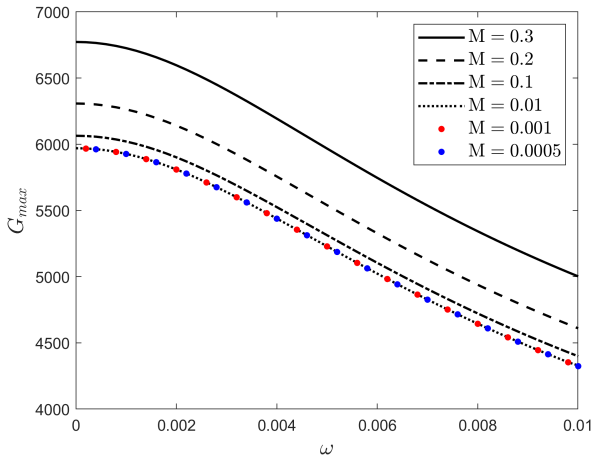

Figure 3.8: Influence of Mach number on the maximum perturbation energy growth. The maximum energy growth (G_{max}) is plotted with respect to the frequency ω. The Reynolds number is $\mathrm{Re}_\delta = 1000$, and the span-wise wave number $\beta = 1$. Various Mach numbers for a CO2 BL with $T_\infty = 0.95T_{pc}$, $T_{\mathrm{wall}} = 1.05T_{pc}$, $P_\infty = 80$bar.

4

Selected Base Flows

In this chapter, the base flow profiles under consideration are presented. We consider CO2 boundary layers at a supercritical pressure of 80bar. The wall is isothermal, and the boundary layers are divided into three regimes: subcritical, transcritical, and supercritical. In the subcritical regimes, the temperature profiles remain below the pseudo-boiling temperature of $T_{pc} = 307.7$K, while in the supercritical regime, the temperature profiles exceed this value. In the transcritical regime the temperature profile crosses the pseudo-boiling temperature. For each flow regime, both wall cooling and wall heating are considered.

In the subcritical regime, the free-stream and wall temperatures are set at either $0.90 \cdot T_{pc}$ or $0.95 \cdot T_{pc}$, depending on whether wall cooling or heating is considered. Similarly, for the supercritical regime, the temperature boundary conditions are $1.05 \cdot T_{pc}$ and $1.10 \cdot T_{pc}$. Finally, in the transcritical regimes, the temperature boundary conditions are $0.95 \cdot T_{pc}$ and $1.05 \cdot T_{pc}$. The Mach number is varied, and, given the scaling in equation 2.1, the Mach number is varied in increments of its square, i.e., we consider increments of M_∞^2. The considered Mach numbers are $M_\infty^2 = \{0, 0.2, 0.4, 0.6, 0.8, 0.9\}$, where $M_\infty^2 = 0.9$ is chosen instead of $M_\infty^2 = 1$ as to avoid the sonic condition at the free-stream. For the heated subcritical case, the maximum considered Mach number is $M_\infty^2 = 0.6$ as opposed to $M_\infty^2 = 0.9$. This is due to the proximity of the temperature profile to the pseudo-boiling point for the $M_\infty^2 > 0.6$ cases. For the high Mach number subcritical boundary layers, it was found the the modal response deviated substantially from the low Mach number cases, and was in some regards qualitatively similar to a trancritical boundary layer; for this reason $M_\infty^2 > 0.6$ is not considered. An overview of the different cases is given in Table 4.1.

The base flow temperature, density and velocity profiles are shown in Figure 4.1 for the heated wall cases, and in Figure 4.2 for the cooled wall cases. In the supercritical regime (for both heated and cooled wall), an increase in Mach number results in a comparatively small change in the temperature and density profiles. Viscous heating in the supercritical regime is reduced when compared to the subcritical conditions ,which aligns with the Eckert numbers shown in Table 4.1. Furthermore, the velocity profile in the supercritical regime is almost unvarying with the Mach number and very similar to the Blasius profile.

The transcritical cases feature strong density gradients, specially in the vicinity of the Widom point. In the heated wall cases, an increase in the Mach number results in a noticeable increase in the height of the Widom point. However, for the cooled wall cases, the height at which the pseudo-boiling is crossed remains almost unchanged with varying Mach number. Regarding the velocity profiles, similar to the two-fluid boundary layer in Özgen et al., 1998, below the pseudo-boiling point the velocity profile is near linear. In the heated wall transcritical cases, the near wall velocity gradient is large, with the dynamic viscosity being low in this region. Conversly, for the cooled wall transcritical cases, the

		Subcritical Regime						
		T^*_∞/T^*_{pc}	$T^*_{\text{wall}}/T^*_{pc}$	Pr_∞	M^2_∞	M_∞	Ec_∞	Case
CO2 at P^* = 80bar	Heated Wall	0.90	0.95	2.11	$1 \cdot 10^{-4}$	0.01	0.000	SubHM0
					0.2	0.447	0.106	SubHM^{2}0.2
					0.4	0.632	0.211	SubHM^{2}0.4
					0.6	0.775	0.317	SubHM^{2}0.6
	Cooled Wall	0.95	0.90	2.39	$1 \cdot 10^{-4}$	0.01	0.000	SubCM0
					0.2	0.447	0.045	SubCM^{2}0.2
					0.4	0.632	0.090	SubCM^{2}0.4
					0.6	0.775	0.135	SubCM^{2}0.6
					0.8	0.894	0.180	SubCM^{2}0.8
					0.9	0.949	0.202	SubCM^{2}0.9
		Supercritical Regime						
		T^*_∞/T^*_{pc}	$T^*_{\text{wall}}/T^*_{pc}$	Pr_∞	M^2_∞	M_∞	Ec_∞	Case
CO2 at P^* = 80bar	Heated Wall	1.05	1.10	1.59	$1 \cdot 10^{-4}$	0.01	0.000	SupHM0
					0.2	0.447	0.012	SupHM^{2}0.2
					0.4	0.632	0.025	SupHM^{2}0.4
					0.6	0.775	0.037	SupHM^{2}0.6
					0.8	0.894	0.050	SupHM^{2}0.8
					0.9	0.949	0.056	SupHM^{2}0.9
	Cooled Wall	1.10	1.05	1.22	$1 \cdot 10^{-4}$	0.01	0.000	SupCM0
					0.2	0.447	0.020	SupCM^{2}0.2
					0.4	0.632	0.040	SupCM^{2}0.4
					0.6	0.775	0.059	SupCM^{2}0.6
					0.8	0.894	0.079	SupCM^{2}0.8
					0.9	0.949	0.089	SupCM^{2}0.9
		Transcritical Regime						
		T^*_∞/T^*_{pc}	$T^*_{\text{wall}}/T^*_{pc}$	Pr_∞	M^2_∞	M_∞	Ec_∞	Case
CO2 at P^* = 80bar	Heated Wall	0.95	1.05	2.39	$1 \cdot 10^{-4}$	0.01	0.000	TransHM0
					0.2	0.447	0.045	TransHM^{2}0.2
					0.4	0.632	0.090	TransHM^{2}0.4
					0.6	0.775	0.135	TransHM^{2}0.6
					0.8	0.894	0.180	TransHM^{2}0.8
					0.9	0.949	0.202	TransHM^{2}0.9
	Cooled Wall	1.05	0.95	1.59	$1 \cdot 10^{-4}$	0.01	0.000	TransCM0
					0.2	0.447	0.012	TransCM^{2}0.2
					0.4	0.632	0.025	TransCM^{2}0.4
					0.6	0.775	0.037	TransCM^{2}0.6
					0.8	0.894	0.050	TransCM^{2}0.8
					0.9	0.949	0.056	TransCM^{2}0.9

Table 4.1: Numerical parameters of the cases investigated. CO2 boundary layer at supercritical pressure of p = 80bar. The free-stream and wall temperature are shown non-dimensionalized by the pseudo-critical temperature of T^*_{pc} = 307.7K. The wall is isothermal. Varying Mach numbers at the free-stream, which is prescribed. The Eckert and Prandtl numbers at the free-stream result from the input parameters

dynamic viscosity is high near the wall, and the velocity gradient is low.

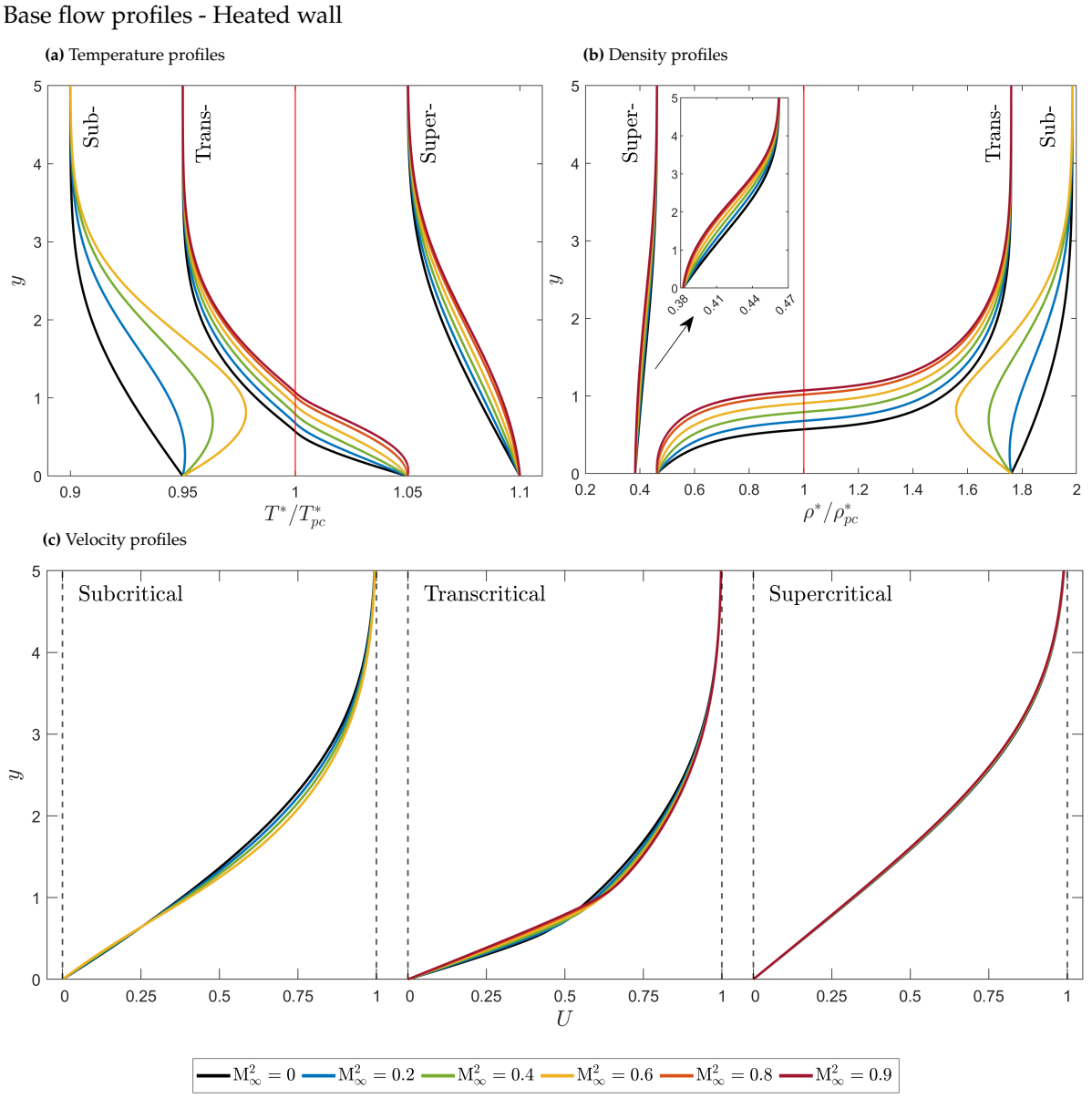

Figure 4.1: Base flow profiles of all considered cases with a heated wall. The vertical red line in the temperature and density panels (4.2a and 4.2b) represent the condition at the pseudo-critical point.

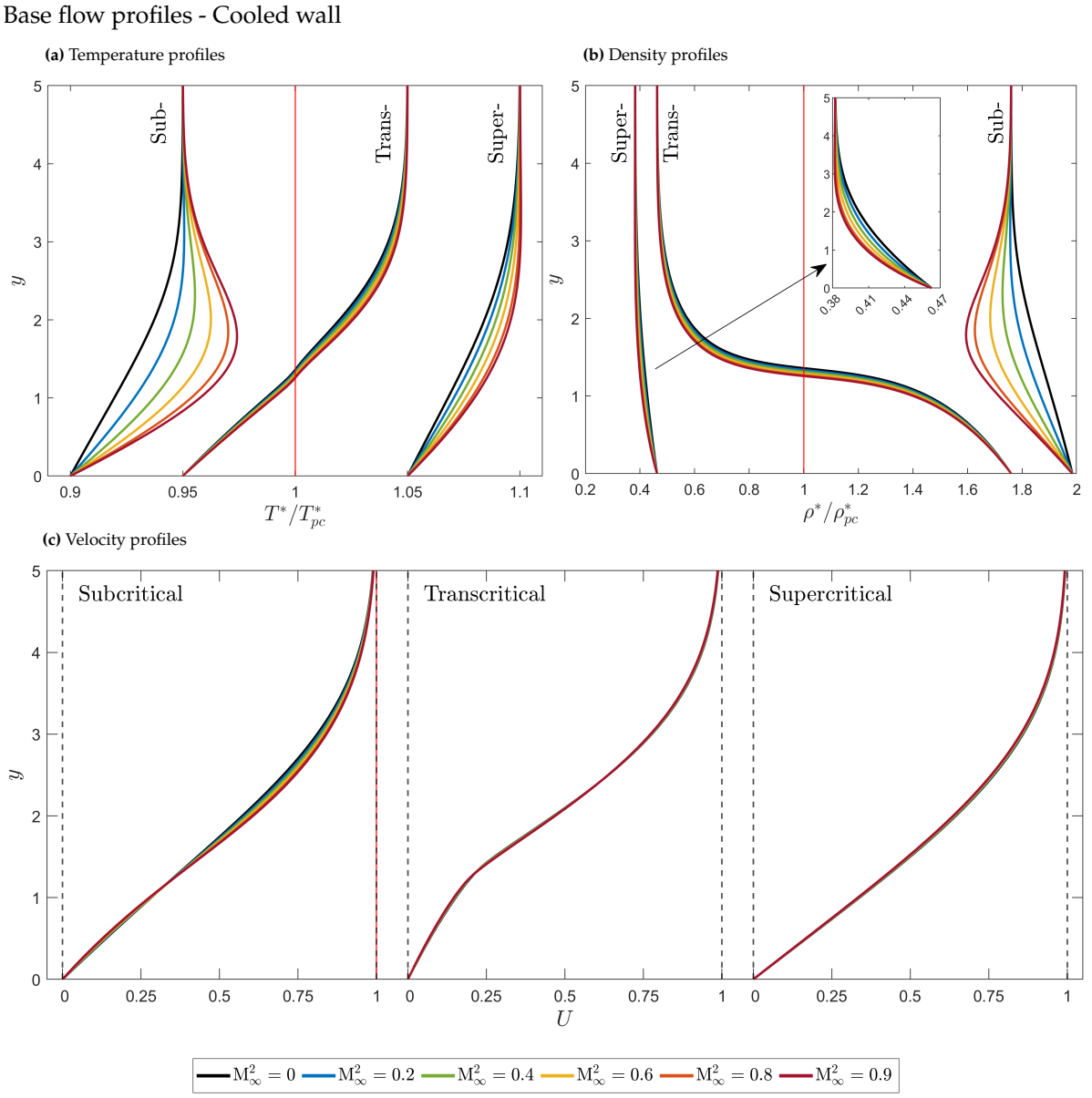

Figure 4.2: Base flow profiles of all considered cases with a cooled wall. The vertical red line in the temperature and density panels (4.2a and 4.2b) represent the condition at the pseudo-critical point.

5

Results: Modal Stability Analysis

In this chapter, the modal stability of mode I and mode II is investigated. Firstly, the viscous problem is considered, where the Reynolds number is finite. Section 5.1 explores mode I (TS mode) instability in the subcritical and supercritical boundary-layer flows. Section 5.2 investigates mode I (when present) and mode II in the transcritical flows. Particular attention is given to the amplification of 3D waves and the effect of the Mach number in the further amplification of 3D waves when compared to their 2D counterparts. Finally, in Section 5.3, the inviscid formulation is considered ($Re_\delta \to \infty$). In this case, only mode II is present for the transcritical regimes. In this simplified scenario, the effect of Mach number in the further amplification of 3D waves is analyzed once more.

5.1. Sub- and Supercritical Regimes

The subcritical and supercritical regimes are investigated – see Table 4.1. In these regimes, only the viscous mode I is present. The analysis begins by considering the case $M_\infty \to 0$, representing the limit of an infinitely high speed of sound and negligible compressibility effects. Figure 5.1 shows the growth rate of mode I in the $Re_\delta - \omega - B$ space for both heated and cooled wall scenarios in the sub- and supercritical regimes at zero Mach number. At $M_\infty = 0$, for all four boundary layers, as the global span-wise wave number (B) increases, the unstable surfaces become smaller, and the maximum growth rate decreases. Therefore, at $M_\infty = 0$, mode I is observed to be preferentially 2D. For increasing wave number B, mode I remains unstable only at lower Re_δ values. Still, the critical Reynolds number – defined as the minimum Reynolds number at which an unstable wave exists – increases slightly with B.

The supercritical heated wall (SupHM0) and the subcritical cooled wall (SubCM0) cases (panels 5.1b and 5.1c) are both qualitatively and quantitative similar. Similarly, the supercritical cooled wall (SupCM0) and the subcritical heated wall (SubHM0) scenarios exhibit comparable behavior. This indicates that at $M_\infty = 0$, a symmetry of the wall and free-stream temperatures, at the pseudo-critical point, produce a similar modal response. The maximum growth rate for the SupHM0 and SubCM0 cases is approximately twice as high as the SupCM0 and SupHM0 cases and occurs at a lower Reynolds number. This results in the boundary layer being unstable for higher values of the global span-wise wave number B.

To investigate the three-dimensionality of mode I under compressibility effects, non-zero Mach number is considered. The squared Mach number at the free stream is varied from $M_\infty^2 = 0$ to $M_\infty^2 = 0.9$. The growth rate ($-\alpha_i$), optimized over all values of Re_δ and ω, is computed for various β. Note that, unlike Figure 5.1, where the global span-wise wave number B is varied, in this case, the span-wise wave number β is considered.

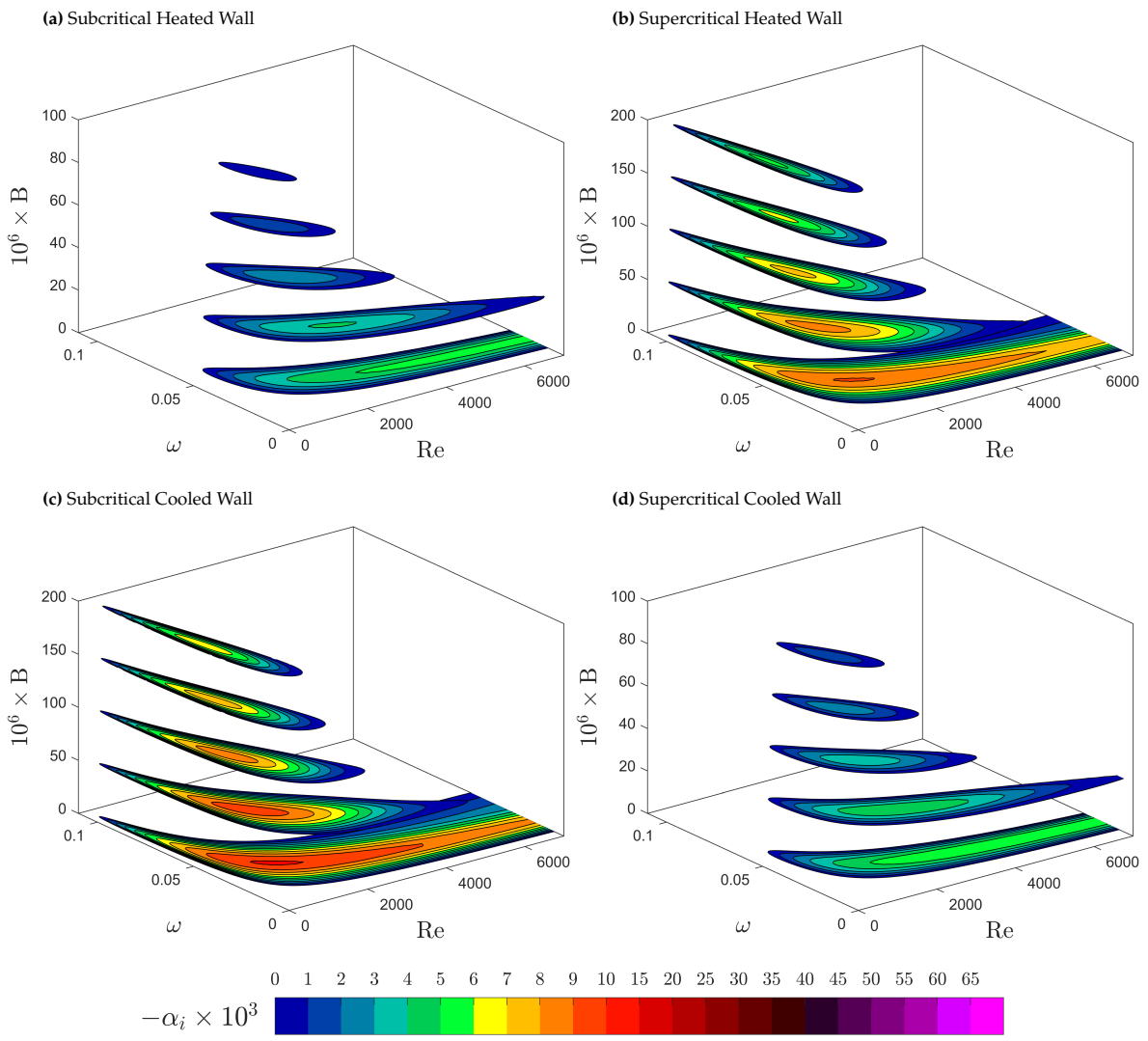

Figure 5.1: Growth rate contour in the $\mathrm{Re}_\delta - \omega - \mathrm{B}$ space for the Sub- and supercritical cases at zero Mach number (SubHM0 5.1a, SupHM0 5.1b, SubCM0 5.1c, SupCM0 5.1d)

To quantify the effect of β on the maximum modal amplification, the growth rate $-\alpha_i$ is normalized by the amplification of the most amplified 2D mode. Let r represent the ratio of the growth rate to that of the most amplified 2D instability, given by

$$r(\beta) = \frac{(\max_{\omega,\mathrm{Re}_\delta}\{-\alpha_i\})_\beta}{(\max_{\omega,\mathrm{Re}_\delta}\{-\alpha_i\})_{\beta=0}} \tag{5.1}$$

Table 5.1 shows the parameters of the most amplified 2D instability for all subcritical and supercritical cases. For the supercritical cases, an increase in the Mach number leads to a decrease in the most amplified modal amplification. This is accompanied by an increase in Re_δ number and a decrease in ω for the most amplified wave. Conversely, for the subcritical cases, an increase in Mach number leads a decrease in Re_δ and an increase in ω of the most amplified wave. In the subcritical heated wall case the growth rate of the most amplified 2D wave increases with the Mach number. However, in the cooled wall case, the modal amplification at high Mach number is lower compared to the lower M_∞^2 cases.

The growth rate ratio $r(\beta)$ is shown in Figure 5.2. In all cases, a sufficiently high Mach number will lead to waves that are preferentially 3D. In the supercritical cases a higher growth rate ratio (r) is

(a) Heated Wall Subcritical Cases

Case	Re_δ	ω	$\alpha \times 10^3$
SubHM0	7484	0.0183	85.2 - 5.45 i
SubHM^{2}0.2	4943	0.0218	90.8 - 6.45 i
SubHM^{2}0.4	3792	0.0237	91.4 - 7.12 i
SubHM^{2}0.6	2916	0.0251	89.7 - 7.53 i

(b) Heated Wall Supercritical Cases

Case	Re_δ	ω	$\alpha \times 10^3$
SupHM0	1653	0.0368	115.9 - 9.1 i
SupHM^{2}0.2	1734	0.0340	106.7 - 8.0 i
SupHM^{2}0.4	1807	0.0315	98.2 - 6.9 i
SupHM^{2}0.6	1861	0.0293	90.3 - 6.0 i
SupHM^{2}0.8	1888	0.0273	83.3 - 5.1 i
SupHM^{2}0.9	1886	0.0265	80.1 - 4.6 i

(c) Cooled Wall Subcritical Cases

Case	Re_δ	ω	$\alpha \times 10^3$
SupHM0	1409	0.0368	123.1 - 10.1 i
SupHM^{2}0.2	1345	0.0369	120.9 - 10.3 i
SupHM^{2}0.4	1268	0.0369	118.0 - 10.3 i
SupHM^{2}0.6	1158	0.0370	115.0 - 10.1 i
SupHM^{2}0.8	990	0.0380	113.1 - 9.6 i
SupHM^{2}0.9	876	0.0392	113.3 - 9.4 i

(d) Cooled Wall Supercritical Cases

Case	Re_δ	ω	$\alpha \times 10^3$
SupCM0	5831	0.0185	90.3 - 5.9 i
SupCM^{2}0.2	6601	0.0163	80.3 - 5.0 i
SupCM^{2}0.4	7457	0.0143	70.9 - 4.2 i
SupCM^{2}0.6	8283	0.0126	62.3 - 3.5 i
SupCM^{2}0.8	8864	0.0112	54.5 - 2.7 i
SupCM^{2}0.9	8924	0.0106	51.1 - 2.4 i

Table 5.1: Parameters for the most amplified 2D mode I instability for all the sub- and supercritical cases

achieved when compared to the subcritical regime. For the supercritical cases, with an increase in Mach number, the growth rate of the most amplified 2D perturbation decreases, and so does the range of β for which an instability exists. The opposite is observed in the subcritical regimes, where an increase in Mach number leads to an increase of the growth rate of the 2D instability and of the maximum wave number β for which an instability exists. The similarity between the SupH and SubC cases (panels 5.2b and 5.2c), and the SupC and SubH cases, is lost for finite Mach number. This is not surprising considering the loss of simetry in the base flow profiles shown in Figures 4.1 and 4.2.

Figure 5.3 shows, for varying β, the phase speed $c_x = \omega/\alpha_r$ for the most amplified modes. As shown in Section 2.3, the quantity $c_x = \omega/\alpha_r$ is the phase speed along the x-axis. For all cases where compressibility is negligible, including all zero Mach number cases, the phase speed of the most amplified wave increases with increasing β. However, in the cases where $r > 1$, indicating that mode I is preferentially 3D, a decrease in the phase speed c_x is observed before its subsequent increase. This reduction in phase speed is more pronounced at higher Mach numbers, where the growth rate ratio r is also higher. There appears to be a link between the decrease of phase speed c_x and the increase of the amplification $-\alpha_i$.

Figure 5.4 shows, for the highest considered Mach number in each panel of Figure 5.2, the most amplified 2D perturbation alongside the most amplified 3D perturbation. Let y_c denote the location at which the base flow velocity equals the phase speed c_x. This point, referred to as the critical layer, is marked by a horizontal blue line in each panel of Figure 5.4. It is observed that for oblique perturbations, the eigenfunctions are more confined in the boundary layer, meaning the eigenfunctions are "small" away from the wall. For the 3D perturbations, the perturbation velocity in the z-direction is sizable and its maximum amplitude close to y_c. Both temperature and pressure perturbations become comparatively smaller. Hence, the most unstable oblique perturbation has more of a kinetic nature when compared to its 2D counterpart. Additionally, it is noted that the Reynolds number of the most amplified perturbation increases with β, while the frequency ω decreases.

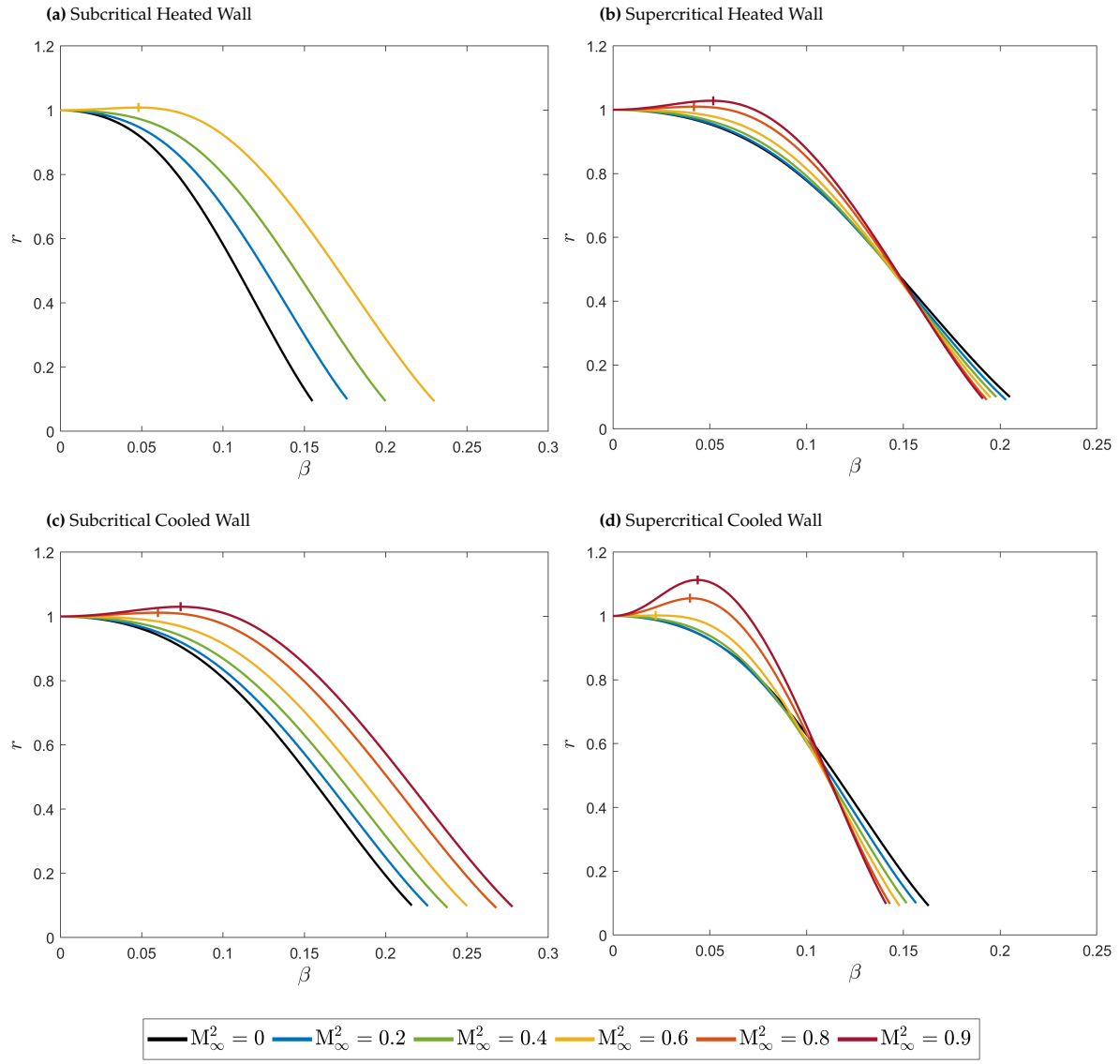

Figure 5.2: Evolution of the growth rate ratio r with the span-wise wave number for all sub- and supercritical cases. The maximum obtained growth rate ratio is represented by a vertical dash.

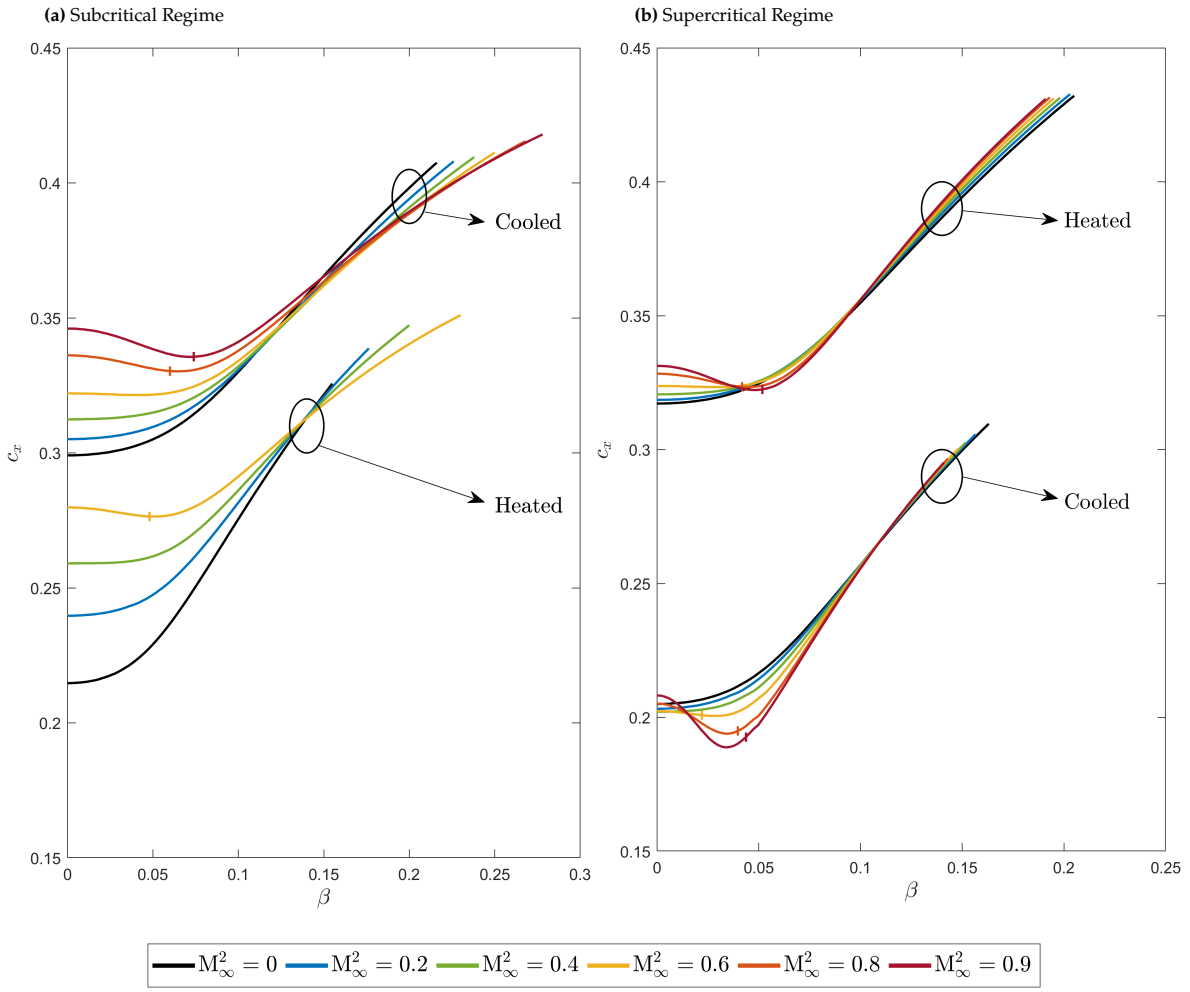

Figure 5.3: Effect of the span-wise wave number β on the phase velocity (c_x) of the most amplified mode. All sub- and supercritical cases. The point at which maximum growth rate ratio is achieved is marked with a dash.

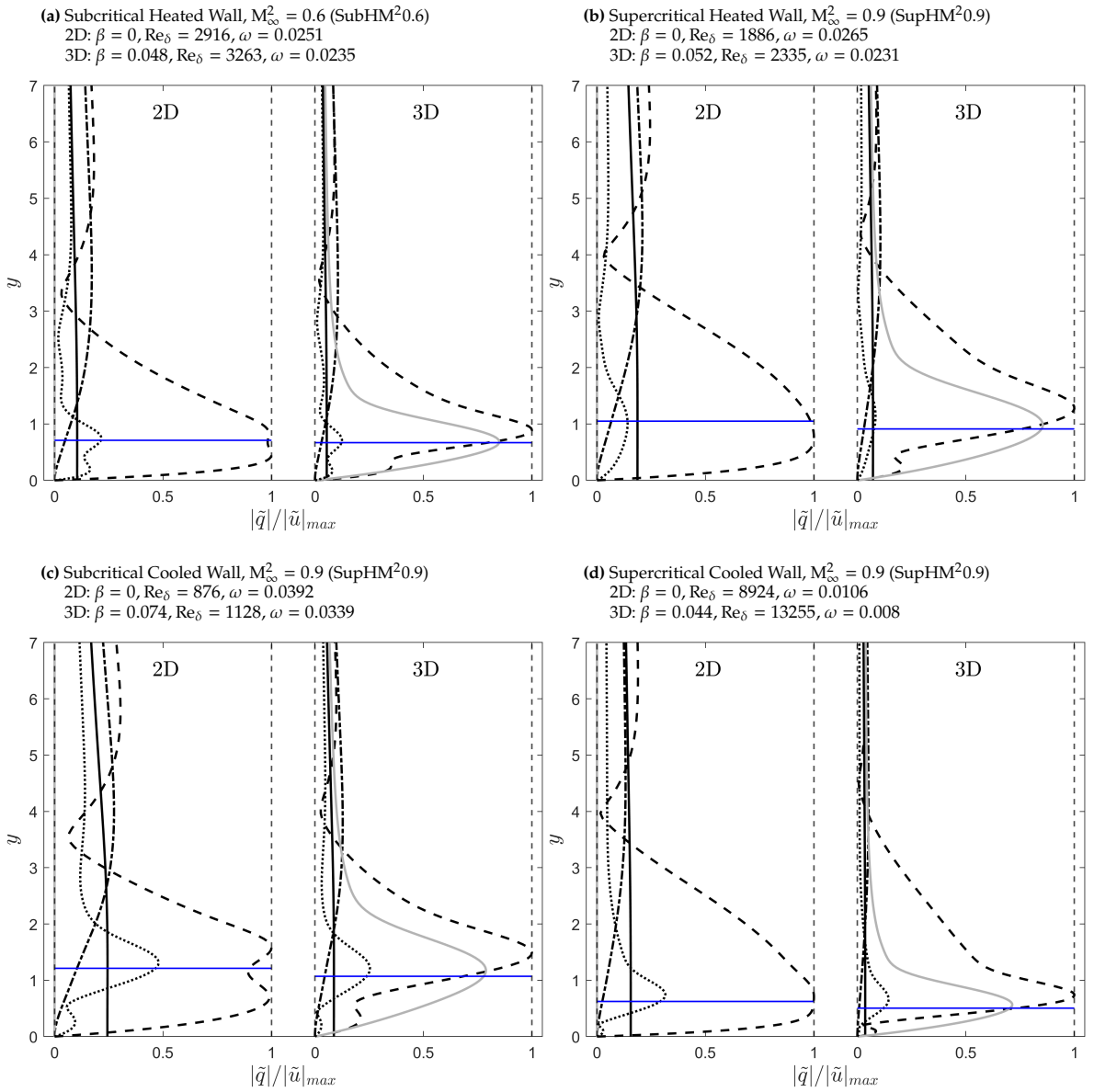

Figure 5.4: Profiles of the most amplified 2D and 3D perturbations. The horizontal blue line represents the location of y_c, defined has the point at which the base flow velocity U is the same as the phase speed c_x ($U(y_c) = c_x$). For each panel, the Mach number is the highest Mach in the respective panel in Figure 5.2: Case SubHM^{2}0.6 in 5.4a, case SupHM^{2}0.9 in 5.4b, case SubCM^{2}0.9 in 5.4c, and case SupCM^{2}0.9 in 5.4d.

5.2. Transcritical Regime

In this section, the stability of mode I and mode II in the transcritical regime is investigated. While mode I and mode II may coexist in transcritical boundary layers, for the considered temperature boundary conditions, no mode I instability was found in the cooled wall scenario. As in Section 5.1, the analysis begins by considering the case where $M_\infty \to 0$. Figure 5.5 shows the growth rates of mode I (panel 5.5c) and mode II (panels 5.5b and 5.5b) in the $Re_\delta - \omega - B$ space for both heated and cooled wall scenarios in the transcritical regime at zero Mach number.

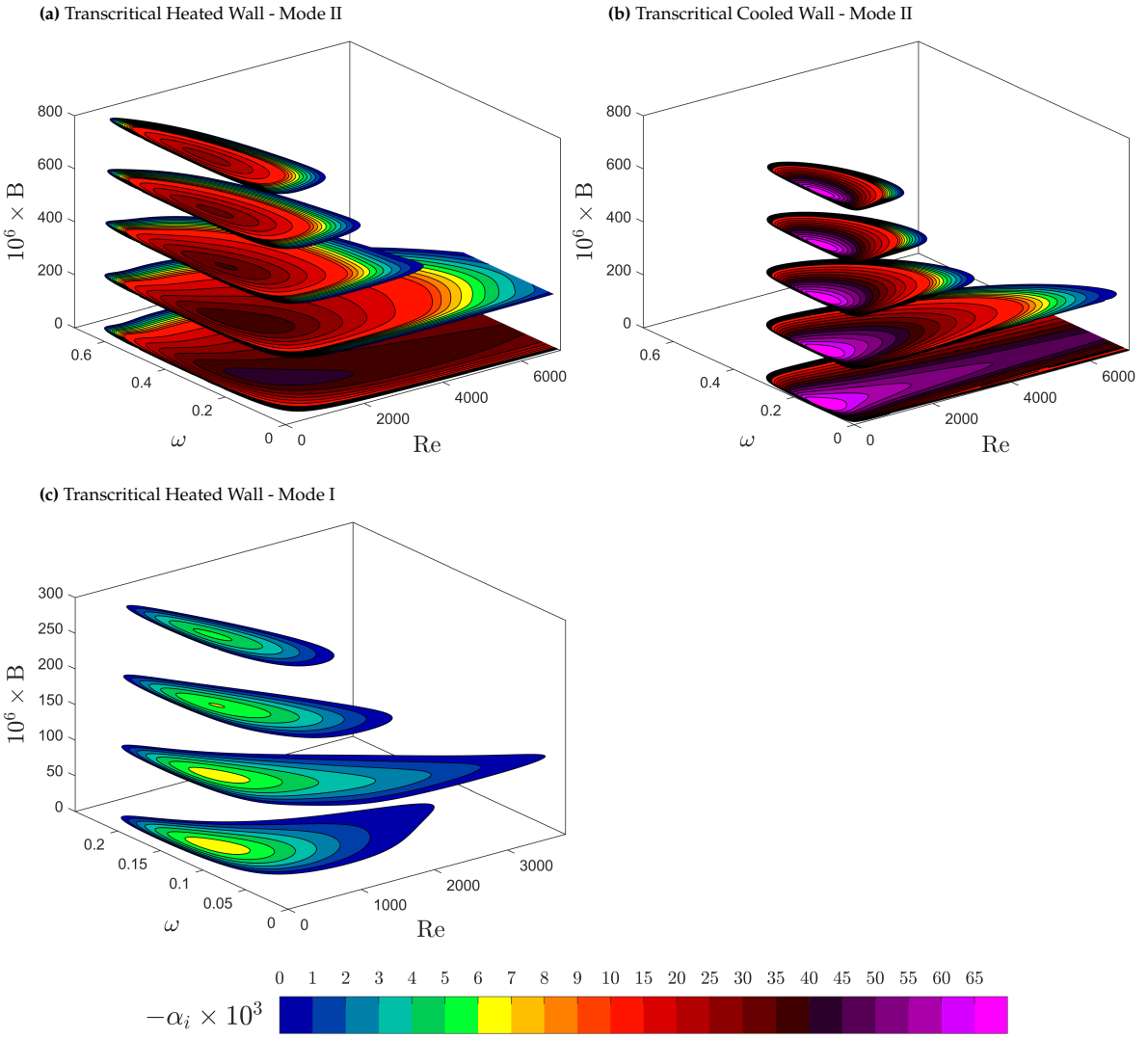

Figure 5.5: Growth rate contour, of mode I and mode II, in the $Re_\delta - \omega - B$ space for the transcritical cases at zero Mach number

As in the subcritical and supercritical regimes, in the transcritical regime, at $M_\infty = 0$, both mode I and mode II are most amplified for 2D perturbations. Regarding mode I, its maximum growth rate is of the same order of magnitude as in the sub- and supercritical regimes. However, with increasing wave number B, the maximum growth rate decays more gradually. Thus, in the TransHM0 case, mode I is unstable for a higher range of wave numbers β when compared to the sub- and supercritical cases. Moreover, unlike in the sub- and supercritical regimes where the unstable surface contracts with increasing B, in the heated wall transcritical regime, the unstable surface expands for some values of B, despite the decrease in the maximum growth rate $-\alpha_i$. Meaning that, for some fixed ω, Re_δ, the

amplification of mode I may increase with B. Regarding mode II, its growth rate is significantly higher than that of mode I. In the heated wall scenario the maximum growth rate of mode I is approximately $\alpha_i = -7 \cdot 10^{-3}$, whereas for mode II it is $\alpha_i = -40 \cdot 10^{-3}$, close to 6 times higher amplification. In the cooled wall scenario, an even higher mode II amplification is obtained, reaching a maximum of $\alpha_i = -74 \cdot 10^{-3}$, representing a tenfold increase. Noticeably, mode II is unstable for a much larger range of wave numbers B when compared to mode I, as evident from the differing scales of the B-axis.

(a) Heated Wall Transcritical Cases - Mode II

Case	Re_δ	ω	$\alpha \times 10^3$
TransHM0	1420	0.232	588.8 - 42.4 i
TransHM^{2}0.2	1004	0.223	504.6 - 34.0 i
TransHM^{2}0.4	710	0.220	451.8 - 27.9 i
TransHM^{2}0.6	556	0.210	398.0 - 22.9 i
TransHM^{2}0.8	454	0.201	356.6 - 19.3 i
TransHM^{2}0.9	386	0.206	354.2 - 18.2 i

(b) Cooled Wall Transcritical Cases - Mode II

Case	Re_δ	ω	$\alpha \times 10^3$
TransCM0	208	0.130	501.4 - 73.6 i
TransCM^{2}0.2	219	0.128	502.4 - 70.8 i
TransCM^{2}0.4	234	0.126	504.2 - 68.5 i
TransCM^{2}0.6	247	0.125	511.3 - 65.2 i
TransCM^{2}0.8	264	0.124	522.7 - 62.6 i
TransCM^{2}0.9	270	0.126	535.2 - 61.3 i
TransCM^{2}1.6	335	0.130	611.9 - 49.4 i

(c) Heated Wall Transcritical Cases - Mode I

Case	Re_δ	ω	$\alpha \times 10^3$
TransHM^{2}0	566	0.134	241.1 - 6.7 i
TransHM^{2}0.2	419	0.134	221.1 - 3.8 i
TransHM^{2}0.4	338	0.132	203.2 - 1.7 i

Table 5.2: Parameters for the most amplified 2D mode I and mode II instability for all the transcritical cases

To investigate the possible three-dimensionality of modes I and II under compressibility effects, the growth rate ratio r is shown in Figure 5.6 for all transcritical cases, with varying Mach number. Table 5.2 provides the parameters for the most amplified 2D wave. In both heated and cooled wall cases, the growth rate of the most amplified mode I or II 2D wave decreases with increasing Mach number. For the heated wall transcritical scenario, the amplification of mode I is only shown for $M^2_\infty \leq 0.6$, as any mode I instability is dampened for $M^2_\infty = 0.8$ and $M^2_\infty = 0.9$. Regarding Figure 5.6, unlike what is observed in the sub- and supercritical regimes, the amplification of mode I decreases with increasing β, regardless of the Mach number. High Mach number ($M^2_\infty = 0.8, 0.9$) are not considered, but given the evolution of r for the plotted cases, it could be expected that further increasing the Mach number will not result in an increase of r with β, i.e. will not result in preferentially 3D waves. For mode II, in both heated and cooled wall scenarios, a sufficiently high Mach number results in 3D waves with higher growth rate than their 2D counterpart. In the heated wall case (panel 5.6a), for $M^2_\infty \geq 0.4$, two local maxima are observed. For low values of β, a local maximum exists at a low Reynolds number. At some $\beta > 0$ a second local maximum appears, plotted with a dashed line, and at higher β, the initial local maximum ceases to exist. For the cooled wall scenario an additional Mach number of $M^2_\infty = 1.6$ is considered as to achieve preferentially 3D waves. It is noted that the ratio r of mode II is higher for the heated wall case when compared to the cooled wall case.

Figure 5.7 shows the ratio c_x/U_s for the waves in Figure 5.6, where the subscript 's' stands for the location of the generalized inflection point (GIP). Note that U_s varies with the Mach number. The phase speed c_x is normalized by the base flow speed at the GIP because, in the limiting case of $Re_\delta \to \infty$, a neutral wave exists with phase speed $c_x = U_s$. That is, the non-trivial neutral inviscid wave meets $c_x = U_s$. Regarding the evolution of c_x/U_s in Figure 5.7, in the heated wall scenario, the phase speed of mode II reveals a similar pattern to what is observed in the sub- and supercritical cases. For increasing β, an increase in the growth rate is accompanied by a decrease of the phase speed c_x, before its subsequent increase. As for mode I, it is a preferentially 2D mode and the phase c_x increasing with β, similar to

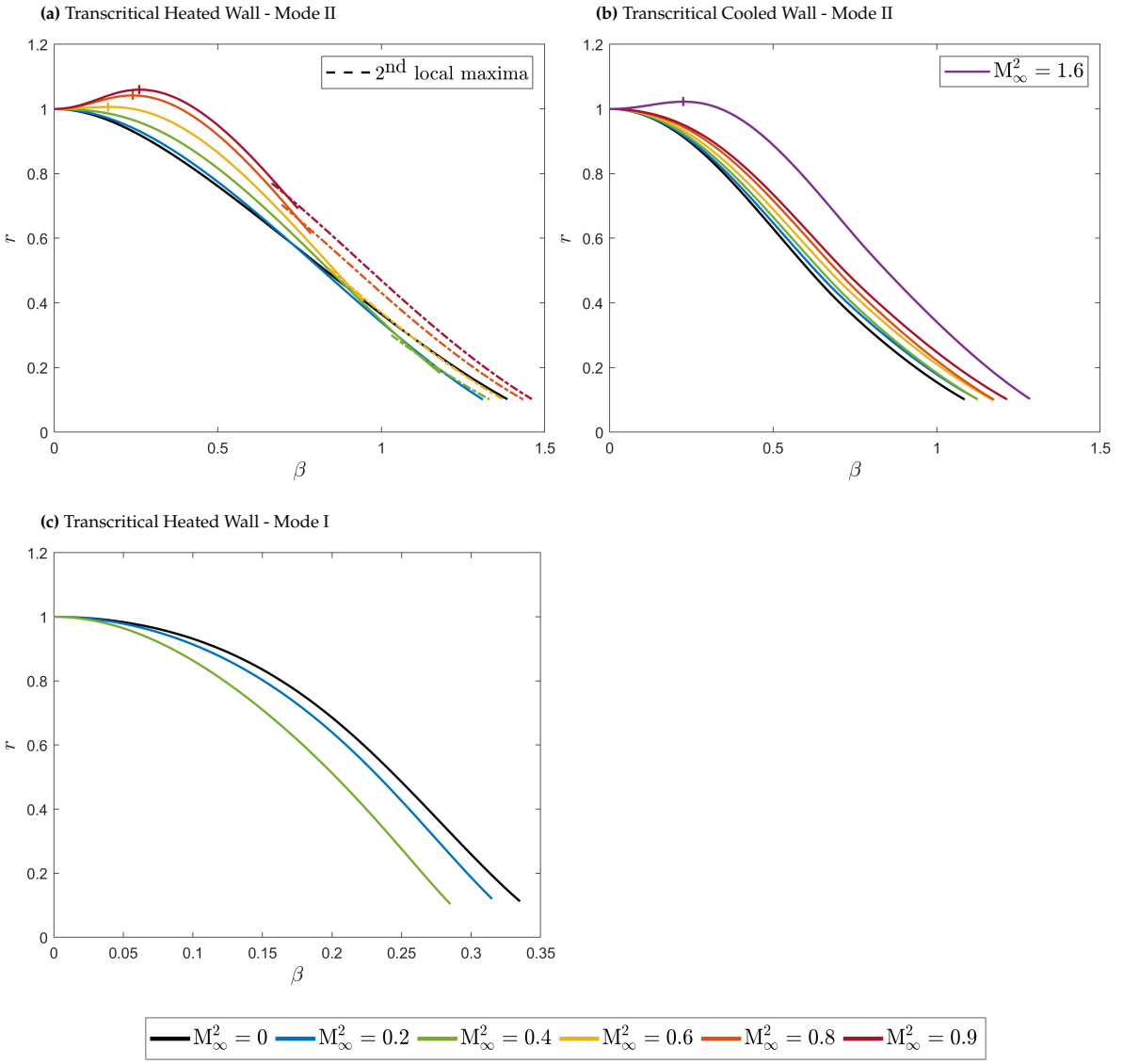

Figure 5.6: Evolution of the growth rate ratio r with the span-wise wave number for all transcritical cases. mode I in panels The maximum obtained growth rate ratio is represented by a vertical dash.

what occurs in the sub- and supercritical regimes. In the cooled wall scenario (panel 5.6b), unlike the other cases, the phase speed c_x of high-β waves is lower when compared to 2D waves. This is justified, as for high wave number β, the Reynolds number Re_δ is also high, such that the global span-wise wave number B is relatively low. For $\mathrm{Re}_\delta \to \infty$, the phase speed must satisfy $1 - 1/\mathrm{M}_\infty < c_x < 1$ (Mack, 1984). Since in the cooled wall case the most amplified 2D wave has $c_x > 1$, it follows that for high β (and high Re_δ) the phase speed of mode II must decrease and eventually reach 1 at some high $\beta, \mathrm{Re}_\delta$. However, looking solely at the high Mach number cases, namely $\mathrm{M}_\infty^2 \geq 0.4$ ($\mathrm{M}_\infty \geq 0.63$), where compressibility is non-negligible, it is observed that in the case of $r > 1$ there is a reversion of the evolution of c_x compared to the $r < 1$ cases. For these boundary layers, in the case of decreasing r, c_x decreases with increasing β, and in the $\mathrm{M}_\infty^2 = 1.6$ ($\mathrm{M}_\infty = 1.26$) case, increasing r is accompanied by increasing c_x. A link remains between the evolution of the amplification $-\alpha_i$ and the evolution of the phase speed c_x.

Figure 5.8 shows the profiles of the most amplified 2D waves alongside the most amplified 3D wave, when considering the highest Mach number on each panel in Figure 5.6. Regarding mode I, in the TransHM^{2}0.4 case, only the 2D perturbation is plotted since no 3D wave has a higher amplification. The

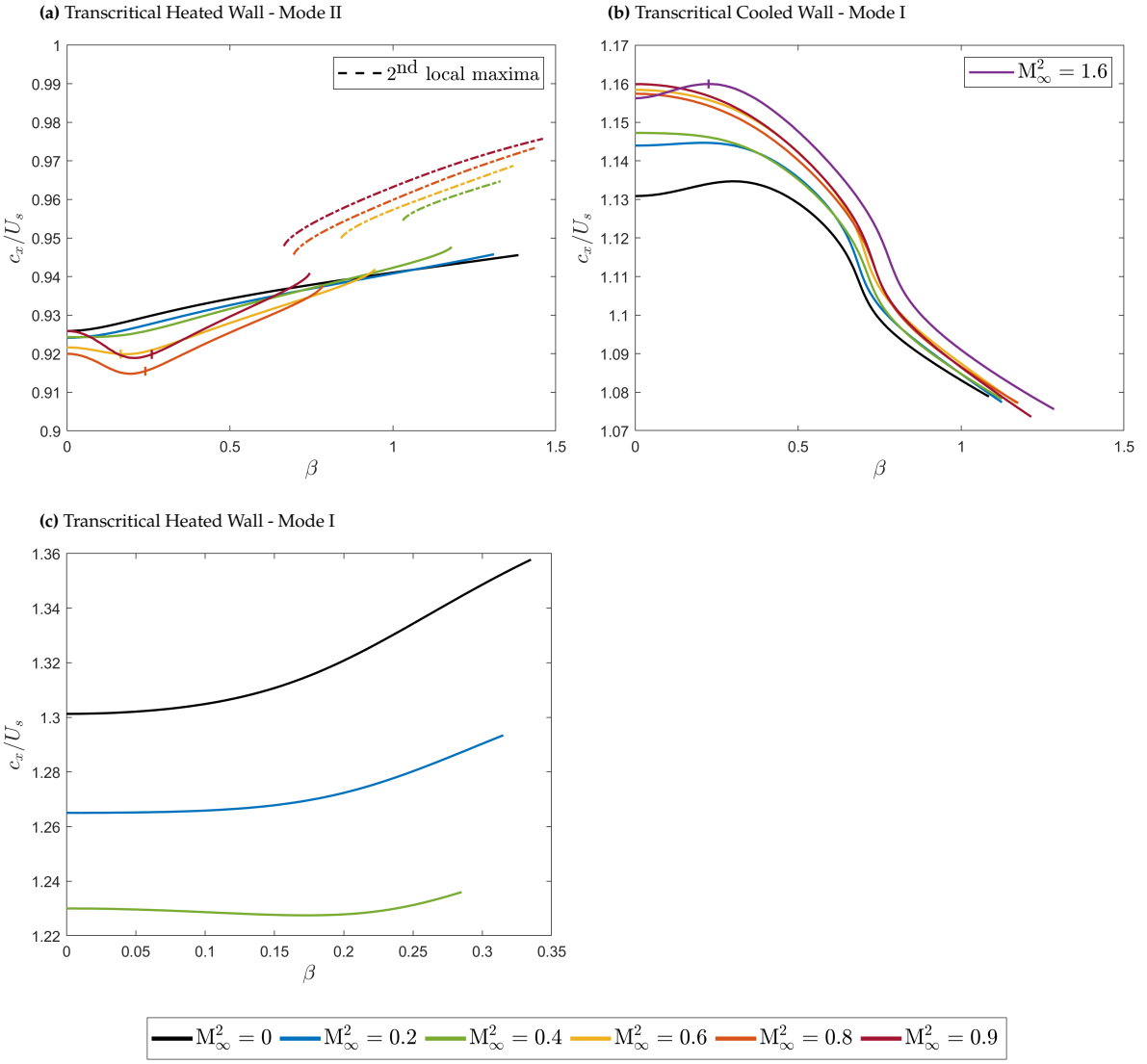

Figure 5.7: Effect of the span-wise wave number β on the phase speed (c_x) of the most amplified mode. All transcritical cases. The point at which maximum growth rate ratio is achieved is marked with a dash.

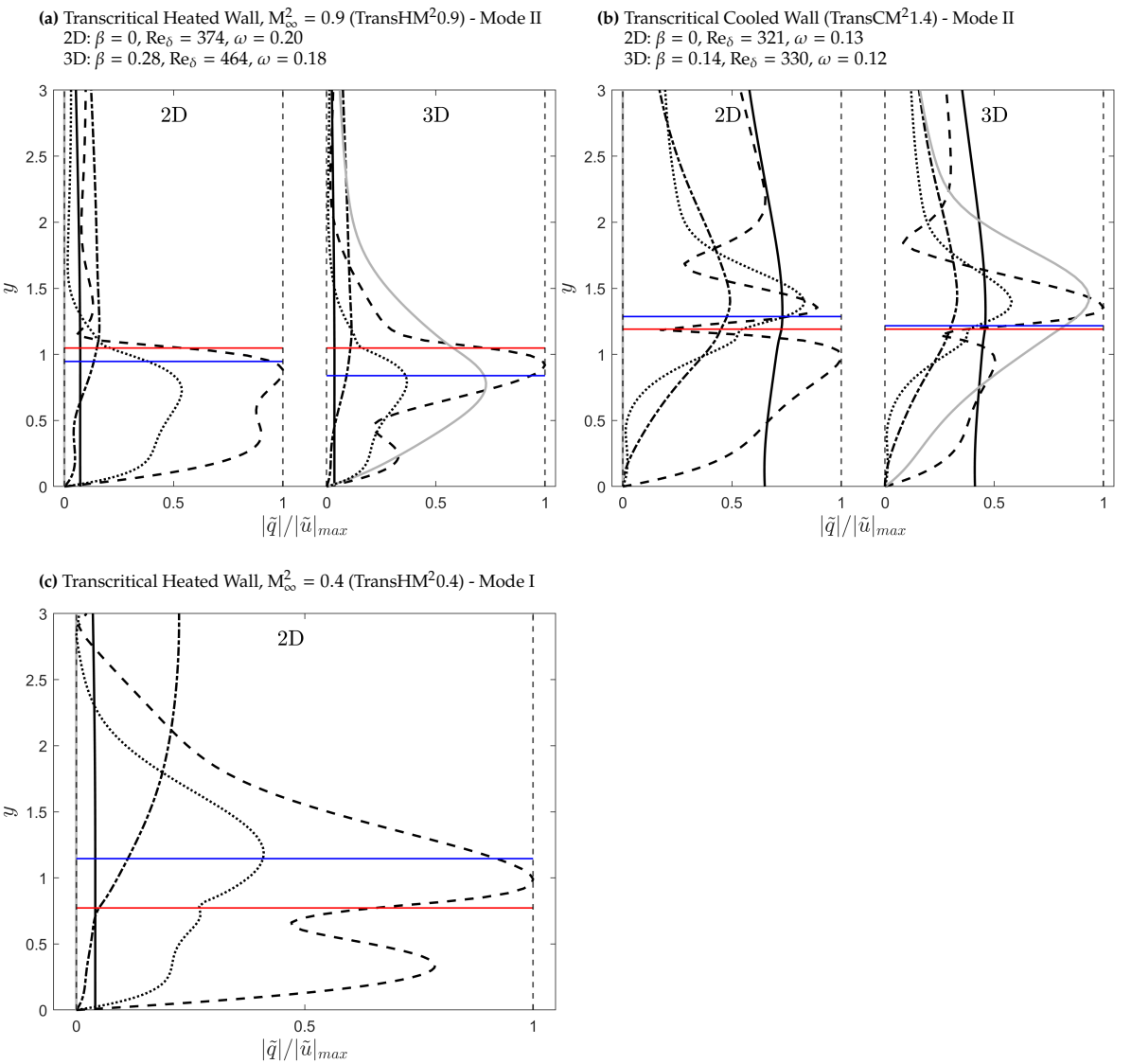

Figure 5.8: Profiles of the most amplified 2D and 3D perturbations. The horizontal blue line represents the location of y_c, and the red line represents the location of the pseudo-boiling point y_w. For each panel, the considered Mach number is the highest Mach considered in the respective panel in Figure 5.6.

stream-wise velocity and temperature perturbations still feature a maxima near the critical layer y_c, just as in the sub- and supercritical regimes (Figure 5.4). Additionally, the stream-wise velocity perturbation has a sharp decrease near the location where $T = T_{pc}$, called the Widom line y_w, and represented by the horizontal red line in Figure 5.6. As for mode II, both in the heated and cooled wall cases, the temperature and velocity perturbations also feature a maxima near the critical layer. In the cooled wall scenario the pressure perturbation is significantly higher when compared to the heated wall case. When comparing the 3D to the 2D perturbation, most noticeably, the most amplified 3D perturbations have greatly reduced near-wall velocity perturbations. Similar to the sub- and supercritical regimes, the perturbation temperature and pressure perturbations are comparatively small for the three-dimensional waves, and the perturbation velocity in the z-direction is sizable with a maximum near the critical layer y_c.

5.3. Inviscid Regime

The limiting case of $\mathrm{Re}_\delta \to \infty$ allows for the simplification of the governing equations for a perturbation q'. The system detailed in Section 2.3.1 is considered. The three-dimensionality of mode II is studied in this simplified framework for all transcritical cases. Figure 5.9 shows the growth rate ratio r in panels 5.9a and 5.9b for the heated and cooled wall scenarios, respectively. Additionally, in panels 5.9c and 5.9d the phase speed scaled by the base flow velocity at the GIP (c_x/U_s) is shown for the most amplified wave.

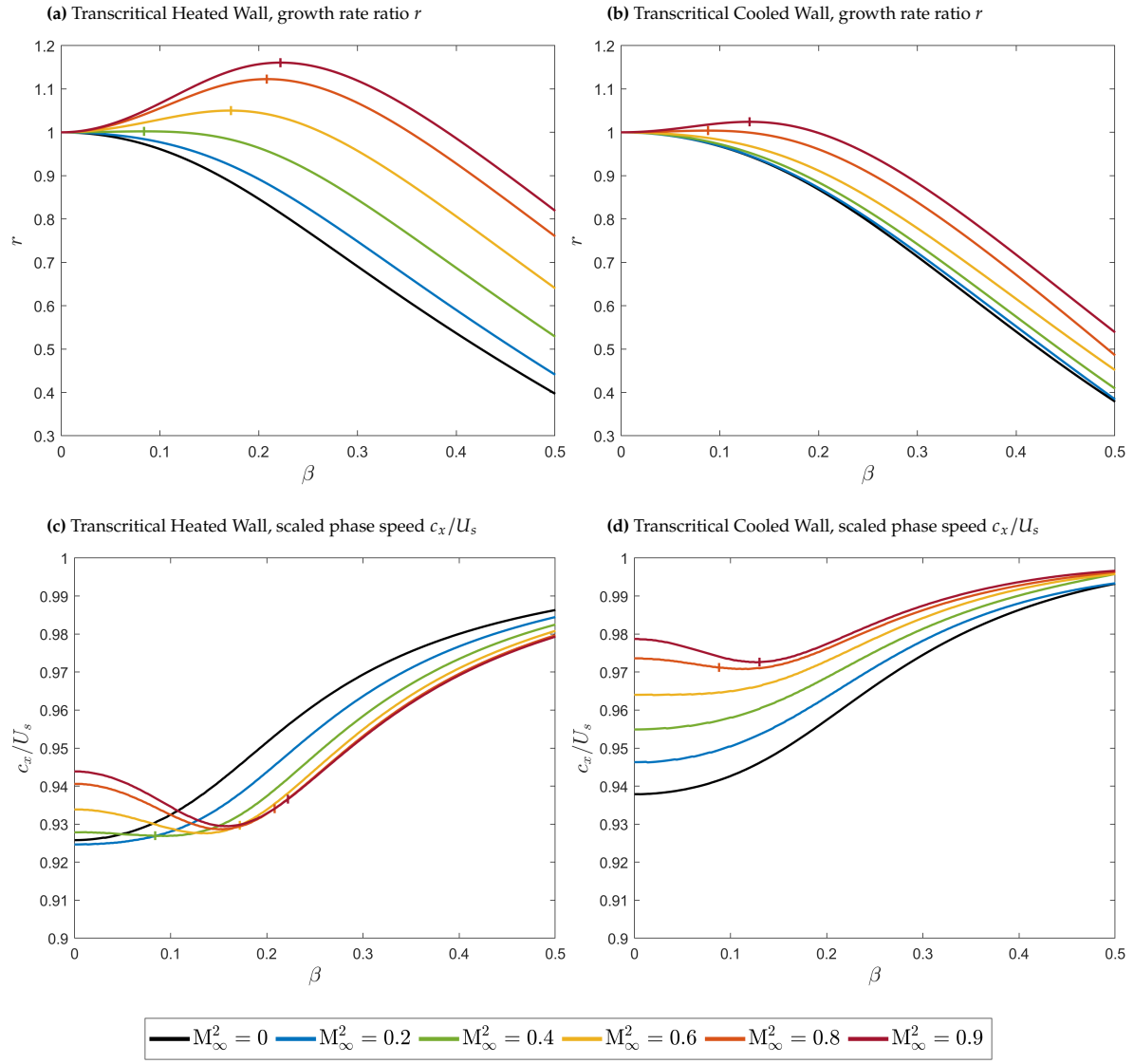

Figure 5.9: Growth rate ratio (panels 5.9a and 5.9b), and scaled phase speed c_x/U_s (panels 5.9c and 5.9d) of the most amplified inviscid wave, optimized over all frequencies w. CO2 BL with P_∞ = 80bar. On the left (panels 5.9a, 5.9c) the transcritical heated wall case with $T_\infty = 0.95T_{pc}$, and $T_{\text{wall}} = 1.05T_{pc}$, and on the right (panels 5.9b, 5.9d) a cooled wall with $T_\infty = 1.05T_{pc}$, and $T_{\text{wall}} = 0.95T_{pc}$

The results show a similar trend to what was initially observed in the sub- and supercritical regimes. A sufficient increase of the Mach number leads to preferentially 3D waves. This is accompanied by a decrease in the phase speed c_x before its subsequent increase. Being that $y_c < y_s$, the critical layer is located below or at the Widom point. Hence, in the heated wall scenario the critical layer is located in a region where the fluid has a gas-like behavior, and conversely, in the cooled wall scenario the

critical layer is in a region where the fluid is liquid-like. The growth rate ratio r is higher for the TransH case when compared to the TransC. It is noted that the phase speed c_x of the most amplified 2D wave increases for high Mach number, and this increase is greater for the cooled wall case. Similar observations could be made when comparing the super- and subcritical regimes in Figures 5.2 and 5.3.

Within the $\mathrm{Re}_\delta \to \infty$ approximation, the system in 2.27 can be written as a single second order differential equation for the pressure perturbation $\tilde{p}$ as

$$\frac{\partial^2 \tilde{p}}{\partial y^2} - \frac{\{\bar{\rho}(U-c_x)^2\}^{(1)}}{\bar{\rho}(U-c_x)^2}\frac{\partial \tilde{p}}{\partial y} - \psi \tilde{p} = 0 \tag{5.2}$$

where the superscripts (i) denote the ith order derivative with respect to the wall normal direction. Equivalently, a second order differential equation for the wall-normal velocity perturbation $\tilde{v}$ exists:

$$\frac{\partial^2 \tilde{v}}{\partial y^2} + \frac{\xi^{(1)}}{\xi}\frac{\partial \tilde{v}}{\partial y} - \left(\psi + \frac{\zeta}{\xi}\right)\tilde{v} = 0 \tag{5.3}$$

with

$$\xi = \frac{\bar{\rho}}{1-M_r^2}; \quad \psi = \left(\alpha^2+\beta^2\right)\left(1-M_r^2\right); \quad \zeta = \frac{1}{U-c_x}\frac{\partial}{\partial y}\left(\xi\frac{\partial U}{\partial y}\right) \tag{5.4}$$

Consider the temporal framework where, in this case, α and β are real. The eigenvalue c_x is complex and forms an eigenvalue pair together with the vector $\tilde{q}$. The temporal framework was found to facilitate the subsequent analysis. Inspiration is taken from Lees and Lin (1946). In the 1946 paper, in the presence of a GIP, given the existence of a neutral 2D wave with wave number $\alpha = \alpha_s$ and $c_x = U_s$, the authors prove the existence of an amplified inviscid wave by considering the total derivative $dc/d(\alpha^2)$. In the present work, interest lies in the amplification of 3D waves. Hence, consider a constant wave number $\alpha > 0$, s.t. c_x is an analytical function of β^2. In the neighbourhood of $\beta = 0$, c_x may be expressed by a Taylor series expansion with respect to $\lambda = \beta^2$:

$$c_x = (c_x)|_{\beta=0} + \lambda \left.\frac{\mathrm{d}c_x}{\mathrm{d}\lambda}\right|_{\beta=0} + \frac{\lambda^2}{2}\left.\frac{\mathrm{d}^2 c_x}{\mathrm{d}\lambda^2}\right|_{\beta=0} + \dots \tag{5.5}$$

If $\mathrm{Im}\left\{\left.\frac{\mathrm{d}c_x}{\mathrm{d}\lambda}\right|_{\beta=0}\right\} \neq 0$, then, at a first order Taylor approximation of c_x, i.e. for small values of β^2, the growth rate should increase/decrease depending on the sign of $\mathrm{Im}\left\{\left.\frac{\mathrm{d}c_x}{\mathrm{d}\lambda}\right|_{\beta=0}\right\}$. Take the derivative of the pressure equation with respect to λ:

$$\frac{\partial^2 \tilde{p}_\lambda}{\partial y^2} - \frac{\{\bar{\rho}(U-c_x)^2\}^{(1)}}{\bar{\rho}(U-c_x)^2}\frac{\partial \tilde{p}_\lambda}{\partial y} - \psi \tilde{p}_\lambda = \left(\frac{\{\bar{\rho}(U-c_x)^2\}^{(1)}}{\bar{\rho}(U-c_x)^2}\right)_\lambda \frac{\partial \tilde{p}}{\partial y} + \psi_\lambda \tilde{p} \tag{5.6}$$

where the subscript λ represents the total derivative with respect to λ. Consider the equality

$$\begin{aligned} &\frac{\partial}{\partial y}\left(\frac{1}{\bar{\rho}(U-c_x)^2}\left[\tilde{p}\frac{\partial \tilde{p}_\lambda}{\partial y} - \tilde{p}_\lambda \frac{\partial \tilde{p}}{\partial y}\right]\right) - \frac{1}{\bar{\rho}(U-c_x)^2}\tilde{p}^2 = \\ &= \frac{1}{\bar{\rho}(U-c_x)^2}\left(\frac{2U^{(1)}}{(U-c_x)^2}\tilde{p}\frac{\partial \tilde{p}}{\partial y} + 2\alpha^2 \mathrm{M}_\infty^2 \frac{1}{\bar{a}^2}(U-c_x)\tilde{p}^2\right)\frac{\mathrm{d}c_x}{\mathrm{d}\lambda} \end{aligned} \tag{5.7}$$

where

$$\frac{\mathrm{d}c_x}{\mathrm{d}\lambda} = \frac{\partial}{\partial \lambda} + \frac{\mathrm{d}c_x}{\mathrm{d}\lambda}\frac{\partial}{\partial c_x} \tag{5.8}$$

was used.

By integrating both sides of Equation 5.7 an expression for $\frac{\mathrm{d}c_x}{\mathrm{d}\lambda}$ is obtained. While numerically it is possible to compute expression 5.7 for any amplified wave, since $\tilde{p}$ is complex, even for the neutral wave with $c_x = U_s$, it is more convenient to make use of the wall normal velocity Equation 5.3. An equivalent expression is obtained:

$$\begin{aligned}\frac{\partial}{\partial y}\left(\xi\tilde{v}\frac{\partial\tilde{v}_\lambda}{\partial y} - \xi\tilde{v}_\lambda\frac{\partial\tilde{v}}{\partial y}\right) + \xi\frac{\partial}{\partial\lambda}\left(\frac{\xi^{(1)}}{\xi}\right)\tilde{v}\frac{\partial\tilde{v}}{\partial y} - \xi\frac{\partial}{\partial\lambda}\left(\psi+\frac{\zeta}{\xi}\right)\tilde{v}^2 = \\ = \left[-\xi\frac{\partial}{\partial c_x}\left(\frac{\xi^{(1)}}{\xi}\right)\tilde{v}\frac{\partial\tilde{v}}{\partial y} + \xi\frac{\partial}{\partial c_x}\left(\psi+\frac{\zeta}{\xi}\right)\tilde{v}^2\right]\frac{\mathrm{d}c_x}{\mathrm{d}\lambda}\end{aligned} \tag{5.9}$$

Integrating from the wall till $y_2 \to \infty$, and solving for $\frac{\mathrm{d}c_x}{\mathrm{d}\lambda}$:

$$\frac{\mathrm{d}c_x}{\mathrm{d}\lambda} = \frac{\int_0^{y_2}\frac{\partial}{\partial y}\left(\bar{\rho}\tilde{v}\frac{\partial\tilde{v}_\lambda}{\partial y} - \bar{\rho}\tilde{v}_\lambda\frac{\partial\tilde{v}}{\partial y}\right)dy + \int_o^{y_2}\xi\frac{\partial}{\partial\lambda}\left(\frac{\xi^{(1)}}{\xi}\right)\tilde{v}\frac{\partial\tilde{v}}{\partial y}dy + \int_0^{y_2} -\xi\frac{\partial}{\partial\lambda}\left(\psi+\frac{\zeta}{\xi}\right)\tilde{v}^2dy}{\int_0^{y_2} -\xi\frac{\partial}{\partial c_x}\left(\frac{\xi^{(1)}}{\xi}\right)\tilde{v}\frac{\partial\tilde{v}}{\partial y}dy + \int_0^{y_2}\xi\frac{\partial}{\partial c_x}\left(\psi+\frac{\zeta}{\xi}\right)\tilde{v}^2dy} \tag{5.10}$$

Regarding the leftmost integral of the numerator:

$$\int_0^{y_2}\frac{\partial}{\partial y}\left(\bar{\rho}\tilde{v}\frac{\partial\tilde{v}_\lambda}{\partial y} - \bar{\rho}\tilde{v}_\lambda\frac{\partial\tilde{v}}{\partial y}\right)dy = \left(\bar{\rho}\tilde{v}\frac{\partial\tilde{v}_\lambda}{\partial y} - \bar{\rho}\tilde{v}_\lambda\frac{\partial\tilde{v}}{\partial y}\right)\Bigg|_{y=0}^{y=y_2} = -\left(\bar{\rho}\tilde{v}\frac{\partial\tilde{v}_\lambda}{\partial y} - \bar{\rho}\tilde{v}_\lambda\frac{\partial\tilde{v}}{\partial y}\right)\Bigg|_{y=y_2} \tag{5.11}$$

where the last equality follows from the identity $\tilde{v} = \tilde{v}_\lambda = 0$. At the upper limit (for $y_2 \to \infty$):

$$\left.\frac{\partial\tilde{v}}{\partial y}\right|_{y\to\infty} = -\sqrt{(\alpha^2+\beta^2)\,(1-M_r^2)}\,\tilde{v}_\infty \tag{5.12a}$$

$$\left.\frac{\partial\tilde{v}_\lambda}{\partial y}\right|_{y\to\infty} = -\sqrt{(\alpha^2+\beta^2)\,(1-M_r^2)}\,(\tilde{v}_\lambda)_\infty - \frac{\mathrm{d}}{\mathrm{d}\lambda}\left[\sqrt{(\alpha^2+\beta^2)\,(1-M_r^2)}\right]\tilde{v}_\infty \tag{5.12b}$$

which for $\beta = 0$ read

$$\left.\frac{\partial\tilde{v}}{\partial y}\right|_{y\to\infty} = -\alpha\sqrt{1-\mathrm{M}_\infty^2(1-c_x)^2}\,\tilde{v}_\infty \tag{5.13a}$$

$$\left.\frac{\partial\tilde{v}_\lambda}{\partial y}\right|_{y\to\infty} = -\alpha\sqrt{1-\mathrm{M}_\infty^2(1-c_x)^2}\,(\tilde{v}_\lambda)_\infty - \left(\frac{1}{2\alpha\sqrt{1-\mathrm{M}_\infty^2(1-c_x)^2}} + \frac{\alpha\mathrm{M}_\infty^2(1-c_x)}{\sqrt{1-\mathrm{M}_\infty^2(1-c_x)^2}}\frac{\mathrm{d}c_x}{\mathrm{d}\lambda}\right)\tilde{v}_\infty \tag{5.13b}$$

substitution in 5.11 yields

$$\int_0^{y_2}\frac{\partial}{\partial y}\left(\bar{\rho}\tilde{v}\frac{\partial\tilde{v}_\lambda}{\partial y} - \bar{\rho}\tilde{v}_\lambda\frac{\partial\tilde{v}}{\partial y}\right)dy = -\left(\frac{1}{2\alpha\sqrt{1-\mathrm{M}_\infty^2(1-c_x)^2}} + \frac{\alpha\mathrm{M}_\infty^2(1-c_x)}{\sqrt{1-\mathrm{M}_\infty^2(1-c_x)^2}}\frac{\mathrm{d}c_x}{\mathrm{d}\lambda}\right)\tilde{v}^2|_{y_2\to\infty} \tag{5.14}$$

and since $\tilde{v}|_{y_2\to\infty} = 0$, then

$$\int_0^{y_2}\frac{\partial}{\partial y}\left(\bar{\rho}\tilde{v}\frac{\partial\tilde{v}_\lambda}{\partial y} - \bar{\rho}\tilde{v}_\lambda\frac{\partial\tilde{v}}{\partial y}\right)dy = 0 \tag{5.15}$$

Regarding the partial derivative terms of Equation 5.10:

$$\frac{\partial}{\partial\lambda}\left(\frac{\xi^{(1)}}{\xi}\right) = \frac{-\{M_r^2\}^{(1)}}{(\alpha^2+\beta^2)(1-M_r^2)^2} \tag{5.16}$$

$$\frac{\partial}{\partial\lambda}\left(\psi+\frac{\zeta}{\xi}\right)=1-\frac{2\alpha^2\mathrm{M}_\infty^2}{\bar{a}(\alpha^2+\beta^2)^2(1-M_r^2)^2}\left\{\frac{U-c_x}{\bar{a}}\right\}^{(1)}U^{(1)} \tag{5.17}$$

$$\frac{\partial}{\partial c_x}\left(\frac{\xi^{(1)}}{\xi}\right)=\frac{-2\alpha^2\mathrm{M}_\infty^2}{\bar{a}(\alpha^2+\beta^2)(1-M_r^2)}\left[\left\{\frac{U-c_x}{\bar{a}}\right\}^{(1)}\left(1+\frac{2M_r^2}{1-M_r^2}\right)-(U-c_x)\frac{\bar{a}^{(1)}}{\bar{a}^2}\right] \tag{5.18}$$

$$\frac{\partial}{\partial c_x}\left(\psi+\frac{\zeta}{\xi}\right)=\frac{\left\{\bar{\rho}U^{(1)}\right\}^{(1)}}{\bar{\rho}(U-c_x)^2}+\frac{2\alpha^2\mathrm{M}_\infty^2}{\bar{a}^2}\left[(U-c_x)+\frac{U^{(1)}}{(\alpha^2+\beta^2)(1-M_r^2)}\left(\frac{\bar{a}^{(1)}}{\bar{a}}-\frac{\{M_r^2\}^{(1)}}{1-M_r^2}\right)\right] \tag{5.19}$$

The term $\frac{1}{\bar{\rho}(U-c_x)^2}\left\{\bar{\rho}U^{(1)}\right\}^{(1)}$ is the only singular term, and is found in the denominator. Meaning, when integrating while considering the neutral wave with $c_x = U_s$, all but the singular term are real and finite. As shown by Lees and Lin (1946), the point at which $M_r^2 = 1$ is an apparent singularity: under the formulation in Equation 2.27 the only singularity occurs at $U = c_x$. Thus, when considering the neutral wave with $c_x = U_s$ (with corresponding wave number $\alpha = \alpha_s$), the sign of imaginary part of $(dc_x/d\lambda)|_{\alpha_s}$ is given by:

$$\operatorname{sgn}\left\{\operatorname{Im}\left\{\left.\frac{\mathrm{d}c_x}{\mathrm{d}\lambda}\right|_{\alpha_s}\right\}\right\}=\operatorname{sgn}\{-\text{Num.}\cdot\operatorname{Im}\{\text{Den.}\}\} \tag{5.20}$$

where Num. stands for the numerator of Equation 5.10, and Den. its denominator.

Regarding the singular term, Lees and Lin consider the same quantity and express the base density and stream-wise velocity fields in a Taylor series centred around $y = y_c = y_s$:

$$\begin{aligned}\int_0^{y_2}\left[\frac{\xi}{\bar{\rho}(U-c_x)^2}\left\{\bar{\rho}U^{(1)}\right\}^{(1)}\tilde{v}^2\right]dy&=\\ &=\int_0^{y_2}\frac{\left[\tilde{v}_c^2+2\tilde{v}_c\tilde{v}_c^{(1)}(y-y_c)+\dots\right]\left[\xi_c\left\{\bar{\rho}U^{(1)}\right\}_c^{(2)}(y-y_c)+\dots\right]}{\bar{\rho}_c\left(U_c^{(1)}\right)^2(y-y_c)^2\left[1+\left(\frac{U_c^{(2)}}{2U_c^{(1)}}+\frac{\bar{\rho}_c^{(1)}}{2\bar{\rho}_c}\right)(y-y_c)+\dots\right]^2}dy\end{aligned} \tag{5.21}$$

where the subscript 'c' indicates that the function is being evaluated at $y = y_c$. The integrand of Equation 5.21 is a Laurent series centred around y_c. The imaginary part is equal to

$$\begin{aligned}\operatorname{Im}\left\{\int_0^{y_2}\left[\frac{\xi}{\bar{\rho}(U-c_x)^2}\left\{\bar{\rho}U^{(1)}\right\}^{(1)}\tilde{v}^2\right]dy\right\}&=\\ &=\frac{1}{2i}\oint_\gamma\frac{\left[\tilde{v}_c^2+2\tilde{v}_c\tilde{v}_c^{(1)}(y-y_c)+\dots\right]\left[\xi_c\left\{\bar{\rho}U^{(1)}\right\}_c^{(2)}(y-y_c)+\dots\right]}{\bar{\rho}_c\left(U_c^{(1)}\right)^2(y-y_c)^2\left[1+\left(\frac{U_c^{(2)}}{2U_c^{(1)}}+\frac{\bar{\rho}_c^{(1)}}{2\bar{\rho}_c}\right)(y-y_c)+\dots\right]^2}dy\end{aligned} \tag{5.22}$$

where γ is a positively oriented simple closed curve around y_c. Since the singularity is isolated, we may arbitrarily choose $\gamma = \{y : |y - y_c| = \epsilon \to 0\}$. From Cauchy residue theorem, Equation 5.22 yields

$$\operatorname{Im}\left\{\int_0^{y_2}\left[\frac{\xi}{\bar{\rho}(U-c_x)^2}\left\{\bar{\rho}U^{(1)}\right\}^{(1)}\tilde{v}^2\right]dy\right\}=\pi\left|\tilde{v}_c\right|^2\frac{\left\{\bar{\rho}U^{(1)}\right\}_c^{(2)}}{\left(U_c^{(1)}\right)^2}<0 \tag{5.23}$$

The last inequality follows from Fjørtoft's theorem, extended to varying density fluids, which states $\left\{\bar{\rho}U^{(1)}\right\}_s^{(2)} < 0$, and thus $\operatorname{Im}\{\text{Den.}\} < 0$ for $\alpha = \alpha_s$. In the context of trancritical flows, as shown by Bugeat et al. (2022), the maximum of $\bar{\rho}U^{(1)}$ at the GIP is associated with a minimum of kinematic

viscosity. Near the Widom point, viscosity effects dominate the balance of stream-wise momentum such that $\{\overline{\mu}U^{(1)}\}^{(1)} \approx 0$, from which $\left\{\bar{\rho}U^{(1)}\right\}^{(1)} \approx -\bar{\rho}U^{(1)}\overline{v}^{(1)}$. The existence of a GIP is associated with an extremum of $\overline{v}$: $\overline{v}_s^{(1)} = 0$. From which, $\left\{\bar{\rho}U^{(1)}\right\}_s^{(2)} \approx -\left\{\bar{\rho}U^{(1)}\overline{v}^{(2)}\right\}_s$, and, in order to satisfy Fjørtoft's criterion, considering $U_s^{(1)} > 0$, the kinematic viscosity is at a minimum at the GIP: $\overline{v}_s^{(2)} > 0$. Note however that the result in Equation 5.23 is general for all boundary layer flows.

Figure 5.10 confirms that $\left\{\bar{\rho}U^{(1)}\right\}_c^{(2)} < 0$. The quantity $\left\{\bar{\rho}U^{(1)}\right\}^{(1)}$ is plotted for both heated (panel 5.10a) and cooled (panel 5.10b) wall cases and various Mach numbers. The neutral inviscid mode with $c_x = U_s$ has its critical layer at the GIP, i.e. the location where $\left\{\bar{\rho}U^{(1)}\right\}^{(1)} = 0$.

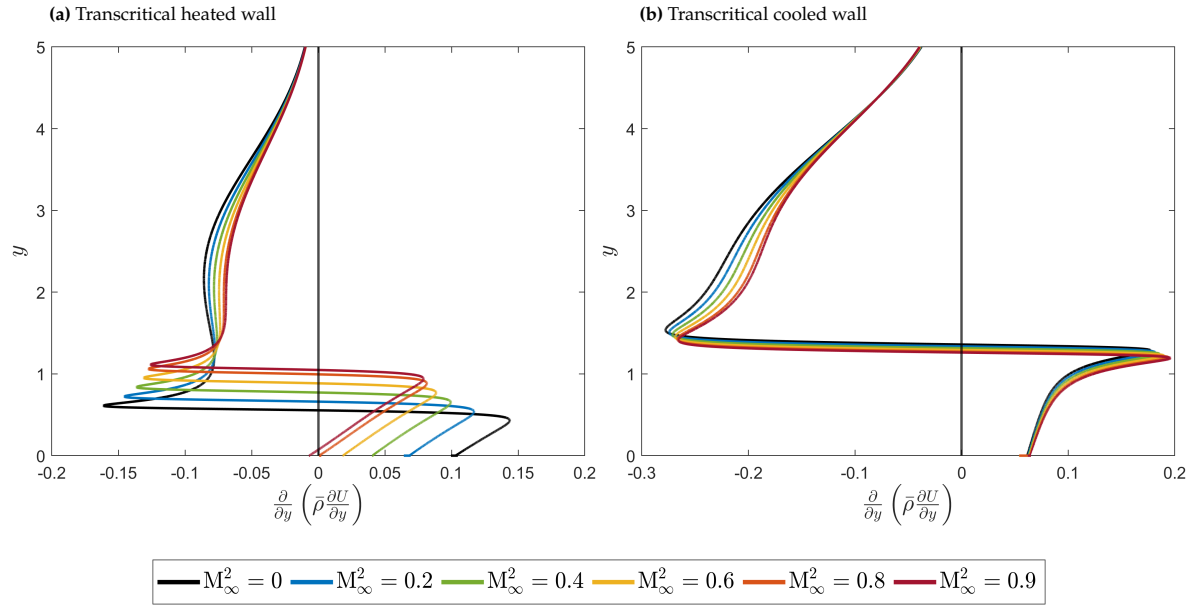

Figure 5.10: Generalized inflection point $\left\{\bar{\rho}U^{(1)}\right\}^{(1)}$ for the transcritical boundary layers cases. A heated wall in 5.10a, and cooled wall in 5.10b.

Record Equation 5.20, since, as shown in Equation 5.23, Im{Den.} < 0, for constant $\alpha = \alpha_s$, an inviscid mode is most amplified for a 3D wave if Num. > 0. Consider then the numerator of Equation 5.10, it reads

$$\underbrace{\int_0^{y_2} -\xi\tilde{v}^2 dy}_{a_1} + \int_0^{y_2} \frac{\xi\{M_r^2\}^{(1)}}{(\alpha^2+\beta^2)(1-M_r^2)^2}\left(\frac{U^{(1)}}{U-c_x}\tilde{v}^2 - \tilde{v}\tilde{v}^{(1)}\right)dy \tag{5.24}$$

For the zero Mach case, the relative Mach number M_r is zero and $\xi \to \bar{\rho}$. The leftmost integral is the only non-zero term, and being that its integrand is negative for all y, then $a_1 \in \mathbb{R}_-$, and $\mathrm{Im}\left\{\frac{dc}{d\beta^2}\right\} < 0$. Thus, for $\mathrm{M}_\infty \to 0$, the neutral inviscid wave with $\alpha = \alpha_s$ is, for small values of β^2, most amplified for $\beta = 0$. The rightmost integral can be decomposed into two terms:

$$\begin{aligned} &\underbrace{\int_0^{y_2} -\xi\tilde{v}^2 dy}_{a_1} + \\ &\underbrace{+\int_0^{y_2} \xi\frac{-\{M_r^2\}^{(1)}}{(\alpha^2+\beta^2)(1-M_r^2)^2}\tilde{v}\tilde{v}^{(1)}dy}_{a_2} + \underbrace{\int_0^{y_2} \xi\frac{2\alpha^2\mathrm{M}_\infty^2}{\bar{a}(\alpha^2+\beta^2)^2(1-M_r^2)^2}\left\{\frac{U-c_x}{\bar{a}}\right\}^{(1)}U^{(1)}\tilde{v}^2 dy}_{a_3} \end{aligned} \tag{5.25}$$

Consider a subsonic wave ($|M_r| < 1$), such that $\xi > 0$, and assume that the relative Mach number is an increasing function with respect to the wall normal direction, meaning $\left\{\frac{U-c_x}{\tilde{a}}\right\}^{(1)} \geq 0$. The integrand of a_1 remains negative for all y, s.t. $a_1 \in \mathbb{R}_-$. Regarding the term a_2. The square of the relative Mach number M_r^2 is a decreasing function for $y < y_c$, and an increasing function for $y > y_c$. On the contrary, the perturbation $\tilde{v}$ is, generally, an increasing/decreasing function for $(y < y_c)/(y > y_c)$. All other terms in a_2 are positive, thus it is expected that a_2 is positive ($a_2 \in \mathbb{R}_+$). The integrand of a_3 is positive for all y, meaning $a_3 \in \mathbb{R}_+$. The two zero-terms when $M_\infty = 0$ (terms a_2 and a_3) are expected to be positive for $M_\infty > 0$. Thus, for $M_\infty > 0$, the terms a_2 and a_3 have a positive contribution in the further amplification of the wave with $\alpha = \alpha_s$ for $\beta > 0$. Figure 5.11 shows, for increasing Mach number, the values of a_1, and $(a_2 + a_3)$ for the transcritical heated wall case with $T_\infty = 0.95T_{pc}$, $T_{\text{wall}} = 1.05T_{pc}$. The temporal framework is used. The 2D ($\beta = 0$) neutral wave with $c = U_s$ is considered, note that U_s varies with the Mach number, as does the wave number α_s. The perturbation wall-normal velocity $\tilde{v}$ is normalized by:

$$\frac{\tilde{v}}{\max\{|\tilde{v}|\}} \frac{|\tilde{v}(y \to \infty)|}{\tilde{v}(y \to \infty)} \tag{5.26}$$

such that $\tilde{v}$ is real.

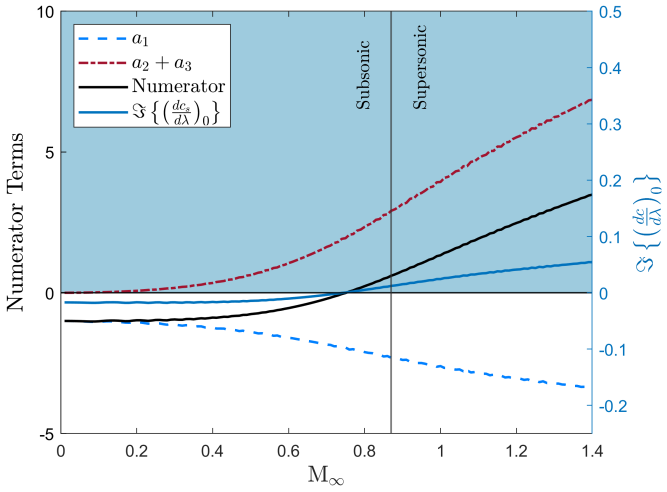

Figure 5.11: Evolution of the terms a_1 and a_2+a_3 of the numerator of Equation 5.10 with increasing Mach number. CO2 transcritical boundary layer with heated wall. The temperature boundary conditions are $T_\infty = 0.95T_{pc}$, and $T_{\text{wall}} = 1.05T_{pc}$. For each Mach number the neutral inviscid wave with $\alpha = \alpha_s > 0$ and $c_x = U_s$, where the subscript 's' denotes the GIP, is considered. The imaginary part of $(dc_x/d\lambda)\,|_{\alpha_s}$ is plotted on the right y-axis. The vertical line indicates that the neutral wave is sonic, that is $\max\{|M_r^2|\} = 1$

The derivative $dc/d\lambda$ in Figure 5.11 is calculated from Equation 5.10, and validated using a 4th order forwards difference method by solving the eigenvalue problem in Equation 2.27 for increasing β^2. The term $(a_2 + a_3)$ is observed to have a positive contribution towards the increase of $\text{Im}\{dc_s/d\lambda\}$. The wave with $\alpha = \alpha_s$ reaches a higher amplification for $\beta > 0$ still in the subsonic regime, where in this case subsonic refers to the relative Mach number M_r. The imaginary part of Equation 5.10 continues to increase in the supersonic regime.

Considering amplified waves. Figure 5.12 shows the imaginary (panel 5.12a) and real part (panel 5.12b) of $dc_x/d\lambda$. Three values for α are considered, and additionally, for each Mach number the value of α which maximizes the amplification of the 2D wave is considered ($\alpha_{\max}$).

For large Mach number the imaginary part of $dc_x/d\lambda$ is positive, and the real part is negative. For low Mach number the opposite is true. Just as observed in Figure 5.9 a correlation exists between the higher amplification of a 3D wave and the decrease of the phase speed c_x. For high Mach number notice

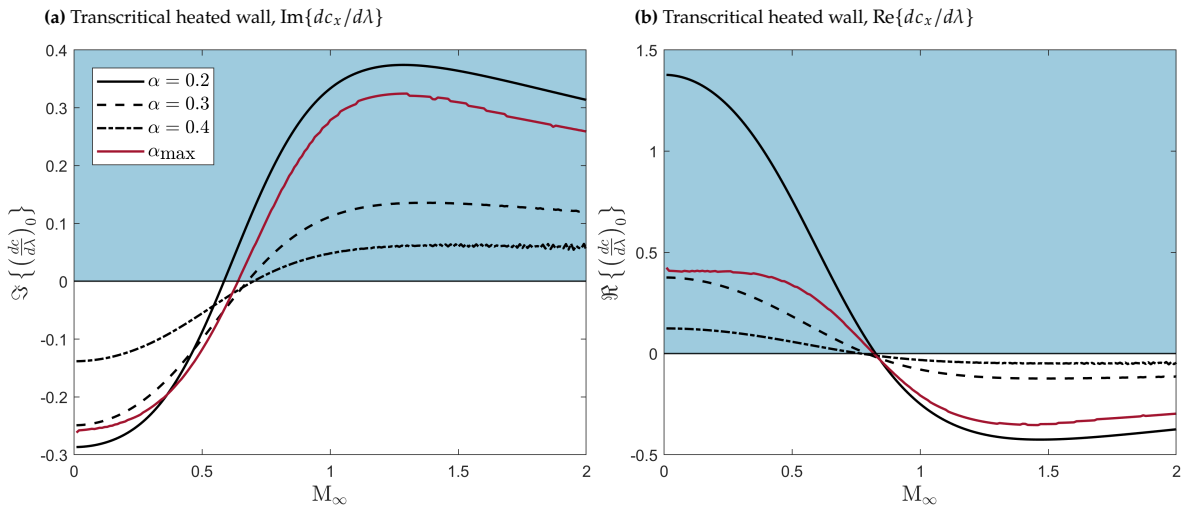

Figure 5.12: Evolution of $dc_x/d\lambda$ with increasing Mach number. The imaginary part on panel 5.12a, and the real part in 5.12b. Various wave number α. The red line represents the most amplified 2D wave for each Mach number.

that the imaginary and real part start to decrease in absolute terms. This is expected, as in the limit of $M_\infty \to \infty$ all terms in Equation 5.25 are zero, and the three-dimensionality of the 2D neutral wave depends on the higher order terms of Equation 5.5.

An important set of inviscid unstable waves in compressible hypersonic boundary layers are Mack's higher modes, and in particular Mack's second mode. The current discussion would suggest that the neutral second mode, with $c = U_s$, is most amplified for $\beta > 0$. However, it is known that Mack's second mode is preferentially two-dimensional, that is, the mode is most amplified for a 2D wave. To highlight some differences between mode II and Mack's second mode a brief look into the latter follows. Figure 5.13 shows, in the $\alpha - \beta$ space, the temporal amplification of Mack's second mode. An air boundary layer, modelled as calorically perfect gas, is considered. The Prandtl number is constant and equal to Pr = 0.72. The temperature at the free-stream is $T_\infty = 61.6$K, and the wall is adiabatic. The free-stream Mach number is $M_\infty = 4.5$.

It is observed that, in agreement with the analysis of Equation 5.25, for high α, close to α_s, the amplification of $\beta > 0$ waves is higher than at $\beta = 0$. The horizontal red line represents the wave number α for which $\text{Im}\{(dc/d\lambda)_0\} = 0$, above which three-dimensional wave are more amplified than their 2D counterpart. If the mode with $\alpha = \alpha_s$ meets $\text{Im}\{dc_s/d\lambda\} > 0$, then an immediate difference between Mack's second mode and mode II is the sign of $\text{Re}\{dc_s/d\lambda\}$. In the case of mode II since $y_c \leq y_s$, it must be that for any amplified mode $c_r < U_s$, such that $\text{Re}\{dc_s/d\lambda\} < 0$. On the contrary, for Mack's second mode $y_c \geq y_s$, and $\text{Re}\{dc_s/d\lambda\} > 0$. In fact, for Mack's second mode $\text{Re}\{dc/d\lambda\} > 0$ for all 2D waves, such that the critical layer rises with increasing β, regardless of the considered wave number α. In contrast, when considering mode II, an increase of β can lead to a decrease in the height of the critical layer y_c, which, as shown in 5.12 is connected with the increase of its temporal growth rate.

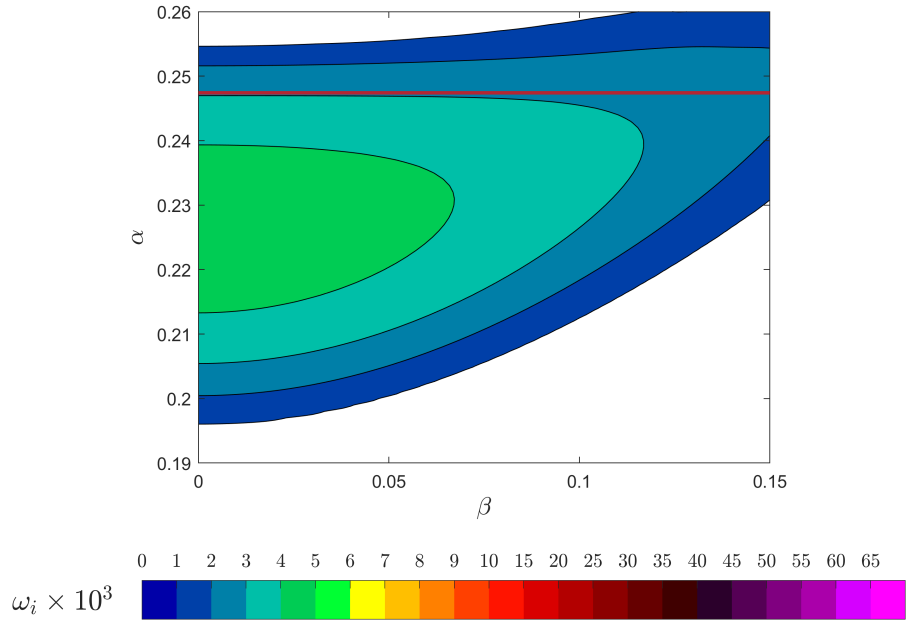

Figure 5.13: Temporal amplification of Mack's second mode. For α close to α_s, three-dimensional waves are more amplified than their 2D counterpart, in agreement with the analysis of Equation 5.25

6

Results: Non-Modal Stability Analysis

In this chapter the non-modal stability of SCO2 boundary layers is investigated. The study is restricted to the zero Mach number cases ($M_\infty \to 0$). The energy growth of perturbations is calculated in the $\beta - \omega$ space, and the Reynolds number is fixed. The Reynolds number is chosen at random, subject to the constraint that unstable modes are present at such a Reynolds number. For the purposes of this study, a Reynolds number of 1000 is selected ($Re_\delta = 1000$). In Section 6.1 the sub- and supercritical regimes considered, and in Section 6.2 the transcritical cases are analyzed.

6.1. Sub- and Supercritical Regimes

In this section, the non-modal stability of the sub- and supercritical cases at zero Mach number is analyzed. Figure 6.1 shows, in the $\omega - \beta$ space, the maximum spacial energy amplification $G_{max}(\omega, \beta)$. For each panel, the kinetic energy growth (KE norm) is shown on the left, and on the right the GE energy norm in Equation 2.50. The colored region represents the maximum energy amplification (G_{max}), while in the grey region modal instabilities are present such that maximum energy amplification is infinite. The outside-most contour line in the grey region is the neutral curve. Subsequent contour lines are equally spaced by 10% of the maximum modal amplification $\max\{\alpha_i\}$.

In every case, the energy amplification G_{max} features a global maximum for an oblique stationary wave ($\beta \neq 0$, $\omega = 0$). The optimal wave number β_{opt}, energy amplification G_{opt}, and stream wise distance where energy amplification reaches its maximum x_{opt} are given in the caption of each panel. The similarity between the SubHM0 and SupCM0 cases, and the SubCM0 and SupHM0 cases initially observed in Figure 5.1 remains: a symmetry of the free-stream and wall temperature boundary conditions around the pseudo-critical temperature produce a similar non-modal response. Both energy norms produce very similar results. The optimal energy amplification when only considering kinetic effects varies between 4464 to 5268, being higher for the cooled wall cases. The inclusion of the thermodynamic terms e' and ρ' in the energy norm only result in an increase of the optimal energy amplification by around 2% in the subcritical regimes and around 4% in the supercritical regimes. Thus, the energy amplification in these regimes is largely due to kinetic energy amplification.

For the RG energy norm, Figure 6.2 shows the optimal initial condition q'_{opt}, and the resulting disturbances at maximum growth $q'_{out}(x = x_{opt})$. These correspond to the respective maximum in Figure 6.1. The optimal disturbance consists in wall-normal and span-wise velocities, and the amplified disturbances in stream-wise velocity and temperature perturbations. These disturbances correspond to the well-known stream-wise vortexes for the initial condition, and in stream-wise streaks of alternating high/low stream-wise velocity and temperature for the resulting disturbance (Hanifi et al., 1996). The

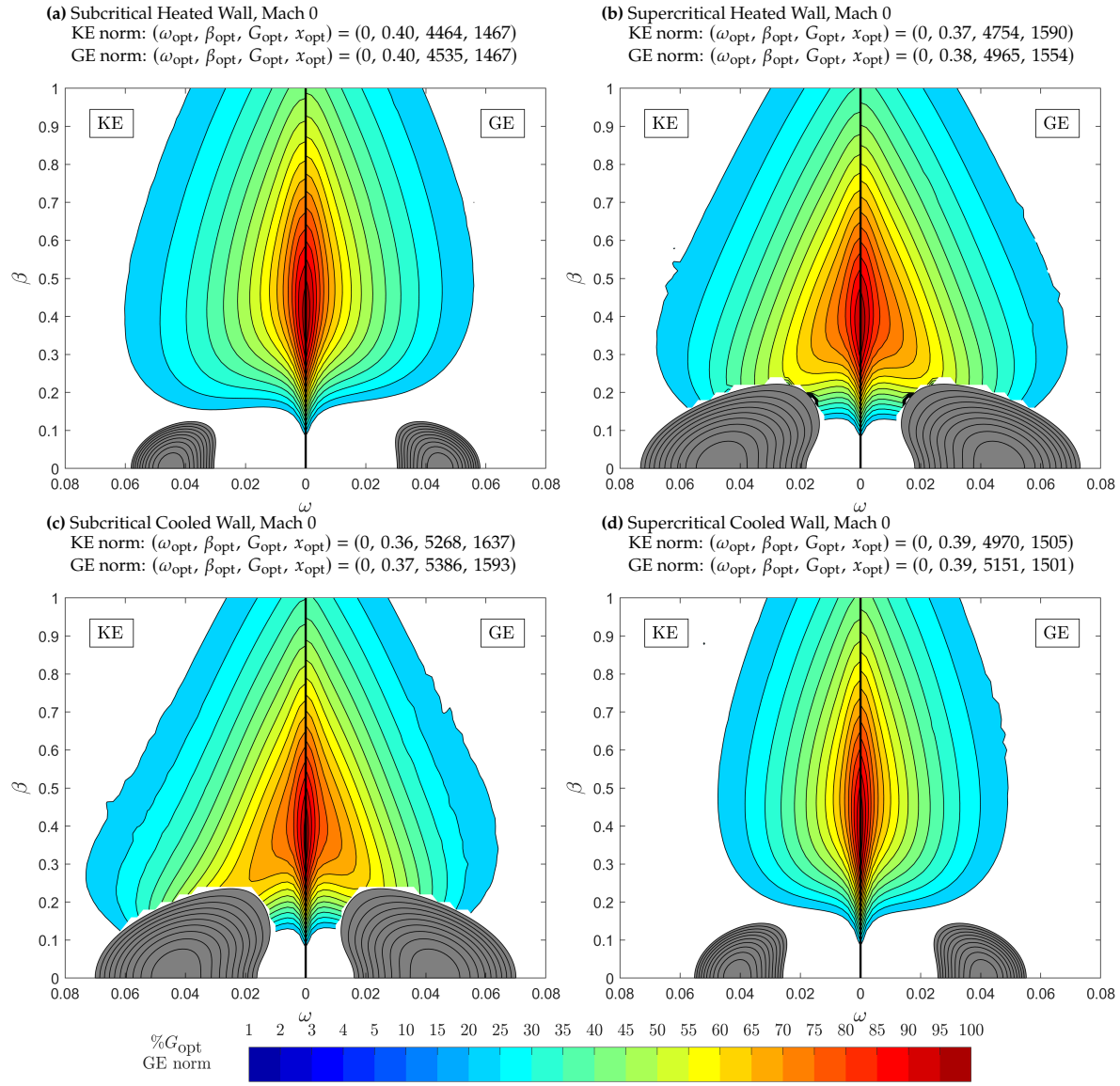

Figure 6.1: Contours of maximum spatial energy amplification (G_{max}) with varying stream-wise and span-wise wave number. The Reynolds number is $Re_\delta = 1000$. The considered boundary layers are the cases SubHM0, SupHM0, SubCM0, and SubCM0, in panels 6.1a, 6.1b, 6.1c, and 6.1d, respectively

physical explanation for these disturbance amplifications is the lift-up effect, also observed in both incompressible and compressible ideal gas boundary layers (Ellingsen and Palm, 1975, Landahl, 1980). While the resulting optimal disturbances do contain noticeable temperature and density perturbations the energy is mostly kinetic: the kinetic terms in Equation 2.51 contain between 96% and 98% of the total energy.

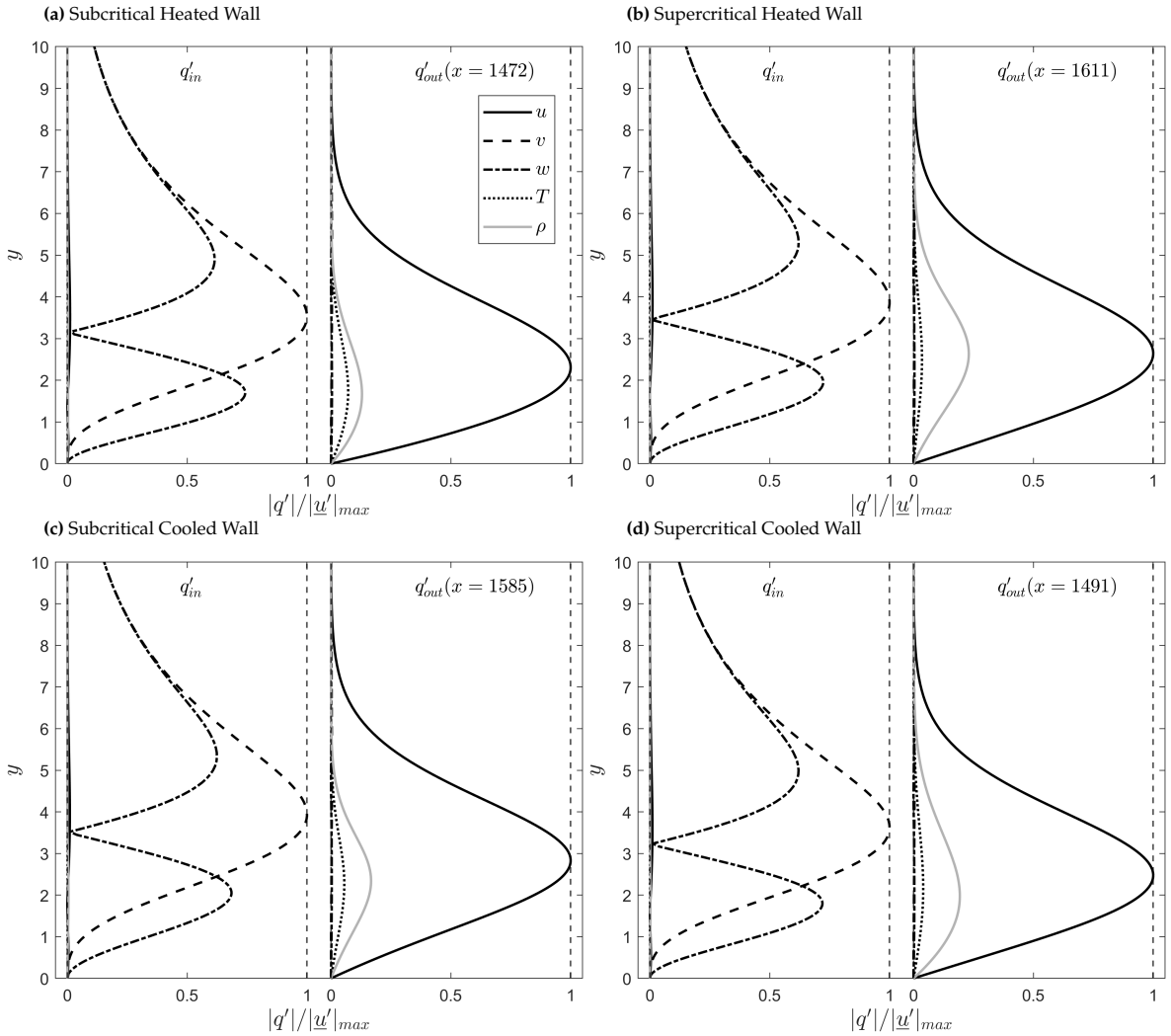

Figure 6.2: Optimal disturbances corresponding to Figure 6.1.

6.2. Transcritical Regimes

In this section the non-modal stability analysis is carried out for the transcritical regimes at zero Mach number (cases TransHM0 and TransCM0). Figure 6.3 shows the maximum spatial energy amplification $G_{\max}(\omega, \beta)$, in the $\omega - \beta$ space. The area where modal instabilities are present is in grey, with the contour lines corresponding to a decrease in 10% of the maximum modal amplification. The outermost contour line is the neutral curve. Note that, in the transcritical heated wall case two modal instabilities are present, corresponding to mode I and mode II, studied in Section 5.2. While in the cooled wall case, only one instability is present, corresponding to mode II.

Firstly, consider the KE norm. In the heated wall case (panel 6.3a) the optimal condition is not observed for stationary waves, but rather for $\omega = 0.003$, indicating an interplay between the Orr and lift-up mechanisms. The optimum energy amplification, at $G_{\text{opt}} = 3160$, is lower compared to the sub- and supercritical regimes, reaching only 60% to 70% of the energy growth observed in those regimes. As for the cooled wall scenario (panel 6.3b), the global maximum occurs for oblique stationary waves, with energy growth being driven by the lift-up mechanism. In this case, the energy amplification at $G_{\text{opt}} = 8990$ is significantly higher than in the sub- and supercritical regimes, showing an increase of 70% to 100%.

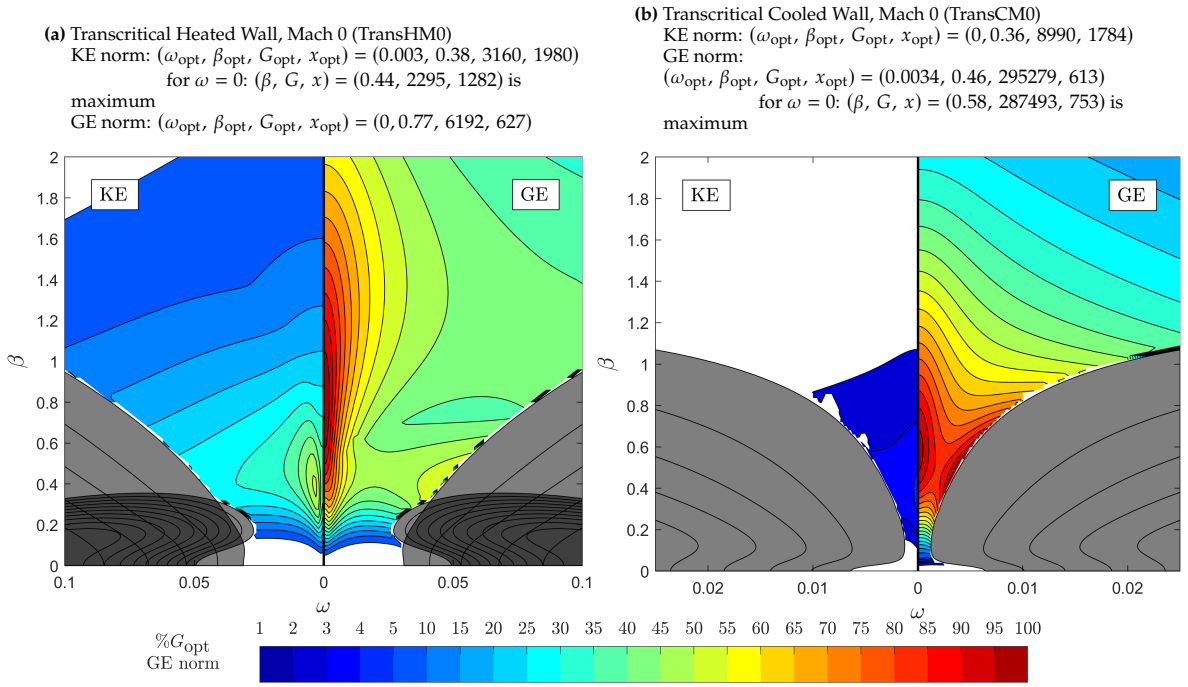

Figure 6.3: Contours of maximum spatial energy amplification (G_{max}) with varying stream-wise and span-wise wave number. The Reynolds number is $Re_\delta = 1000$. The considered boundary layers are the cases TransHM0 and TransCM0 in panels 6.3a and 6.3b, respectively.

Regarding the GE energy norm, in the heated wall case the global maximum is observed for oblique stationary wave: energy amplification due to the lift-up effect. The optimal initial and resulting disturbances are plotted in Figure 6.4a. Unlike in the sub- and supercritical regimes, the resulting disturbance features large temperature and density components. These have a maximum at the pseudo-boiling point where the respective base flow gradients are maximum. The streamwise velocity streak in the resulting disturbance has a noticeable decrease in the proximity of the Widom point. The optimum energy amplification is 3 times higher when compared to the maximum obtained using the KE norm. This is mostly due to the non-kinetic terms of Equation 2.51: for the optimal resulting disturbance, the kinetic terms only contain 25% of the total energy.

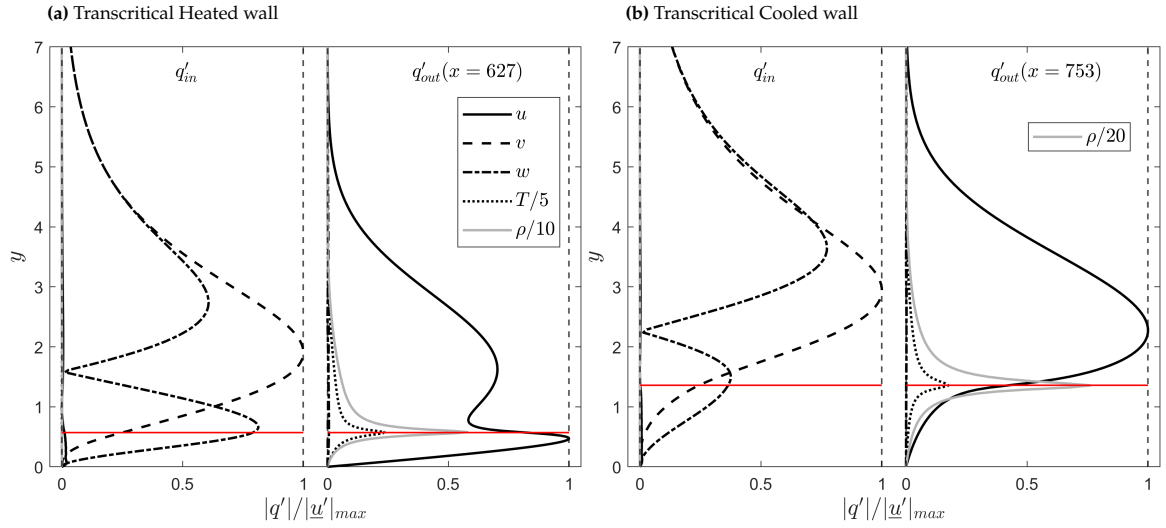

Figure 6.4: Optimal stationary ($\omega = 0$) disturbances corresponding to Figure 6.3

In the TransHM0 GE norm case, a second local maximum is observed near mode I and mode II neutral curves. At this condition, in the initial disturbance the (nearly) neutral modes A and B interact destructively with highly damped eigenfunctions from the continuous vorticity/entropy spectrum. As x increases, the highly damped continuous modes decay and only the slowly-decaying modes I and II remain, resulting in transient energy growth. This mechanism is also observed for ideal gas boundary layers (Bitter & Shepherd, 2014), although in the present the process is unique due to the presence of two slow-decaying discrete modes: mode II in addition to the TS mode (mode I). In the case of slowly-decaying mode I and II, due to their non-orthogonality, the perturbation energy oscillates with increasing x. Consider the case where both mode I and mode II are neutral (with the remaining modes damped). At $x \to \infty$ only the two neutral modes remain, and the distarbance is

$$q'|_{x\to\infty} = \left(\kappa_I \tilde{q}_I \exp\{i\alpha_I x\} + \kappa_{II}\tilde{q}_{II}\exp\{i\alpha_{II}x\}\right)\exp\{(i(\beta z - \omega t))\} \tag{6.1}$$

where the subscripts I and II refer to mode I and mode II respectively, and κ are expansion coefficients. The energy of this disturbance is

$$\begin{aligned}\|q'|_{x\to\infty}\|_{\mathrm{E}} &= ||\kappa_I\tilde{q}_I\exp\{i\alpha_I x\} + \kappa_{II}\tilde{q}_{II}\exp\{i\alpha_{II}x\}||_{\mathrm{E}} = \\ &= \|\kappa_I\tilde{q}_I\|_{\mathrm{E}}^2 + \|\kappa_{II}\tilde{q}_{II}\|_{\mathrm{E}}^2 + 2\,\mathrm{Re}\left\{\left\langle\kappa_I\tilde{q}_I\exp\{i\alpha_I x\},\ \kappa_{II}\tilde{q}_{II}\exp\{i\alpha_{II}x\}\right\rangle_{\mathrm{E}}\right\} = \\ &= \|\kappa_I\tilde{q}_I\|_{\mathrm{E}}^2 + \|\kappa_{II}\tilde{q}_{II}\|_{\mathrm{E}}^2 + 2\,\mathrm{Re}\left\{\langle\kappa_I\tilde{q}_I,\ \kappa_{II}\tilde{q}_{II}\rangle_{\mathrm{E}}\exp\{i(\alpha_I-\alpha_{II})x\}\right\}\end{aligned} \tag{6.2}$$

which oscillates with period $2\pi/|\alpha_{II} - \alpha_I|$. The amplitude of these oscillations is

$$\max_x\left\{2\,\mathrm{Re}\left\{\langle\kappa_I\tilde{q}_I,\ \kappa_{II}\tilde{q}_{II}\rangle_{\mathrm{E}}\exp\{i(\alpha_I-\alpha_{II})x\}\right\}\right\} = 2\left\|\langle\kappa_I\tilde{q}_I,\ \kappa_{II}\tilde{q}_{II}\rangle_{\mathrm{E}}\right\|_2 \tag{6.3}$$

This is shown in Figure 6.5, where $(\beta, \omega) = (0.32, 0.041)$ is considered. At this condition $\alpha_I = 0.067$ and $\alpha_{II} = 0.11$. In panel 6.5a the evolution of the energy amplification $G(x)$ is shown in black, and in blue the energy amplification of the initial condition that obtains maximum energy amplification. For large x, two maximum are separated by a distance of $\Delta x = 144$, which equals $2\pi/|\alpha_{II} - \alpha_I|$. In panel 6.5b the initial condition is shown alongside the disturbance at the locations marked with crosses in panel 6.5a. At the energy minimum, mode I and mode II cancel out each other's temperature and density components at the Widom line, while at the energy maximums these perturbations are large. The large amplitude of the energy fluctuation is mostly due to the non-kinetic terms of Equation 2.51. When mode I and II are slightly damped, decaying oscillations with irregular periods are observed.

Regarding the cooled wall case (panel 6.3b), and considering the GE norm, a local maximum is observed for an oblique stationary wave: lift-up mechanism. The initial and resulting disturbances are plotted in Figure 6.4b. Similar to the heated wall case, there are large temperature and density streaks in the resulting disturbance, with a maximum at the pseudo-boiling point. In the cooled wall scenario, the kinetic terms contain an even smaller percentage of the total energy, around 2%. The optimal energy amplification when accounting for the non-kinetic terms is around 18 times higher when comparing to the KE norm. A second local maximum of $G_{\max}$ exists near the neutral curve of mode II, this being a global maximum. Just as in the TransHM0 case, in this region amplification is high due to destructive interactions between highly damped vorticity/entropy modes and a slowly-decaying mode II. This is shown in Figure 6.6, where in panel 6.6a the global eigenspectrum is shown where the 10 most relevant modes are highlighted with the blue marker, these can be identified as mode II and additional modes from the continuous spectrum. In panel 6.6b the initial and resulting disturbances are shown. It is observed that at the initial condition ($x = 0$) the interaction between mode II and the remaining modes result in small temperature and density perturbations. As x increases, the modes from the continuous

(a) Energy amplification $G(x)$ in black and $g(x)$ in blue - see Equations 2.38 and 2.40. For $g(x)$ the initial disturbance which attains maximum energy growth is considered.

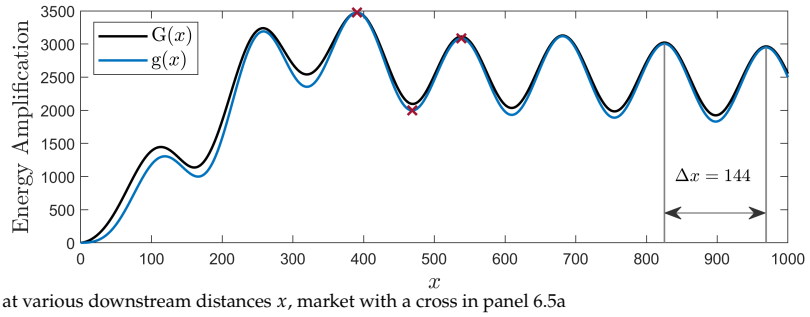

(b) Perturbation at various downstream distances x, market with a cross in panel 6.5a

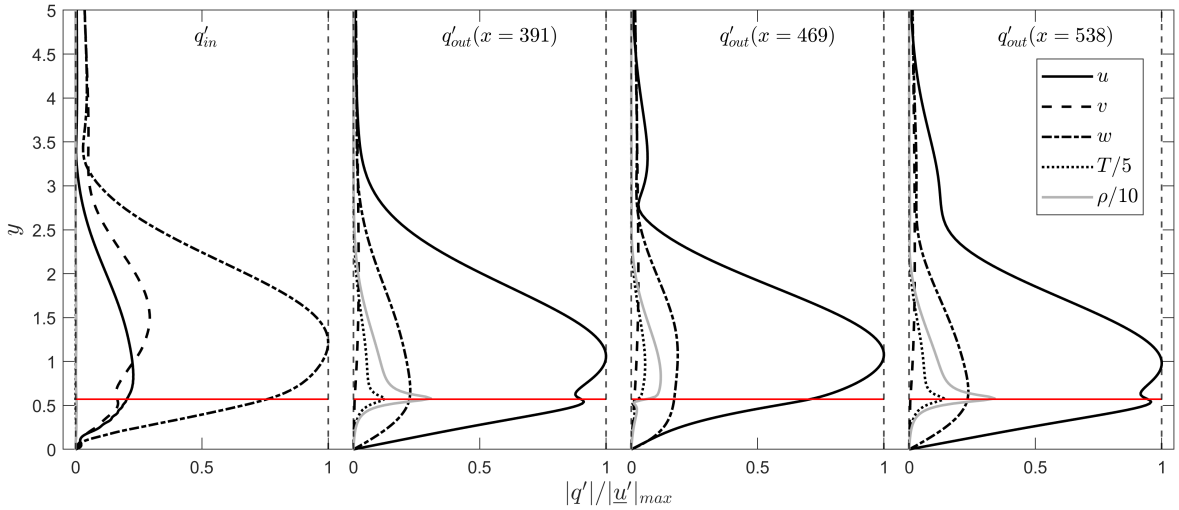

Figure 6.5: Energy growth oscillations due to non-orthogonality between mode I and II

spectrum quickly decay, resulting the large temperature and density perturbations, and ultimately, in energy growth.

(a) Global eigenspectrum. The black markers represent the global eigenspectrum, and the blue markers represent the 10 most relevant modes for the optimal disturbance – i.e. modes for which $|\kappa|$ is highest in Equation 2.36

(b) Optimal initial and resulting disturbances

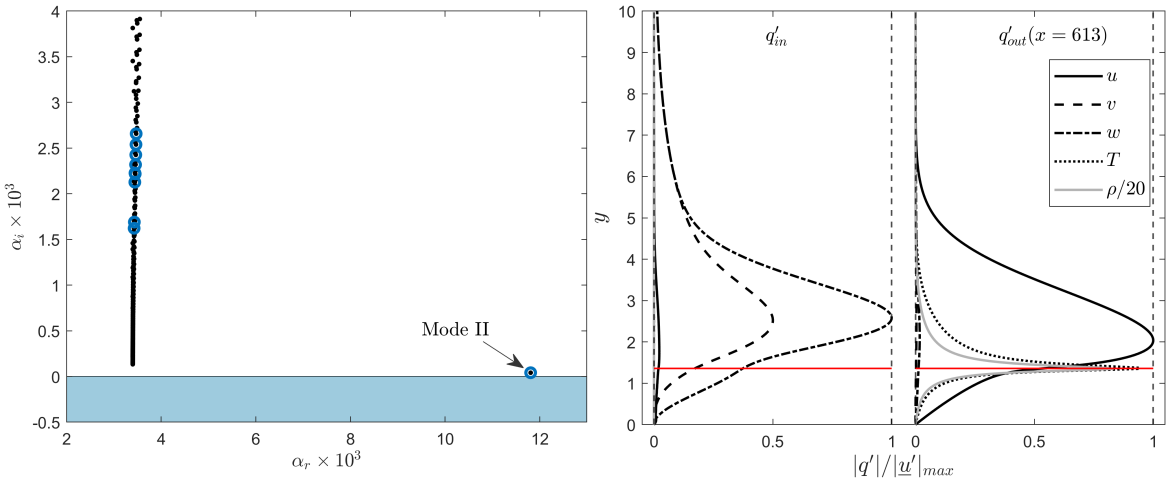

Figure 6.6: Energy growth due to the destructive interaction between a nearly neutral discrete mode (mode II) and highly damped vorticity/entropy modes from the continuous spectra

6.2.1. The Lift-up Effect in Transcritical Boundary layers

The kinetic energy amplification through the lift-up effect is most commonly explained by the redistribution of mean flow momentum in the wall normal direction. In the presence of a shear flow, vorticity streaks oriented in the stream-wise direction transport fast moving fluid from the outer region of the boundary layer towards the wall, and vice-versa, slow moving fluid near the wall is transported upwards. This originates stream-wise velocity streaks along the span-wise direction. Alternatively, one may interpret the origin of the stream-wise streaks as resulting from a tilting of the mean vorticity $-\partial U/\partial y$. Perturbation stream-wise vorticity tilts the mean vorticity along the stream-wise direction. This results in a perturbation vorticity oriented along the wall-normal direction, i.e. stream-wise velocity streaks.

In transcritical boundary layers, due to strong property stratification, particularly at the Widom line, the base flow velocity profile differs greatly when compared to an ideal gas boundary layer. As a result, the mean vorticity profile is also notably affected. The vorticity Ω is introduced:

$$\Omega = \nabla \times \underline{u} = \nabla \times \underline{\bar{u}} + \nabla \times \underline{u'} = \overline{\Omega} + \Omega' \tag{6.4}$$

where $\overline{\Omega}$ is the mean flow vorticity and Ω' the perturbation vorticity, given by

$$\overline{\Omega} = -\frac{\partial U}{\partial y}\vec{e_z} \tag{6.5a}$$

$$\Omega' = \left(\frac{\partial w'}{\partial y} - i\beta v'\right)\vec{e_x} + \left(i\beta u' - i\alpha w'\right)\vec{e_y} + \left(i\alpha v' - \frac{\partial u'}{\partial y}\right)\vec{e_z} \tag{6.5b}$$

Following the interpretation of the lift-up effect, the mean flow vorticity, optimal initial stream-wise perturbation vorticity and the resulting stream-wise perturbation velocity is looked at for the heated and cooled wall transcritical scenarios. As reference cases for comparison, two CO2 boundary layers, modelled as a calorically perfect gas (CPG) with a constant Prandtl number of Pr = 0.77 are also considered. One with a heated wall, where the temperature boundary conditions satisfy $T_\infty/T_{\text{wall}} = 0.95/1.05$. The other CO2 CPG boundary layer having a cooled wall where the temperature boundary condition is $T_\infty/T_{\text{wall}} = 1.05/0.95$. Note that these ratios are equal to the temperature boundary ratios in the SCO2 boundary layers. For each boundary layer, these being the heated and cooled CPG boundary layers and the TransHM0 and TransCM0 cases, the non-modal kinetic energy growth is optimized over β, considering $\omega = 0$. Figure 6.7 shows the mean flow vorticity, the initial stream-wise perturbation vorticity and the resulting stream-wise perturbation velocity for the heated (panel 6.7a) and cooled (panel 6.7b) cases. Note that, since the resulting optimal wall-normal and span-wise velocity perturbations are zero, the resulting span-wise vorticity perturbation is

$$\left(\Omega'_y\right)_{\text{out}} = (i\beta u') \tag{6.6}$$

such that $|\Omega'_y|/|\Omega'_y|_{\max} = |u'|/|u'|_{\max}$. Thus, Figure 6.7 shows the base flow span-wise vorticity, the initial stream-wise perturbation vorticity and the resulting wall-normal perturbation vorticity. Furthermore, Figure 6.8 shows the initial velocity perturbations in the y-z plane

In the CPG boundary layers, shown in Figure 6.7, the mean vorticity is maximum at the wall and slowly decreases with the distance from the wall. The initial perturbation vorticity has two maxima. The further from the wall corresponds with the centre of a vortex structure, while the near-wall stream-wise vorticity maximum is associated with the decay of the span-wise perturbation velocity. Close to the wall, where the wall-normal perturbation velocity is low, the local vorticity maximum is driven by the term $\frac{\partial w'}{\partial y}$ in Equation 6.5. Despite this near-wall maximum in stream-wise vorticity, the redistribution of

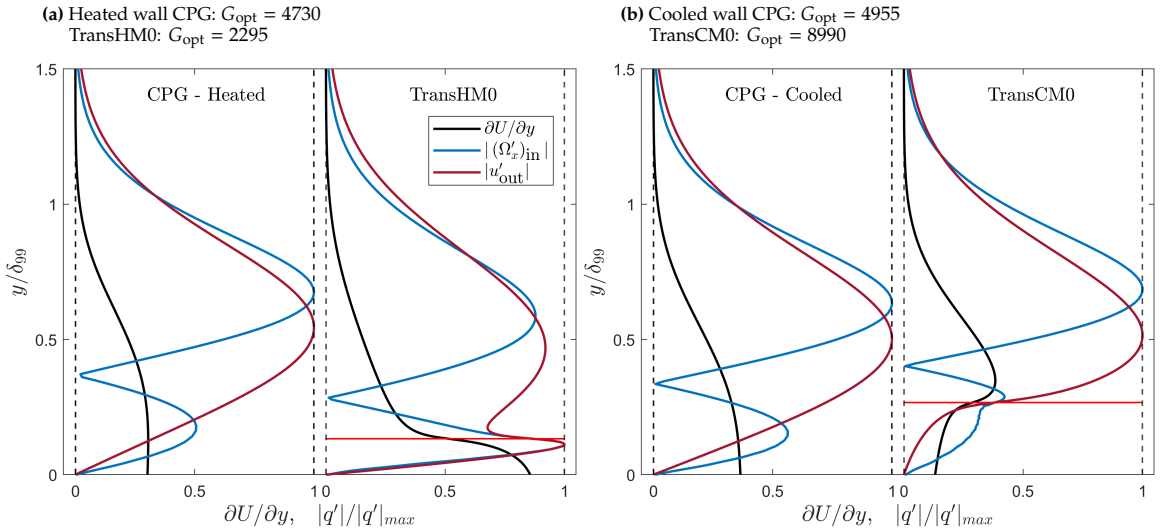

Figure 6.7: Mean span-wise vorticity, initial stream-wise vorticity perturbation and resulting wall-normal vorticity perturbation for the optimal stationary disturbance. The horizontal red line denotes the location of the Widom point. On the left, in panel 6.7a, a heated GCP CO2 boundary layer and the TransHM0 case, and on the right a cooled GCP CO2 boundary layer and the TransCM0 case

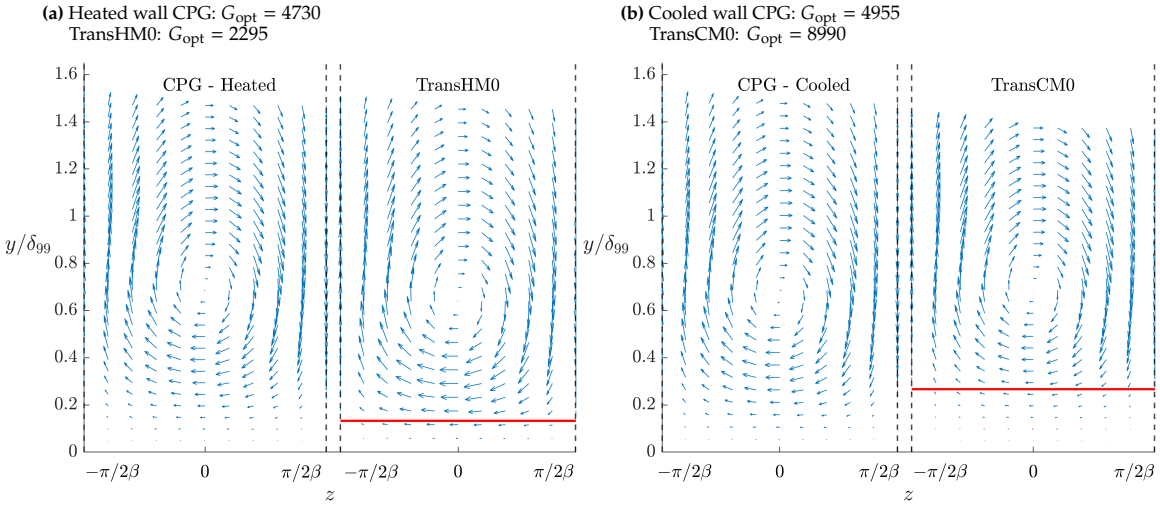

Figure 6.8: Initial velocity perturbation in the y-z plane for the optimal stationary disturbance. The horizontal red line denotes the location of the Widom point. On the left, in panel 6.8a, a heated GCP CO2 boundary layer and the TransHM0 case, and on the right, in panel 6.8b, a cooled GCP CO2 boundary layer and the TransCM0 case

mean flow momentum along the wall-normal direction is low. It is in fact the vortex structure associated with the vorticity maximum far from the wall that is responsible for the redistribution of mean flow momentum, or alternatively, the tilting of the mean vorticity, which in turn generates stream-wise velocity streaks. These conclusions are supported by the initial vortex structures plotted in Figure 6.8.

For the TransHM0 case, the mean vorticity has an abrupt decrease at the Widom line. It is low above the Widom point and high below it, having a maximum at the wall. The initial stream-wise perturbation vorticity has a maximum near the Widom line. However, this is linked to a sharp decrease of the span-wise perturbation velocity – the $\frac{\partial w'}{\partial y}$ term. In this region, while the mean flow vorticity is high, the perturbation wall-normal velocity component in low, indicating minimal wall-normal momentum redistribution. The vortex structure, responsible for the development of wall-normal vorticity, is located far from the wall, where the mean flow vorticity $-\partial U/\partial y$ is low. This results in a lower energy amplification when compared to the heated CPG case. Conversely, the TransCM0 case has

a maximum of mean vorticity above the Widom point, while below it $-\partial U/\partial y$ is relatively low. As the mean vorticity is high in a region far from the wall, where the wall-normal momentum redistribution is high, the resulting velocity streaks obtain a higher amplitude, resulting in higher energy amplification when compared to the CPG cooled wall case.

Near the Widom point, viscosity forces dominate the balance of stream-wise momentum (Bugeat et al., 2022). The approximation $\frac{\partial}{\partial y}\left(\mu\frac{\partial U}{\partial y}\right) \approx 0$ holds, from which $\frac{\partial}{\partial y}\log\left(\overline{\Omega}_z\right) \approx -\frac{\partial}{\partial y}\log(\overline{\mu})$. The derivative of the logarithm of the mean span-wise vorticity is approximately the derivative of the logarithm of the mean dynamic viscosity. Alternatively, near the Widom line:

$$\frac{\partial \log\left(\overline{\Omega}_z\right)}{\partial y} \approx -\frac{1}{\overline{\mu}}\frac{\partial \overline{T}}{\partial y}\left(\frac{\partial \overline{\mu}}{\partial T}\right)_{\overline{P}}. \tag{6.7}$$

The quantity $\left(\frac{\partial \mu}{\partial T}\right)_P$ is negative, and large at the Widom point. Hence, in the case of wall heating, $\partial T/\partial y < 0$, and there is a large decrease of mean stream-wise vorticity at the Widom point. In the case of wall cooling, $\partial T/\partial y > 0$ and a large increase in $\overline{\Omega}_z$ exists at the Widom point. With wall cooling, under $\partial U/\partial y < 0$, there is necessarily a local maximum of $\overline{\Omega}_z$ above the Widom line. Away from the wall, as $y \to \infty$, the mean vorticity is zero $\left(\overline{\Omega}_z|_{y\to\infty} = 0\right)$. Since the mean vorticity is positive at the Widom line and $\left(\partial\overline{\Omega}_z/\partial y\right)_w > 0$, there must exist a point at some $y > y_w$ where $\partial\overline{\Omega}_z/\partial y = 0$, corresponding to a maximum of $\overline{\Omega}_z$. The high mean span-wise vorticity far from the wall, present in the transcritical cooled wall case, results in a large energy amplification.

Lastly, the evolution of the production of kinetic energy with the wall-normal direction is looked at. The production of perturbation kinetic energy is recognized as the term

$$\mathrm{p}_K(x,y) = v'u^*\bar{\rho}\frac{\partial U}{\partial y} \tag{6.8}$$

The inner product $v'u^*$ is a function of the wall-normal and stream-wise direction. The stream-wise location which maximizes the total production $\mathrm{P}_K(x) = \int_{y=0}^{y\longrightarrow\infty}\mathrm{p}_K(x,y)dy$ is considered. That is, $\mathrm{p}_K(x_{\max\{P_K\}},y)$ is considered, where

$$x_{\max\{P_K\}} = \arg\max\ \mathrm{P}_K(x) \tag{6.9}$$

Figure 6.9 shows the evolution of the production of kinetic energy with the wall-normal direction, at $x = x_{\max\{P_K\}}$. The optimal stationary disturbance is considered, where panel 6.9a shows the heated wall cases, and in panel 6.9b the cooled wall cases.

In the heated wall cases (panel 6.9a), the production of kinetic energy is higher in the trancritical boundary layer near the wall, whereas higher in the CPG boundary layer far from the wall. This observation is in agreement with the analysis of Figure 6.7. Near the wall, the mean vorticity is higher for the trancritical boundary layer, resulting in a locally higher kinetic energy production, while the opposite is true far from the wall. Vice-versa, in the cooled wall cases (panel 6.9b), the production of kinetic energy is higher for the transcitical boundary layers far from the wall. This is linked to the comparatively higher mean vorticity in this region, while near the wall, both the mean vorticity and kinetic energy production are higher in the CPG boundary layer.

In transcritical boundary layers, wall cooling results in high mean vorticity away from the wall, which in turn leads to an increased energy growth. Conversely, in the heated wall case, mean vorticity is low far from the wall, leading to reduced energy growth. The distribution of mean vorticity is linked to the distribution of dynamic viscosity. Specifically, mean vorticity is high in the region where the

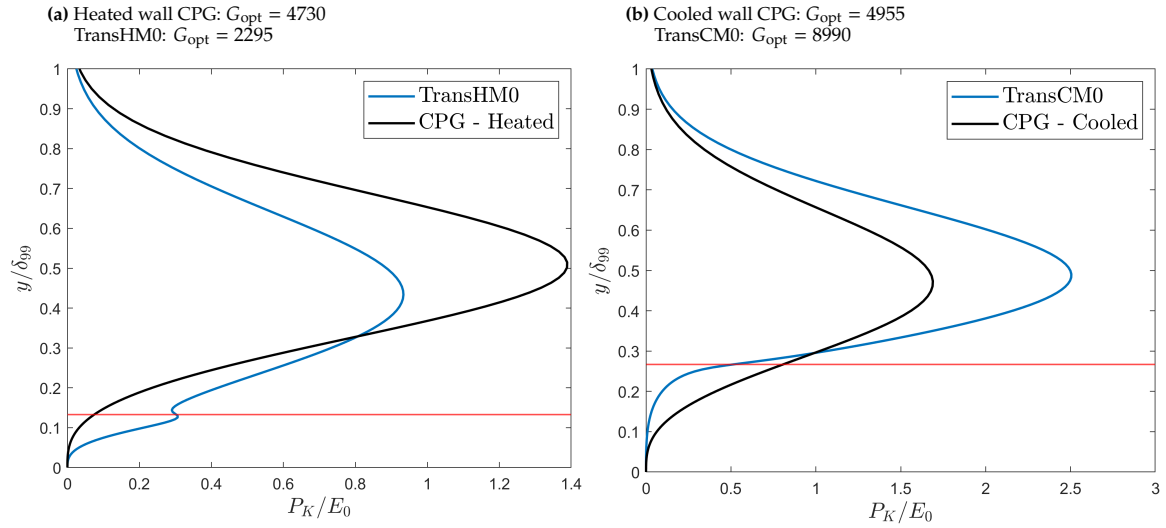

Figure 6.9: Evolution of the production of kinetic energy with the wall-normal direction, for the optimal stationary disturbance. The production term is normalized by the kinetic energy of the initial disturbance E_0. The horizontal red line denotes the location of the Widom point. On the left, in panel 6.9a, a heated GCP CO2 boundary layer and the TransHM0 case, and on the right, in panel 6.9b, a cooled GCP CO2 boundary layer and the TransCM0 case

dynamic viscosity is low, i.e. in the region where the fluid is gas-like. Additionally, in the case of wall cooling, it is shown that a local maximum of mean vorticity exists above the Widom line.

6.2.2. Influence of the location of the pseudo-boiling point

The influence of the location of the pseudo-boiling point on the non-modal perturbation energy growth is investigated. Various zero Mach boundary layers are considered and the location of the Widom line is controlled by changing the temperature boundary conditions at the wall and free stream. For the heated/cooled wall scenario, the stree-stream/wall temperature is varied between $0.9T_{pc}$ and T_{pc}, and the wall/free-stream temperature keeps the relation $|T_\infty - T_{\text{wall}}|/T_{pc} = 0.1$. Focus is placed on energy growth through the lift-up mechanism, and only stationary waves are considered ($\omega = 0$). For both the heated and cooled wall scenarios, the energy growth is optimized over β. Figure 6.10 shows the dependency of the optimum energy growth (G_{opt}) on the location of the Widom line. Only the kinetic energy growth is considered (KE norm). The location of the pseudo-boiling point (y_w) is scaled by the δ_{99} thickness of the boundary layer. The location of the Widom line of the TransHM0 and TransCM0 cases, with temperature boundary conditions of $T_\infty = 0.95T_{\text{pc}}$ and $T_\infty = 1.05T_{\text{pc}}$ respectively, are marked with the vertical lines. Two additional x-axis are provided, one with the free-stream temperature (T_∞) for the heated wall case, and one with the free-stream temperature for the cooled wall case.

The kinetic energy amplification in the heated wall cases is always lower than in the reference CPG cases introduced in Figure 6.7. As discussed, in the heated wall case, the mean vorticity features a noticeable decrease at the location of the Widom line, which in turn results in perturbation wall-normal vorticity of lesser amplitude. The opposite is true for the cooled wall case, where the mean vorticity in high above the Widom line, in a region far from the wall. This results in a higher amplitude of the resulting stream-wise velocity streaks, such that the energy amplification is always higher when compared to the reference CPG case. For the cooled wall case, the kinetic energy amplification is maximum for $y_w/\delta_{99} \sim 0.35$. This can be linked to a maximum of mean vorticity, as shown in Figure 6.11. Indeed, it is observed that the maximum of the mean vorticity ($\partial U/\partial y$) is maximum for $y_w/\delta_{99} \sim 0.35$.

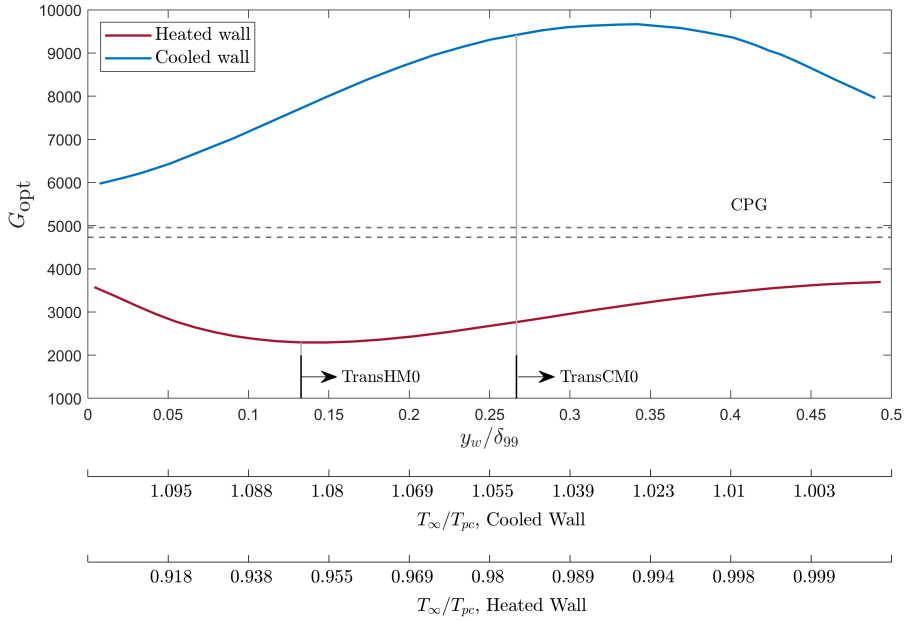

Figure 6.10: Dependency of the optimal kinetic energy growth at $\omega = 0$ with the location of the pseudo-boiling point. Zero Mach number boundary layers are considered with varying temperature boundary conditions, which keep the relation $|T_\infty - T_{\text{wall}}|/T_{pc} = 0.1$. In red the wall is heated ($T_{\text{wall}} = T_\infty + 0.1$) while in blue the wall is cooled. The vertical lines represent the location of the Widom line for the TransHM0 and TransCM0 cases. The horizontal lines represent the optimal kinetic energy growth of the two CPG boundary layers in Figure 6.7. Two additional x-axis are provided, with the free-stream temperature for the cooled and heated wall cases

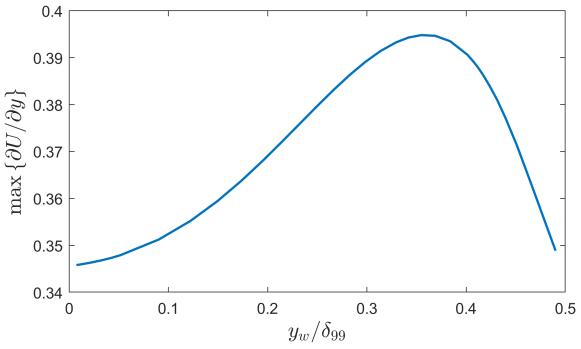

Figure 6.11: Dependency of the mean span-wise vorticity ($\partial U/\partial y$) with the location of the Widom point, for the transcritical cooled wall case.

7

Conclusion

The first main objective of this thesis is to investigate the modal growth of oblique waves. Section 5.1 investigated the amplification of oblique waves in the sub- and supercritical regimes. In agreement with the current literature (Gloerfelt et al., 2020, Mack, 1984, Ren et al., 2019b), mode I (TS mode) is found to be preferentially 3D for sufficiently high Mach number, around $M_\infty > 0.8$. While the phase speed c_x increases with the wave number β, for the cases where mode I is preferentially 3D, an initial decrease of the phase speed c_x is observed before its increase for high β. In the heated wall transcritical regime, addressed in Section 5.2, mode I, whose critical layer (y_c) is above the Widom point (y_w), is found to be preferentially 2D. Conversely, mode II, whose critical layer is below the Widom point, is preferentially 3D for sufficiently high Mach number, around $M_\infty > 0.7$. The increase of the growth rate with β is, similar to the sub- and supercritical regimes, linked to the initial decrease of the phase speed c_x. In the cooled wall transcritical case, for low Reynolds number the critical layer of mode II is above the Widom point, this results in the crossing of the critical layer over the Widom point for high β. Thus, for the cooled wall case, in the viscous regime, the phase speed c_x of mode II decreases with the wave number β. Still, for high Mach number, mode II is preferentially 3D, and the phase speed c_x initially increases with β before its decrease for high β. Thus, a link is made between the evolution of c_x with β and the further amplification of 3D waves.

This link between the phase speed c_x and the further amplification of 3D waves is confirmed in the inviscid regime, in Section 5.3, where only mode II is present in the transcritical cases. The total derivative of the complex phase speed c_x with respect to $\lambda = \beta^2$ is

$$\frac{\mathrm{d}c_x}{\mathrm{d}\lambda} = \frac{\int_0^{y_2} \frac{\partial}{\partial y}\left(\rho\tilde{v}\frac{\partial\tilde{v}_\lambda}{\partial y} - \rho\tilde{v}_\lambda\frac{\partial\tilde{v}}{\partial y}\right)dy + \int_o^{y_2} \xi\frac{\partial}{\partial\lambda}\left(\frac{\xi^{(1)}}{\xi}\right)\tilde{v}\frac{\partial\tilde{v}}{\partial y}dy + \int_0^{y_2} -\xi\frac{\partial}{\partial\lambda}\left(\psi + \frac{\zeta}{\xi}\right)\tilde{v}^2 dy}{\int_0^{y_2} -\xi\frac{\partial}{\partial c_x}\left(\frac{\xi^{(1)}}{\xi}\right)\tilde{v}\frac{\partial\tilde{v}}{\partial y}dy + \int_0^{y_2} \xi\frac{\partial}{\partial c_x}\left(\psi + \frac{\zeta}{\xi}\right)\tilde{v}^2 dy} \qquad \text{(5.10 revisited)}$$

where the temporal approach is adopted, as it is found to facilitate the analysis. For the (non-trivial) 2D neutral inviscid wave, $c_x = U_s$, and $\alpha = \alpha_s$, the numerator is real and the denominator complex. It is shown that, in the case of the neutral inviscid wave, the further amplification of 3D waves is due to the change of sign of the numerator of Equation 5.10, which reads

$$\int_0^{y_2} -\xi\tilde{v}^2 dy + \int_0^{y_2} \frac{\xi\{M_r^2\}^{(1)}}{(\alpha^2+\beta^2)(1-M_r^2)^2}\left(\frac{U^{(1)}}{U-c_x}\tilde{v}^2 - \tilde{v}\tilde{v}^{(1)}\right)dy. \qquad \text{(5.24 revisited)}$$

The leftmost integral is negative, and the rightmost is positive. For zero-Mach number the rightmost integral is zero, thus, the numerator is negative and the inviscid wave with $\alpha = \alpha_s$ is damped for

$\beta > 0$. For sufficiently large Mach the numerator is positive due to the contribution of the rightmost integral, and the inviscid wave is amplified for $\alpha = \alpha_s$ and $\beta > 0$. Furthermore, the change of sign of the numerator also justifies the change in the evolution of the real part of c_x with β, as observed not only in the inviscid mode II, but also in the viscous regime and also in the viscous TS mode (Figure 5.3b).

The second main objective of this thesis is to investigate the non-modal energy growth of transcritical boundary layers. Section 6.1 considered both the sub- and supercritical boundary layers at zero-Mach number. It is found that the energy growth is these boundary layers is similar to that observed in ideal gas boundary layers. The optimal energy growth is obtained for oblique stationary waves – energy growth through the lift-up mechanism. Furthermore, energy growth is in great part attributed to kinetic effects. In the case of the transcritical boundary layers, explored in Section 6.2, optimal energy growth is found to also be associated with the lift-up mechanism. However, in these cases the non-kinetic terms contribute considerably to the energy makeup of the resulting optimal disturbances. Moreover, mode I (TS) and mode II are found to be non-orthogonal resulting in energy oscillations at a frequency and span-wise wave-number near their neutral curves. Lastly, in the case of the kinetic energy growth, the modulation of the mean span-wise vorticity is attributed to the large kinetic energy growth observed in the cooled wall transcritical case, and comparatively low kinetic energy growth for a heated wall. Indeed, for a cooled wall trancritical boundary layer, due to the large decrease in viscosity with the wall-normal direction, a maximum of mean vorticity is observed at a region far from the wall, which results in large kinetic energy amplification.

7.1. Discussion and Further Research

In Chapter 5 the modal stability of the considered boundary-layers was investigated. Here, a link is made between the Mach number and the further amplification of 3D waves, when compared to their 2D counterpart. Within the inviscid approximation an analytical expression for the first order derivative of c_x with respect to β is obtained. However, the analysis of this equation is limited to the neutral inviscid wave. In this case, for the inviscid wave with $c_x = U_s$ and $\alpha = \alpha_s$, a greater-than-zero Mach is necessary for the further amplification of $\beta > 0$, $\alpha = \alpha_s$ waves. It is observed that in the case of mode II, a slow wave whose critical layer is below the GIP, 3D waves are more amplified than at $\beta = 0$. However, in the case of Mack's second mode, it is observed that fast waves, whose critical layer is above the GIP, are less amplified for increasing β. Firstly, a more detailed analysis of Macks' second mode, and a comparison between it and mode II, could bring clarity as to the mechanism responsible for the further amplification of 3D inviscid waves. Moreover, the analysis of Equation 5.10 could be extended to amplified waves in order to better understand the influence of the location of the critical layer (or equivalently, the speed of the wave) in the further amplification of 3D waves. Finally, an interpretation of the terms in Equation 5.24, could also bring some clarity into the mechanism at play.

With regards to the non-modal stability analysis. The present study is restricted to zero Mach number. In this case the transcritical regime can be obtained by considering a cooled or heated wall, as opposed to an adiabatic wall. However, this approach makes the choice of an energy norm more challenging, as Chu's energy norm is no longer bounded. The present study can be extended to finite Mach number with an adiabatic wall. In this case, Chu's energy norm is bounded and offers a physically meaningful energy norm which includes non-kinetic terms.

Appendices

A

The Stability Equations

Regarding the linear problem in equation 2.19:

$$\mathcal{L}_t \frac{\partial q'}{\partial t} + \mathcal{L}_x \frac{\partial q'}{\partial x} + \mathcal{L}_y \frac{\partial q'}{\partial y} + \mathcal{L}_z \frac{\partial q'}{\partial z} + \mathcal{L}_{q'} q' + \\ + \mathcal{L}_{xx} \frac{\partial^2 q'}{\partial x^2} + \mathcal{L}_{yy} \frac{\partial^2 q'}{\partial y^2} + \mathcal{L}_{zz} \frac{\partial^2 q'}{\partial z^2} + \mathcal{L}_{xy} \frac{\partial^2 q'}{\partial x \partial y} + \mathcal{L}_{xz} \frac{\partial^2 q'}{\partial x \partial z} + \mathcal{L}_{yz} \frac{\partial^2 q'}{\partial y \partial z} = 0 \quad \text{(2.19 revisited)}$$

the matrices are 5×5, and their non-zero elements are

$$\begin{gathered} \mathcal{L}_t(1,1) = \left(\frac{\partial \rho}{\partial p}\right)_T \qquad \mathcal{L}_t(1,5) = \left(\frac{\partial \rho}{\partial T}\right)_p \\ \mathcal{L}_t(2,2) = \mathcal{L}_t(3,3) = \mathcal{L}_t(4,4) = \rho \\ \mathcal{L}_t(5,1) = \rho \left(\frac{\partial e}{\partial p}\right)_T \qquad \mathcal{L}_t(5,5) = \rho \left(\frac{\partial e}{\partial T}\right)_p \end{gathered} \tag{A.1}$$

$$\begin{gathered} \mathcal{L}_x(1,1) = U \left(\frac{\partial \rho}{\partial p}\right)_T \qquad \mathcal{L}_x(1,2) = \rho \qquad \mathcal{L}_x(1,5) = U \left(\frac{\partial \rho}{\partial T}\right)_p \\ \mathcal{L}_x(2,1) = \frac{1}{\mathrm{M}_\infty^2} \qquad \mathcal{L}_x(2,2) = \rho U \qquad \mathcal{L}_x(2,3) = -\frac{1}{\mathrm{Re}_\delta} \frac{\partial \mu}{\partial y} \\ \mathcal{L}_x(3,1) = -\frac{1}{\mathrm{Re}_\delta} \left(\frac{\partial \mu}{\partial p}\right)_T \frac{\partial U}{\partial y} \qquad \mathcal{L}_x(3,2) = \frac{2}{3} \frac{\partial \mu}{\partial y} \qquad \mathcal{L}_x(3,3) = \rho U \\ \mathcal{L}_x(3,5) = -\frac{1}{\mathrm{Re}_\delta} \left(\frac{\partial \mu}{\partial T}\right)_p \frac{\partial U}{\partial y} \\ \mathcal{L}_x(4,4) = \rho U \\ \mathcal{L}_x(5,1) = \rho U \left(\frac{\partial e}{\partial p}\right)_T \qquad \mathcal{L}_x(5,2) = \frac{\mathrm{Ec}}{\mathrm{M}_\infty^2} p \qquad \mathcal{L}_x(5,3) = -2\mu \frac{\mathrm{Ec}}{\mathrm{Re}_\delta} \frac{\partial U}{\partial y} \\ \mathcal{L}_x(5,5) = \rho U \left(\frac{\partial e}{\partial T}\right)_p \end{gathered} \tag{A.2}$$

$$
\begin{gathered}
\mathcal{L}_y(1,3) = \rho \\
\mathcal{L}_y(2,1) = -\frac{1}{\mathrm{Re}_\delta}\left(\frac{\partial \mu}{\partial p}\right)_T \frac{\partial U}{\partial y} \qquad \mathcal{L}_y(2,2) = -\frac{1}{\mathrm{Re}_\delta}\frac{\partial \mu}{\partial y} \qquad \mathcal{L}_y(2,5) = -\frac{1}{\mathrm{Re}_\delta}\left(\frac{\partial \mu}{\partial T}\right)_p \frac{\partial U}{\partial y} \\
\mathcal{L}_y(3,1) = \frac{1}{\mathrm{M}_\infty^2} \qquad \mathcal{L}_y(3,3) = -2\frac{1}{\mathrm{Re}_\delta}\frac{\partial \mu}{\partial y} + \frac{2}{3}\frac{1}{\mathrm{Re}_\delta}\frac{\partial \mu}{\partial y} \\
\mathcal{L}_y(4,4) = -\frac{1}{\mathrm{Re}_\delta}\frac{\partial \mu}{\partial y} \\
\mathcal{L}_y(5,1) = -\frac{1}{\mathrm{Re}_\delta \mathrm{Pr}}\left(\frac{\partial \kappa}{\partial p}\right)_T \frac{\partial T}{\partial y} \qquad \mathcal{L}_y(5,2) = -2\mu\frac{\mathrm{Ec}}{\mathrm{Re}_\delta}\frac{\partial U}{\partial y} \qquad \mathcal{L}_y(5,3) = \frac{\mathrm{Ec}}{\mathrm{M}_\infty^2} p \\
\mathcal{L}_y(5,5) = -\frac{1}{\mathrm{Re}_\delta \mathrm{Pr}}\left(\frac{\partial \kappa}{\partial y} + \left(\frac{\partial \kappa}{\partial T}\right)_p \frac{\partial T}{\partial y}\right)
\end{gathered}
\tag{A.3}
$$

$$
\begin{gathered}
\mathcal{L}_z(1,4) = \rho \\
\mathcal{L}_z(3,4) = \frac{2}{3}\frac{\partial \mu}{\partial y}\frac{1}{\mathrm{Re}_\delta} \\
\mathcal{L}_z(4,1) = \frac{1}{\mathrm{M}_\infty^2} \qquad \mathcal{L}_z(4,3) = -\frac{\partial \mu}{\partial y}\frac{1}{\mathrm{Re}_\delta} \\
\mathcal{L}_z(5,4) = \frac{\mathrm{Ec}_\infty}{\mathrm{M}_\infty^2} p
\end{gathered}
\tag{A.4}
$$

$$
\begin{gathered}
\mathcal{L}_{q'}(1,3) = \frac{\partial \rho}{\partial y} \\
\mathcal{L}_{q'}(2,1) = -\left(\frac{\partial \mu}{\partial p}\right)_T \frac{\partial^2 U}{\partial y y^2}\frac{1}{\mathrm{Re}_\delta} - \frac{\partial U}{\partial y}\frac{1}{\mathrm{Re}_\delta}\left(\left(\frac{\partial^2 \mu}{\partial p^2}\right)_T \frac{\partial p}{\partial y} + \frac{\partial^2 \mu}{\partial T \partial p}\frac{\partial T}{\partial y}\right) \\
\mathcal{L}_{q'}(2,3) = \rho\frac{\partial U}{\partial y} \mathcal{L}_{q'}(2,5) = -\frac{1}{\mathrm{Re}_\delta}\left(\frac{\partial \mu}{\partial T}\right)_p \frac{\partial^2 U}{\partial y^2} - \frac{1}{\mathrm{Re}_\delta}\frac{\partial U}{\partial y}\left(\left(\frac{\partial^2 \mu}{\partial T^2}\right)_p \frac{\partial T}{\partial y} + \frac{\partial^2 \mu}{\partial T \partial p}\frac{\partial P}{\partial y}\right) \\
\mathcal{L}_{q'}(5,1) = -\frac{1}{\mathrm{Re}_\delta \mathrm{Pr}}\left(\frac{\partial^2 T}{\partial y^2}\left(\frac{\partial \kappa}{\partial p}\right)_T + \frac{\partial T}{\partial y}\left(\left(\frac{\partial^2 \kappa}{\partial p^2}\right)_T \frac{\partial p}{\partial y} + \frac{\partial^2 \kappa}{\partial T \partial p}\frac{\partial T}{\partial y}\right)\right) - \frac{\mathrm{Ec}}{\mathrm{Re}_\delta}\left(\frac{\partial \mu}{\partial p}\right)_T \left(\frac{\partial U}{\partial y}\right)^2 \\
\mathcal{L}_{q'}(5,3) = \rho\frac{\partial e}{\partial y} \\
\mathcal{L}_{q'}(5,5) = -\frac{1}{\mathrm{Re}_\delta \mathrm{Pr}}\left(\frac{\partial^2 T}{\partial y^2}\left(\frac{\partial \kappa}{\partial T}\right)_p + \frac{\partial T}{\partial y}\left(\left(\frac{\partial^2 \kappa}{\partial T^2}\right)_p \frac{\partial T}{\partial y} + \frac{\partial^2 \kappa}{\partial T \partial p}\frac{\partial p}{\partial y}\right)\right) - \frac{\mathrm{Ec}}{\mathrm{Re}_\delta}\left(\frac{\partial \mu}{\partial T}\right)_p \left(\frac{\partial U}{\partial y}\right)^2
\end{gathered}
\tag{A.5}
$$

$$\begin{aligned}
\mathcal{L}_{xx}(2,2) &= -\frac{4}{3}\frac{\mu}{\mathrm{Re}_\delta} \\
\mathcal{L}_{xx}(3,3) &= -\frac{\mu}{\mathrm{Re}_\delta} \\
\mathcal{L}_{xx}(4,4) &= -\frac{\mu}{\mathrm{Re}_\delta} \\
\mathcal{L}_{xx}(5,5) &= -\kappa\frac{1}{\mathrm{Re}_\delta \mathrm{Pr}}
\end{aligned} \tag{A.6}$$

$$\begin{aligned}
\mathcal{L}_{yy}(2,2) &= -\frac{\mu}{\mathrm{Re}_\delta} \\
\mathcal{L}_{yy}(3,3) &= -\frac{4}{3}\frac{\mu}{\mathrm{Re}_\delta} \\
\mathcal{L}_{yy}(4,4) &= -\frac{\mu}{\mathrm{Re}_\delta} \\
\mathcal{L}_{yy}(5,5) &= -\kappa\frac{1}{\mathrm{Re}_\delta \mathrm{Pr}}
\end{aligned} \tag{A.7}$$

$$\begin{aligned}
\mathcal{L}_{zz}(2,2) &= -\frac{\mu}{\mathrm{Re}_\delta} \\
\mathcal{L}_{zz}(3,3) &= -\frac{\mu}{\mathrm{Re}_\delta} \\
\mathcal{L}_{zz}(4,4) &= -\frac{4}{3}\frac{\mu}{\mathrm{Re}_\delta} \\
\mathcal{L}_{zz}(5,5) &= -\kappa\frac{1}{\mathrm{Re}_\delta \mathrm{Pr}}
\end{aligned} \tag{A.8}$$

$$\begin{aligned}
\mathcal{L}_{xy}(2,3) &= -\frac{1}{3}\frac{\mu}{\mathrm{Re}_\delta} \\
\mathcal{L}_{xy}(3,2) &= -\frac{1}{3}\frac{\mu}{\mathrm{Re}_\delta}
\end{aligned} \tag{A.9}$$

$$\begin{aligned}
\mathcal{L}_{xz}(2,4) &= -\frac{1}{3}\frac{\mu}{\mathrm{Re}_\delta} \\
\mathcal{L}_{xz}(4,2) &= -\frac{1}{3}\frac{\mu}{\mathrm{Re}_\delta}
\end{aligned} \tag{A.10}$$

$$\begin{aligned}\mathcal{L}_{yz}(3,4) &= -\frac{1}{3}\frac{\mu}{\mathrm{Re}_\delta}\\ \mathcal{L}_{yz}(4,3) &= -\frac{1}{3}\frac{\mu}{\mathrm{Re}_\delta}\end{aligned} \tag{A.11}$$

As for the inviscid equation

$$\left(\alpha^2\mathcal{A}^{\mathrm{INV}}_{\alpha^2} + \omega^2\mathcal{A}^{\mathrm{INV}}_{\omega^2} + \alpha\omega\mathcal{A}^{\mathrm{INV}}_{(\alpha\omega)} + \alpha\mathcal{A}^{\mathrm{INV}}_{\alpha} + \omega\mathcal{A}^{\mathrm{INV}}_{\omega} + \mathcal{A}_0\right)\tilde{q} = 0 \tag{2.23 revisited}$$

the equations are 2×2 and their non-zero elements

$$\mathcal{A}^{\mathrm{INV}}_{\alpha^2}(2,1) = \frac{U^2}{a^2} - \frac{1}{\mathrm{M}_\infty^2} \tag{A.12}$$

$$\begin{aligned}\mathcal{A}^{\mathrm{INV}}_{\alpha}(1,2) &= i\rho U\\ \mathcal{A}^{\mathrm{INV}}_{\alpha}(2,2) &= -i\rho U\left(\frac{\partial}{\partial y} + \frac{\partial U}{\partial y}\right)\end{aligned} \tag{A.13}$$

$$\mathcal{A}^{\mathrm{INV}}_{\alpha\omega}(2,1) = -2\frac{U}{a^2} \tag{A.14}$$

$$\mathcal{A}^{\mathrm{INV}}_{\omega^2}(2,1) = \frac{1}{a^2} \tag{A.15}$$

$$\begin{aligned}\mathcal{A}^{\mathrm{INV}}_{\omega}(1,2) &= -i\rho\\ \mathcal{A}^{\mathrm{INV}}_{\omega}(2,2) &= -i\rho\frac{\partial}{\partial y}\end{aligned} \tag{A.16}$$

$$\begin{aligned}\mathcal{A}^{\mathrm{INV}}_{0}(1,1) &= \frac{1}{\mathrm{M}_\infty^2}\frac{\partial}{\partial y}\\ \mathcal{A}^{\mathrm{INV}}_{0}(2,1) &= \frac{\beta^2}{\mathrm{M}_\infty^2}\end{aligned} \tag{A.17}$$

Bibliography

Anderson, J. D. (1989). *Hypersonic and high temperature gas dynamics*. Aiaa.

Bitter, N., & Shepherd, J. (2014). Transient growth in hypersonic boundary layers. *7th AIAA theoretical fluid mechanics conference*, 2497.

Bugeat, B., Boldini, P. C., & Pecnik, R. (2022). On the new unstable mode in the boundary layer flow of supercritical fluids. *12th International Symposium on Turbulence and Shear Flow Phenomena (TSFP12) Osaka, Japan*.

Ellingsen, T., & Palm, E. (1975). Stability of linear flow. *The Physics of Fluids*, *18*(4), 487–488.

Fedorov, A., & Tumin, A. (2011). High-speed boundary-layer instability: Old terminology and a new framework. *AIAA journal*, *49*(8), 1647–1657.

Gloerfelt, X., Robinet, J.-C., Sciacovelli, L., Cinnella, P., & Grasso, F. (2020). Dense-gas effects on compressible boundary-layer stability. *Journal of Fluid Mechanics*, *893*.

Govindarajan, R., & Sahu, K. C. (2014). Instabilities in viscosity-stratified flow. *Annual Review of Fluid Mechanics*, *46*(1), 331–353.

Gustavsson, L. H. (1991). Energy growth of three-dimensional disturbances in plane poiseuille flow. *Journal of Fluid Mechanics*, *224*, 241–260.

Hanifi, A., Schmid, P. J., & Henningson, D. S. (1996). Transient growth in compressible boundary layer flow. *Physics of Fluids*, *8*(3), 826–837.

Henningson, D. S., Lundbladh, A., & Johansson, A. V. (1993). A mechanism for bypass transition from localized disturbances in wall-bounded shear flows. *Journal of Fluid Mechanics*, *250*, 169–207.

Hudson, M. L., Chokani, N., & Candler, G. V. (1997). Linear stability of hypersonic flow in thermochemical nonequilibrium. *AIAA journal*, *35*(6), 958–964.

Joseph, D. D., Bai, R., Chen, K. P., Renardy, Y. Y., et al. (1997). Core-annular flows. *Annual Review of Fluid Mechanics*, *29*(1), 65–90.

Joseph, D. D., Renardy, M., & Renardy, Y. (1984). Instability of the flow of two immiscible liquids with different viscosities in a pipe. *Journal of Fluid Mechanics*, *141*, 309–317.

King, J., & Williams, L. (2003). Utilization of critical fluids in processing semiconductors and their related materials. *Current Opinion in Solid State and Materials Science*, *7*(4-5), 413–424.

Landahl, M. (1980). A note on an algebraic instability of inviscid parallel shear flows. *Journal of Fluid Mechanics*, *98*(2), 243–251.

Lees, L., & Lin, C.-C. (1946). *Investigation of the stability of the laminar boundary layer in a compressible fluid*. National Advisory Committee for Aeronautics.

Lemmon, E. W., Bell, I. H., Huber, M. L., & McLinden, M. O. (2018). NIST Standard Reference Database 23: Reference Fluid Thermodynamic and Transport Properties-REFPROP, Version 10.0, National Institute of Standards and Technology. https://doi.org/https://doi.org/10.18434/T4/1502528

Lysenko, V. I., & Maslov, A. A. (1984). The effect of cooling on supersonic boundary-layer stability. *Journal of Fluid Mechanics*, *147*, 39–52.

Mack, L. M. (1963). The inviscid stability of the compressible laminar boundary layer. *Space Programs Summary*, *37*, 23.

Mack, L. M. (1964). The inviscid stability of the compressible laminar boundary layer: Part ii. *Space Programs Summary*, *4*, 165.

Mack, L. M. (1965). The stability of the compressible laminar boundary layer according to a direct numerical solution. *AGARDograph*, *97*, 329–362.

Mack, L. M. (1984). *Boundary-layer linear stability theory* (tech. rep.). California Institute of Technology Pasadena Jet Propulsion Laboratory.

Malik, M., & Anderson, E. (1991). Real gas effects on hypersonic boundary-layer stability. *Physics of Fluids A: Fluid Dynamics*, *3*(5), 803–821.

Malik, M. R. (1990). Numerical methods for hypersonic boundary layer stability. *Journal of computational physics*, *86*(2), 376–413.

Morkovin, M. V. (1969). *Critical evaluation of transition from laminar to turbulent shear layers with emphasis on hypersonically traveling bodies* (tech. rep.). Martin Marietta Corporation Baltimore Maryland Institute for Advanced Studies.

Morkovin, M. V. (1994). Transition in open flow systems-a reassessment. *Bulletin of the American Physical Society*, *39*, 1882.

Özgen, S., Degrez, G., & Sarma, G. (1998). Two-fluid boundary layer stability. *Physics of Fluids*, *10*(11), 2746–2757.

Parente, E., Robinet, J.-C., De Palma, P., & Cherubini, S. (2020). Modal and nonmodal stability of a stably stratified boundary layer flow. *Physical Review Fluids*, *5*(11), 113901.

Prandtl, L. (1905). Uber flussigkeitsbewegung bei sehr kleiner reibung. *Verhandl. 3rd Int. Math. Kongr. Heidelberg (1904), Leipzig*.

Prandtl, L. (1921). Bemerkungen über die entstehung der turbulenz. *ZAMM-Journal of Applied Mathematics and Mechanics/Zeitschrift für Angewandte Mathematik und Mechanik*, *1*(6), 431–436.

Rayleigh, L. (1880). On the stability, or instability, of certain fluid motions. *Proceedings of the London Mathematical Society*, *9*, 57–70.

Reddy, S. C., & Henningson, D. S. (1993). Energy growth in viscous channel flows. *Journal of Fluid Mechanics*, *252*, 209–238.

Ren, J., Fu, S., & Pecnik, R. (2019a). Linear instability of poiseuille flows with highly non-ideal fluids. *Journal of Fluid Mechanics*, *859*, 89–125.

Ren, J., Marxen, O., & Pecnik, R. (2019b). Boundary-layer stability of supercritical fluids in the vicinity of the widom line. *Journal of Fluid Mechanics*, *871*, 831–864.

Sahu, K. C., Ding, H., Valluri, P., & Matar, O. K. (2009). Linear stability analysis and numerical simulation of miscible two-layer channel flow. *Physics of Fluids*, *21*(4), 042104.

Schmid, P. J. (2007). Nonmodal stability theory. *Annual Review of Fluid Mechanics*, *39*(1), 129–162.

Schmid, P. J., & Henningson, D. S. (1994). Optimal energy density growth in hagen–poiseuille flow. *Journal of Fluid Mechanics*, *277*, 197–225.

Schubauer, G. B., & Skramstad, H. K. (1947). Laminar boundary-layer oscillations and transition on. *Journal of Research of the National Bureau of Standards*, *38*, 251.

Timoshin, S., & Hooper, A. (2000). Mode coalescence in a two-fluid boundary-layer stability problem. *Physics of Fluids*, *12*(8), 1969–1978.

Trefethen, L. N. (2000). Spectral methods in matlab, volume 10 of software, environments, and tools. *Society for Industrial and Applied Mathematics (SIAM), Philadelphia, PA*, *24*, 57.

Tumin, A., & Reshotko, E. (2001). Spatial theory of optimal disturbances in boundary layers. *Physics of Fluids*, *13*(7), 2097–2104.

White, M. T., Bianchi, G., Chai, L., Tassou, S. A., & Sayma, A. I. (2021). Review of supercritical co2 technologies and systems for power generation. *Applied Thermal Engineering*, *185*, 116447.

Yecko, P., & Zaleski, S. (2005). Transient growth in two-phase mixing layers. *Journal of fluid mechanics*, *528*, 43–52.

Yih, C.-S. (1967). Instability due to viscosity stratification. *Journal of Fluid Mechanics*, *27*(2), 337–352.